

**Data evaluation for pulse heating experiments
combined with emissivity measurements using a
division-of-amplitude photopolarimeter**

DIPLOMA THESIS

Sachsenhofer Franz

**INSTITUT FÜR EXPERIMENTALPHYSIK
DER TECHNISCHEN UNIVERSITÄT GRAZ**

July 2000

Abstract

The group Subsecond Thermophysics at the Technical University of Graz investigates for more than 10 years thermophysical properties of metals and alloys in the liquid phase by means of an ohmic pulse heating experiment. The temperature of the sample is an important quantity, and therefore the radiance temperature is determined using optical pyrometers. From this the true temperature can be calculated, if the emissivity of the sample is known. Last year, a division-of-amplitude photopolarimeter (DOAP) was added to the consisting system thus spectral-normal emissivity data are obtained. The data evaluation of the conventional pulse-heating system, as well as those of the DOAP demanded the development of a new software. The result is the MATLAB-program HOTWIRE. This diploma thesis shows the features of the new data evaluation software and gives a summary of the required theoretical concepts, especially on ellipsometry. Additionally, numerical simulations were carried out to illustrate the theory and to do some error estimates.

Zur Bestimmung thermophysikalischer Daten von Metallen und Legierungen in der flüssigen Phase wird in der Gruppe Subsekunden Thermophysik an der Technischen Universität Graz seit mehr als 10 Jahren ein ohmsches Pulsheizexperiment eingesetzt. Die Temperatur der Probe ist dabei eine wichtige Meßgröße und man bestimmt die Strahlungstemperatur mittels optischer Pyrometer. Um die wahre Temperatur zu erhalten, muß die Emissivität der Probe bekannt sein. Dazu wird neuerdings ein Division-of-Amplitude Photopolarimeter (DOAP) eingesetzt und damit die spektrale Emissivität für Abstrahlung senkrecht zur Oberfläche (spectral-normal emissivity) bestimmt. Die Auswertung der Daten des herkömmlichen Pulsheizexperimentes, als auch die des DOAP, erforderten die Entwicklung einer neuen Software. Das Ergebnis ist das MATLAB-Programm HOTWIRE. Die Diplomarbeit zeigt die Möglichkeiten dieser neuen Auswertesoftware auf und gibt eine Zusammenfassung der benötigten theoretischen Grundlagen, insbesondere für die Ellipsometrie. Zusätzlich wurden einige numerische Simulationen zur Illustration der Theorie und zur Fehlerabschätzung durchgeführt.

Contents

1	Introduction	1
2	Experimental setup of the pulse heating system	3
3	Evaluation of pulse heating data	6
3.1	Ideal discharge circuit	6
3.2	Voltage correction	14
3.3	Specific enthalpy	16
3.4	Specific resistivity	17
3.5	Temperature	18
4	Program HOTWIRE	26
4.1	HOTWIRE-mode	26
4.2	Voltage correction	37
4.2.1	Manual voltage correction	37
4.2.2	Automatic voltage correction	38
4.3	Parameters of the whole discharge circuit	43
4.4	Temperature via melting plateau	45
5	Ellipsometry	46
5.1	Polarized light	48
5.1.1	The plane wave	48
5.1.2	The polarization ellipse	51
5.1.3	The Jones vector and Jones matrix calculus	52
5.2	Stokes parameters, Mueller matrix and Poincaré sphere	53
5.3	Mueller matrix for reflection	57
5.4	Measurement of the ellipsometric parameters	60
5.5	The fundamental equation of ellipsometry	61
5.6	Reflectance	63
5.7	Simulation of the reflective behavior	65
5.8	Polarizing elements and generation of arbitrary polarized states	71

6	Division-of-amplitude photopolarimeter (DOAP)	78
6.1	The principle of the DOAP	78
6.2	Experimental setup	80
	Electronics	83
6.3	Calibration procedure	85
6.4	Verification of the calibration	90
6.5	Instrument matrix	92
	Interpretation of rows	93
	Interpretation of columns	96
	Condition number for matrix inversion	98
6.6	Alignment to measurement position	99
6.7	Measurement	101
	Geometrical considerations	102
7	DOAP-mode of the HOTWIRE-program	106
7.1	DOAP-mode	106
7.2	Temperature	115
8	Conclusion and future outlook	116
A	Data of selected metals	117

Chapter 1

Introduction

Since computer performance has increased during the last years, simulation of industrial processes becomes more and more important. For example foundry industry uses programs based on finite-element algorithms to optimize casting processes. These programs (e.g. MAGMAsoft) work very well, but the performance depends strongly on the uncertainty of input data, especially in the liquid phase of the material. Therefore one is interested in developing new measurement techniques to increase the accuracy of thermophysical data on metals and/or alloys.

At the Institut für Experimentalphysik der Technischen Universität Graz thermophysical properties of high-melting metals and alloys have already been investigated for more than 10 years using an ohmic pulse heating system (Pottlacher [1]). In this case a capacitor bank (max. charging voltages up to 10 *kV*) is discharged over a thin wire of approx. 0.5 *mm* in diameter and 50 *mm* in length. Within some ten microseconds the sample heats up far above the melting point into the liquid region, and due to the short duration of the experiment the cylindrical shape of the wire is maintained. A fast data acquisition system allows the time-resolved measurement of current through and voltage drop across the wire. From this the energy (enthalpy) fed into the wire is calculated, as well as the specific resistivity of the metal.

Another important quantity is the temperature of the sample, where the only applicable measurement method is radiation thermometry. Therefore an optical pyrometer is used, which is calibrated by means of a tungsten ribbon lamp to obtain the radiance temperature. If the emissivity of the sample is known, the true temperature can be calculated using standard equations of pyrometry.

Up to now there were no possibilities to determine the emissivity of metals and/or alloys in the liquid phase. The measurements based either on blackbody radiation emitted from a small hole in the sample, or by determining the optical parameters by means of standard ellipsometry. The first method allows only temperatures up to melting, because the hole closes itself in the liquid due to surface tension. Standard ellipsometry uses mechanically rotated components and consequently it is not applicable to submicrosecond experiments.

One way out is to use the melting plateau as reference point. Melting temperatures of metals are known very accurate and assuming the emissivity in the vicinity of melting stays constant, the true temperature can be calculated. This method is applicable, if one only is interested in data some 100 *K* into the liquid phase.

In the last years a new type of ellipsometer, a so called DOAP (division-of-amplitude photopolarimeter), without mechanical rotated components has been developed by Azzam [2] and was specially adapted to submicrosecond experiments by Krishnan [3]. One year ago such a device was added to the consisting pulse heating system and now the spectral-normal emissivity at 684.4 *nm* also can be determined time-resolved. With it's knowledge

the accuracy of temperature measurement is increased and also the range expanded far into the liquid region.

The installation of the DOAP demanded a new software program for data evaluation, especially to combine data from the ellipsometer and the pulse heating system. It proved that MATLAB ¹ is the most convenient programming language, not only due to mathematics, but also in generating a comfortable user interface. In this way the program *HOTWIRE* was created which operates in two modes:

- *HOTWIRE-mode*: Evaluation of thermophysical data of metals and alloys in the liquid state by means of ohmic pulse heating.

The principal concepts of data evaluation for the conventional pulse heating system are introduced in chapter 3. Chapter 4.1 shows the features of the *HOTWIRE-mode*, where the melting plateau is used as reference point for temperature calculation.

- *DOAP-mode*: Evaluation of thermophysical data of metals and alloys in the liquid state by means of ohmic pulse heating combined with emissivity measurement using a division-of-amplitude photopolarimeter (DOAP).

The *DOAP-mode* (chapter 7.1) allows evaluation of conventional pulse heating data like in *HOTWIRE-mode*. Additional, emissivity data are calculated using standard equations of ellipsometry (chapter 5) and therefore the temperature of the sample can be computed directly from radiance temperature.

The application of the DOAP to the pulse heating experiment is rather complex and requires a lot of adjustment works. This will be described thoroughly in the master's thesis of Seifter [4], which will be finished approximately in February 2001. The current work is intended to gather theoretical concepts for data evaluation of pulse heating data, as well as ellipsometric data. Additionally, some computer simulations are added to illustrate the theoretical models.

¹MATLAB Version 5.1, The Language of Technical Computing, Copyright ©1984-1997 The Math-Works, Inc.

Chapter 2

Experimental setup of the pulse heating system

It is intended to give only a short overview as it is necessary for the understanding of the following chapters. One finds a full description e.g. by Kaschnitz [5].

Fig. 2.1 shows the schematic circuit diagram of the experimental setup. The capacitor bank C ($500 \mu F$) can be loaded at closed switch S up to $10 kV$ with the high-voltage power supply. A typical charging voltage is $5 kV$, which corresponds to an energy of $6250 J$ or a power of approx. $6 MW$ within the short duration of about $100 \mu s$ that the experiment lasts.

The experiment is started manually at the pulse generator PG . This at first triggers the AD-conversion in the PC and after typically $200 \mu s$, the main ignitron IG_1 . Because of the low inductive construction of the entire discharge circuit the current increases within a few μs to its peak value (see chapter 3.1, Fig. 3.2). The wire sample heats up far above the melting point into the liquid region, the heating rates are up to $10^8 K/s$. Depending on the material the experiment is terminated after approx. $50 \dots 100 \mu s$ by igniting the crowbar ignitron IG_2 . This short-circuits the discharge unit and the remaining energy of the capacitor bank dissipates in R_{CROW} . Without this measure, the arc which begins to burn in the metallic vapour (identified by the repeated rise of the current) would damage the sample holders and may soil the discharge chamber strongly.

The current is measured by means of a Pearson-probe (a current transformer with post-connected integration circuit and divider). The voltage drop on the wire is picked up by knife-edge probes made of tantalum and is divided by R_1 to R_4 . The calibration factors are determined experimentally.

The only possibility to determine the temperature of liquid metals is to use an optical pyrometer. Therefore the intensity of radiation from the surface of the sample is projected onto an optical fiber F with rectangular entry section. The photodiode D is attached to the other side of the fiber. A band-pass filter BPF with small transmission width $\Delta\lambda$ selects only a narrow spectral region around the centre wavelength λ_C . The pyrometers are calibrated with a standardized tungsten strip lamp so that the radiation temperature can be computed directly from the intensity via the calibration factor K .

Currently there are two pyrometers in use:

	λ_C/nm	$\Delta\lambda/nm$	K/V
Pyrometer 1	710	12.7	420.4
Pyrometer 2	1580	84.0	3028.1

Data acquisition is done by two plug-in boards T1012 from IMTEC, which are designed for the use in an IBM-AT compatible personal computer. The resolution is 12 bit by a maximum sampling rate of 10 *MHz* (minimum sample interval 0.1 μ s). The sample depth is normally set to 4096 bytes per channel. The associated software package INSIGHT¹ offers a comfortable user interface to control the AD-acquisition boards and to visualize the recorded data. For further evaluation the data are stored in ASCII-files.

The electromagnetic field in the surrounding of the experiment takes on high values due to the fast rise time of the current. Therefore electronics and data acquisition is placed in a shielded room, and all components outside (e.g. Pearson-probe) must be shielded, too. This is not only necessary to obtain reliable measurement data, but also to avoid damages in any electronic devices.

The radial expansion of the sample is measured by means of a specific line camera (not included in Fig. 2.1). The wire is illuminated from the back with a flash and the silhouette of a small section of the sample is recorded every 10 μ s. The evaluation is carried out with an image processing system.

¹INSIGHT v3.28d 12.03.97 von IMTEC, intelligente Messtechnik GmbH

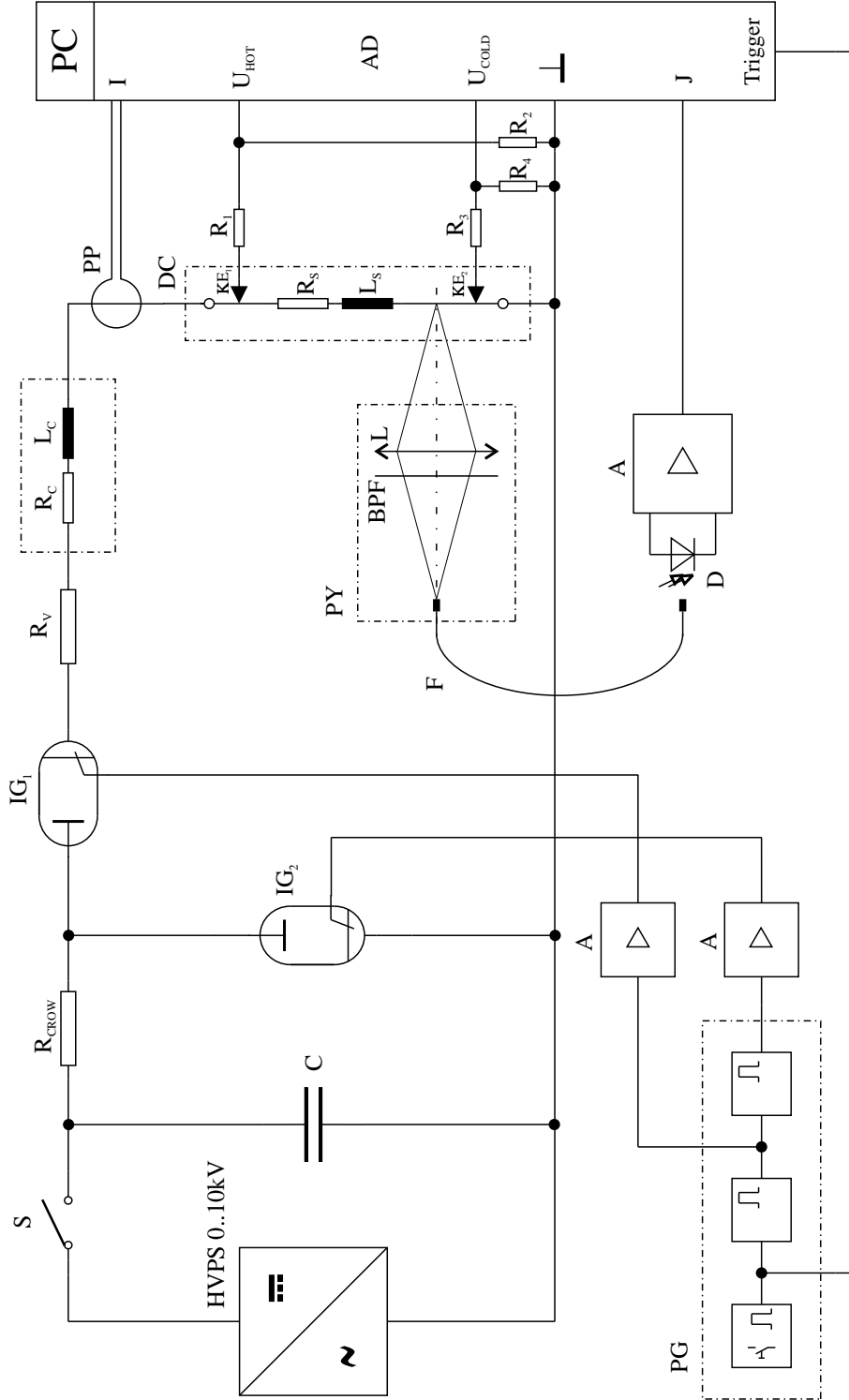


Figure 2.1 Schematic experimental setup

HVPS: high voltage power supply; *S*: switch for loading the capacitor bank *C*; *R_{CROW}*: crowbar resistor; *IG₁*: main ignitron; *IG₂*: crowbar ignitron; *R_C*, *L_C*, *R_S*, *L_S*: resistance and inductance of the circuit and/or the sample; *R₁* - *R₄*: voltage dividers; *KE₁*, *KE₂*: knife-edge probes to pickup the voltage drop across the sample; *PP*: Pearson-probe; *DC*: discharge chamber; *PY*: pyrometer; *L*: lens; *BPF*: band-pass filter; *F*: fiber; *D*: photodiode; *A*: amplifier; *PG*: pulse generator; *AD*: analog-to-digital converter; *PC*: personal computer; *I*, *U_{HOT}*, *U_{COLD}*, *J*: measurement signals of current, voltages and intensity of radiation.

Chapter 3

Evaluation of pulse heating data

The evaluation of ohmic pulse heating experiments is described in detail by Seydel, Fucke [6]. Here only a short overview is given and the equations used in *HOTWIRE* are listed.

Additional, the first chapter 3.1 deals with a simple electric equivalent model of the discharge circuit. The so derived equations allow to check the parameters (especially resistance and inductance) of the whole discharge circuit, for example after installing some new components in the experimental setup.

3.1 Ideal discharge circuit

The ideal discharge circuit is in principle similar to a *RLC*-circuit which is strongly damped (schematic see Fig. 3.1). It is important that the current first rises very rapidly and then remains nearly constant during the time of melting. This is done by a low inductive design of the experimental setup and a relatively high damping resistor ($R_{CROW} + R_V$ in Fig. 2.1). Because the experiment is terminated by the crowbar-ignitron the current gets its typical rectangular shape.

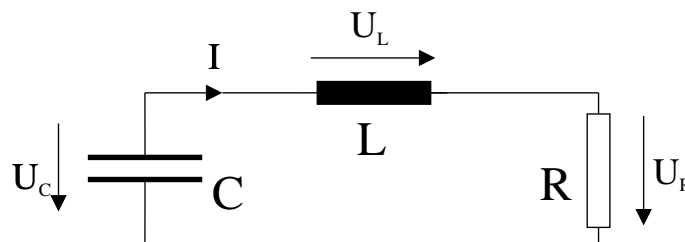


Figure 3.1: Simplified schematic diagram of the discharge circuit
 R : resistor; L : inductor; C : capacitor; I : current; U_R, U_L, U_C :
voltage drops.

In Fig. 3.1 the voltage-arrows are drawn with respect to the passive sign convention ¹.

¹In the passive sign convention supplied energies are negative (and absorbed positive) by definition. Resistor R and inductor L are seen to absorb energy, therefore the positive signs in (3.1) for U_R and U_L . The capacitor supplies the circuit with energy, hence the negative sign by U_C and also by W_C in (3.20).

The relations between voltage drops U_R , U_L , U_C across the components and current I are given by:

$$U_R = R I \quad U_L = L \frac{dI}{dt} \quad U_C = -\frac{1}{C} \int I dt \quad (3.1)$$

R ... resistance

L ... inductance

C ... capacitance

t ... time

By means of Kirchhoff's voltage law

$$U_L + U_R - U_C = 0 \quad (3.2)$$

we get differential equation (3.3) of the RLC -circuit, when we substitute (3.1) into (3.2) and differentiate once.

$$\frac{d^2 I}{dt^2} + \frac{R}{L} \frac{dI}{dt} + \frac{1}{LC} I = 0 \quad (3.3)$$

Trying the solution approach

$$I = \frac{I_0}{2} e^{\lambda t} \quad (3.4)$$

I_0 ... arbitrary constant

we obtain the characteristic equation for the parameter λ

$$\lambda^2 + \frac{R}{L} \lambda + \frac{1}{LC} = 0 \quad (3.5)$$

whose solution can be represented as follows:

$$\lambda = \delta \pm \Omega \quad (3.6)$$

where

$$\delta = \frac{R}{2L} \quad \dots \quad \text{damping constant} \quad (3.7)$$

$$\omega_0 = \frac{1}{\sqrt{LC}} \quad \dots \quad \text{angular frequency of the undamped } RLC\text{-circuit} \quad (3.8)$$

$$\Omega = \sqrt{\delta^2 - \omega_0^2} \quad \dots \quad \text{angular frequency of the damped system} \quad (3.9)$$

The meaning of the above terms becomes clear, if we consider the underdamped RLC -circuit (see below). Because of the demand of strong damping the condition $\delta \gg \omega_0$ holds and therefore Ω is real.

The general solution of differential equation (3.3) is given by:

$$I = \frac{I_{01}}{2} e^{-\delta t} e^{\Omega t} + \frac{I_{02}}{2} e^{-\delta t} e^{-\Omega t} \quad (3.10)$$

The constants I_{01} and I_{02} are determined by the initial conditions

$$I(t = 0) = 0 \quad (3.11)$$

$$U_C(t = 0) = U_0 \quad (3.12)$$

where U_0 is the initial load voltage of the capacitor bank. From (3.11) we obtain

$$\frac{I_{01}}{2} = \frac{I_{02}}{2} =: \frac{I_0}{2} \quad (3.13)$$

and inserting this into (3.10) and using the identity $\sinh x = \frac{1}{2}(e^x - e^{-x})$

$$I = I_0 e^{-\delta t} \sinh \Omega t \quad (3.14)$$

Using (3.1), (3.2), (3.11) and (3.12) we find

$$\frac{U_0}{L} = \left. \frac{dI}{dt} \right|_{t=0} \quad (3.15)$$

This equation can be used to determine the inductance of the whole discharge circuit from load voltage and beginning gradient of current.

If we differentiate once expression (3.14) and set $t = 0$, we obtain the constant I_0 and finally the solution for the current

$$I = \frac{U_0}{\Omega L} e^{-\delta t} \sinh \Omega t \quad (3.16)$$

In the case of underdamping there is the condition $\omega_0 > \delta$ and thus Ω is complex. Instead of the \sinh -term in (3.16) a \sin -term occurs which describes a damped harmonic oscillation. It's angular frequency is Ω and the damping constant δ .

Now we easily can calculate the voltage drops from current (3.16) using equations (3.1).

$$\begin{aligned} U_R &= \frac{U_0}{\Omega L} e^{-\delta t} \sinh \Omega t \\ U_L &= U_0 e^{-\delta t} \left(\cosh \Omega t - \frac{\delta}{\Omega} \sinh \Omega t \right) \\ U_C &= U_0 e^{-\delta t} \left(\cosh \Omega t + \frac{\delta}{\Omega} \sinh \Omega t \right) \end{aligned} \quad (3.17)$$

During the discharge the energy stored in the capacitor bank decreases and is dissipated in form of heat by the resistor. Inserting (3.16) into the general relation for the energy W in an electric circuit

$$W = \int U I dt \quad (3.18)$$

we find for the energies W_C in the capacitor, W_L in the inductor and W_R in the resistor

$$\begin{aligned} W_C &= - \int U_C C \frac{dU_C}{dt} dt = -C \int U_C dU_C = -\frac{CU^2}{2} \\ W_L &= \int I L \frac{dI}{dt} dt = L \int I dI = \frac{LI^2}{2} \\ W_R &= R \int I^2 dt \end{aligned} \quad (3.19)$$

Inserting (3.16) and (3.17) we finally have

$$\begin{aligned}
 W_C &= \frac{CU_0^2}{2} e^{-2\delta t} \left(\cosh \Omega t + \frac{\delta}{\Omega} \sinh \Omega t \right)^2 \\
 W_L &= \frac{U_0^2}{2L\Omega^2} e^{-2\delta t} \sinh^2 \Omega t \\
 W_R &= \frac{CU_0^2}{2} \left[1 - e^{-2\delta t} \left(2 \frac{\delta^2}{\Omega^2} \sinh^2 \Omega t + 2 \frac{\delta}{\Omega} \sinh \Omega t \cosh \Omega t + 1 \right) \right]
 \end{aligned} \tag{3.20}$$

Adding the last three equations we find

$$W_C + W_L + W_R = \frac{CU_0^2}{2} \tag{3.21}$$

Therefore for each time the sum of the energies in the components equals the initial energy stored in the capacitor. This is nothing else then the law of energy conservation.

Without going into details there are some useful formulas dealing with the current maximum:

- Current maximum

$$I_{max} = \frac{U_0}{\sqrt{\frac{L}{C}}} e^{-\left(\frac{\delta}{\Omega} \operatorname{artanh} \frac{\Omega}{\delta}\right)} \tag{3.22}$$

- Time of current maximum

$$t_{I_{max}} = \frac{1}{\Omega} \operatorname{artanh} \frac{\Omega}{\delta} \tag{3.23}$$

- Current-time-area from $t = 0$ to $t_{I_{max}}$

$$\int_{t=0}^{t_{I_{max}}} I dt = C (U_0 - I_{max}R) \tag{3.24}$$

Additional to *HOTWIRE* there is the small program *SIMWIRE*. It allows the simulation of current, voltage and energy for arbitrary parameters U_0 , R , L and C . Some results are shown in Fig. 3.2, 3.3 and 3.4.

Figures 3.5 till 3.8 show the influence of the different parameters to the current. The most interesting diagram is Fig. 3.7, because one can see the importance of a low inductive design of the experimental setup to obtain a rectangular shaped current.

SIMWIRE is not restricted to the overdamped case as discussed here, it is also possible to simulate damped oscillations by choosing the appropriate parameters.

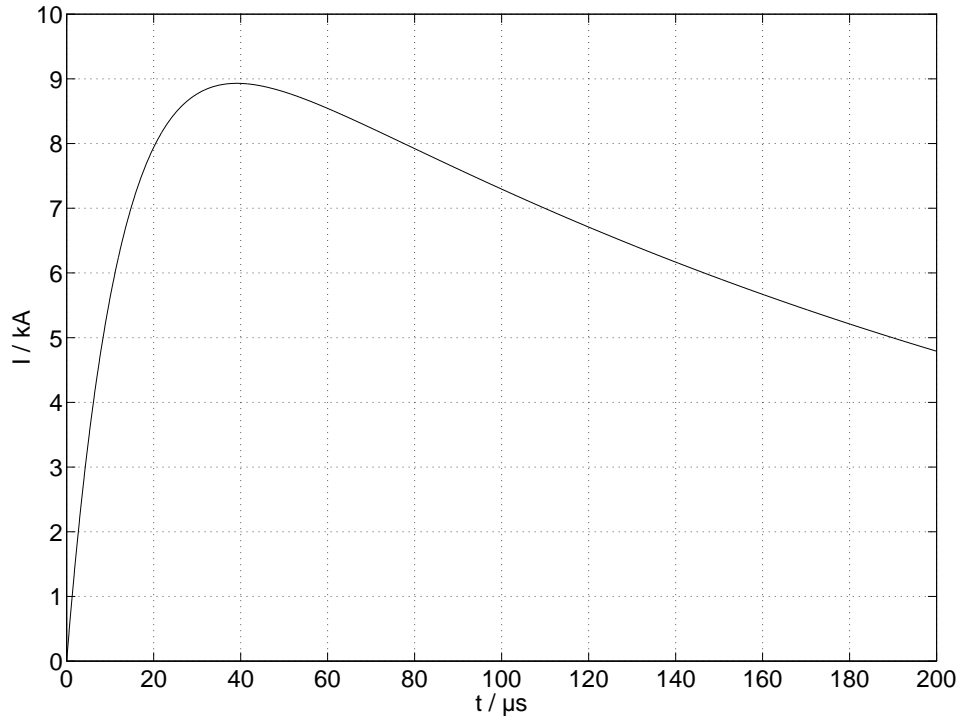


Figure 3.2: Theoretical current (3.16); $U_0 = 5 \text{ kV}$, $R = 0.5 \Omega$,
 $L = 6 \mu\text{H}$, $C = 500 \mu\text{F}$
 I : current; t : time.

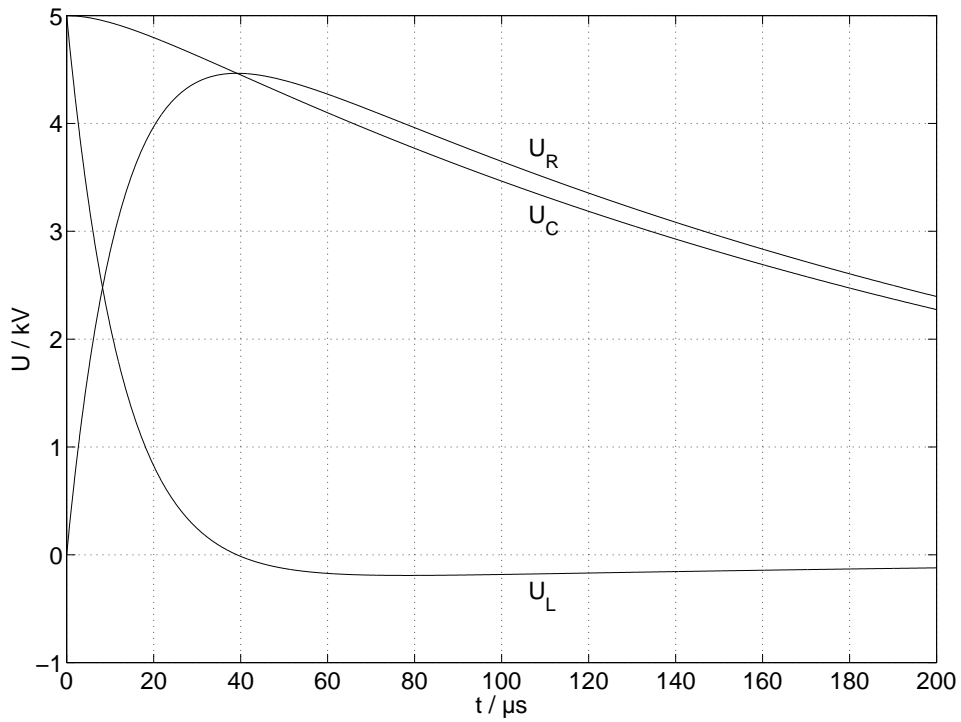


Figure 3.3: Theoretical voltages (3.17); $U_0 = 5 \text{ kV}$, $R = 0.5 \Omega$,
 $L = 6 \mu\text{H}$, $C = 500 \mu\text{F}$
 U_R , U_L , U_C : voltage drops across resistor, inductor and
capacitor; t : time.

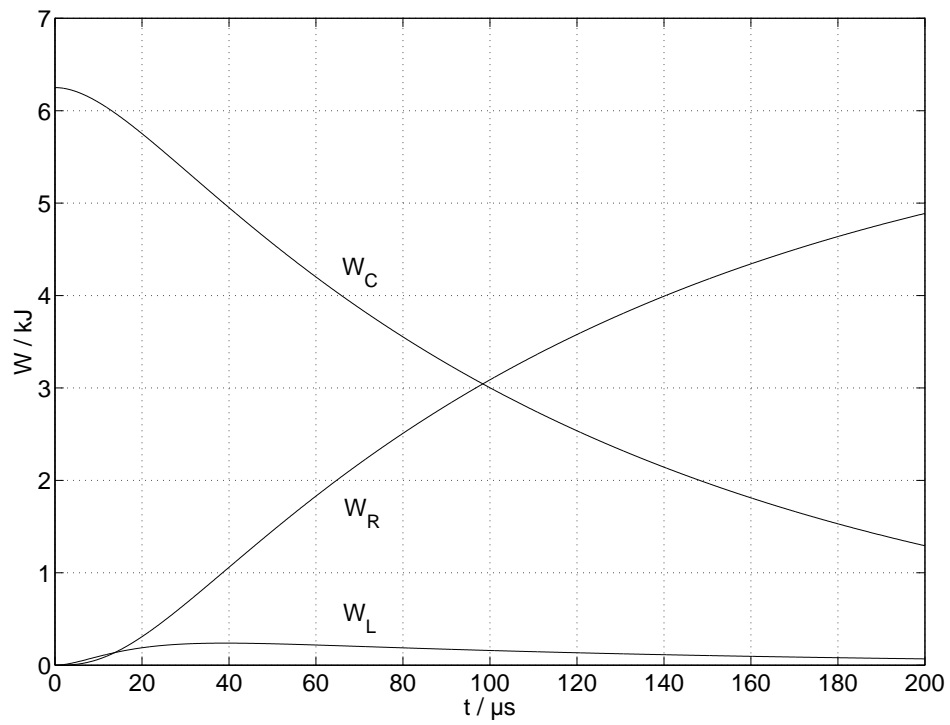


Figure 3.4: Theoretical energies (3.20); $U_0 = 5 \text{ kV}$, $R = 0.5 \Omega$,
 $L = 6 \mu\text{H}$, $C = 500 \mu\text{F}$
 W_R , W_L , W_C : energy in resistor, inductor and capacitor;
 t : time.

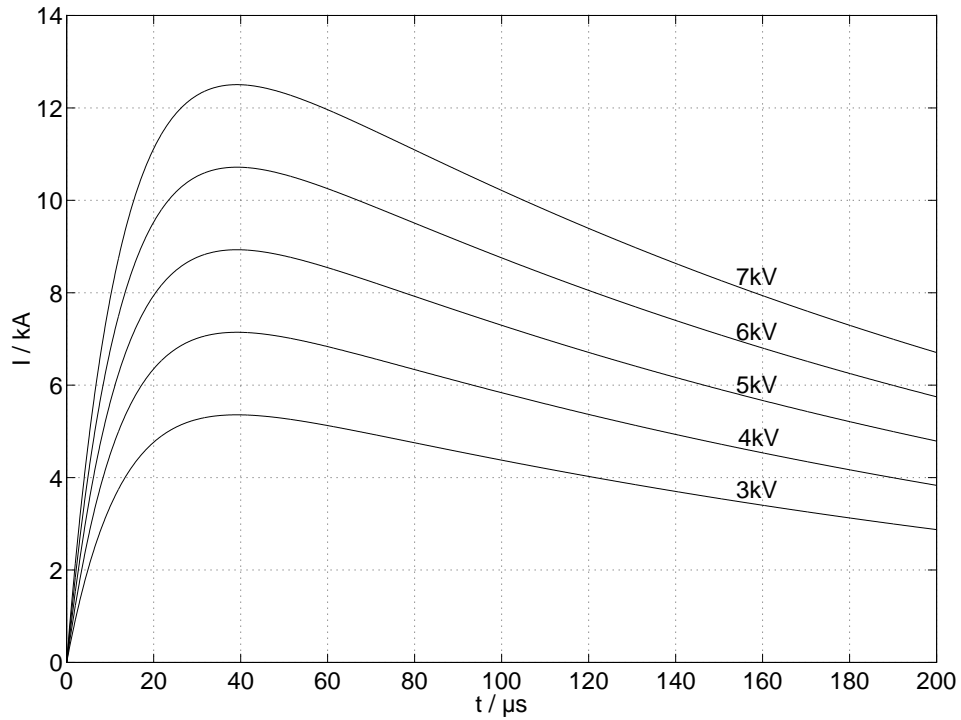


Figure 3.5: Theoretical current (3.16) with load voltage U_0 as parameter;
 I : current; t : time.

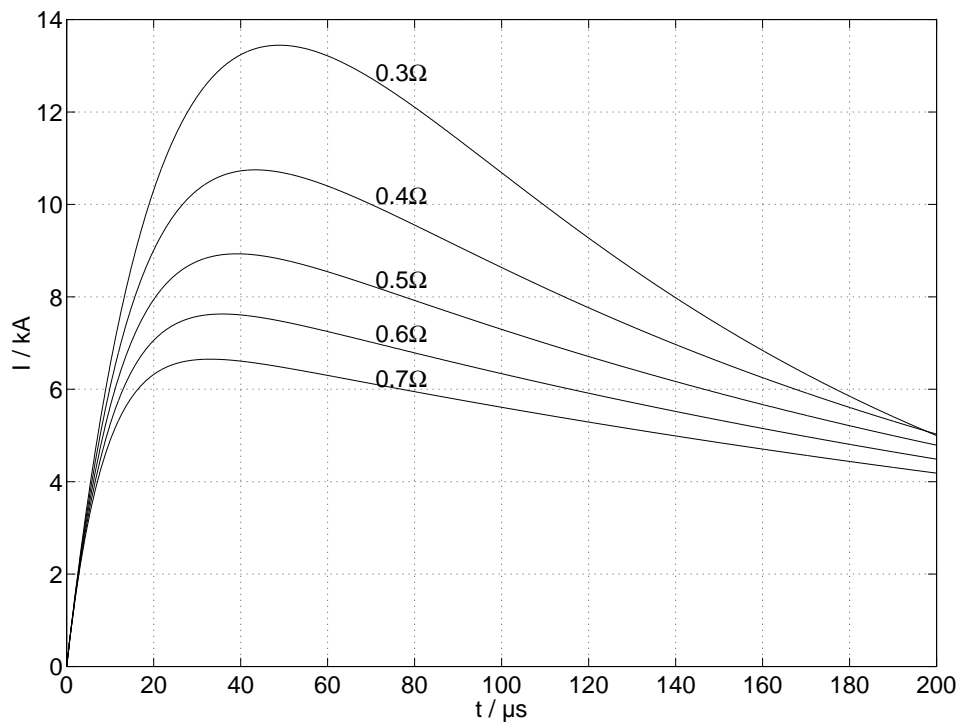


Figure 3.6: Theoretical current (3.16) with resistance R as parameter;
 I : current; t : time.

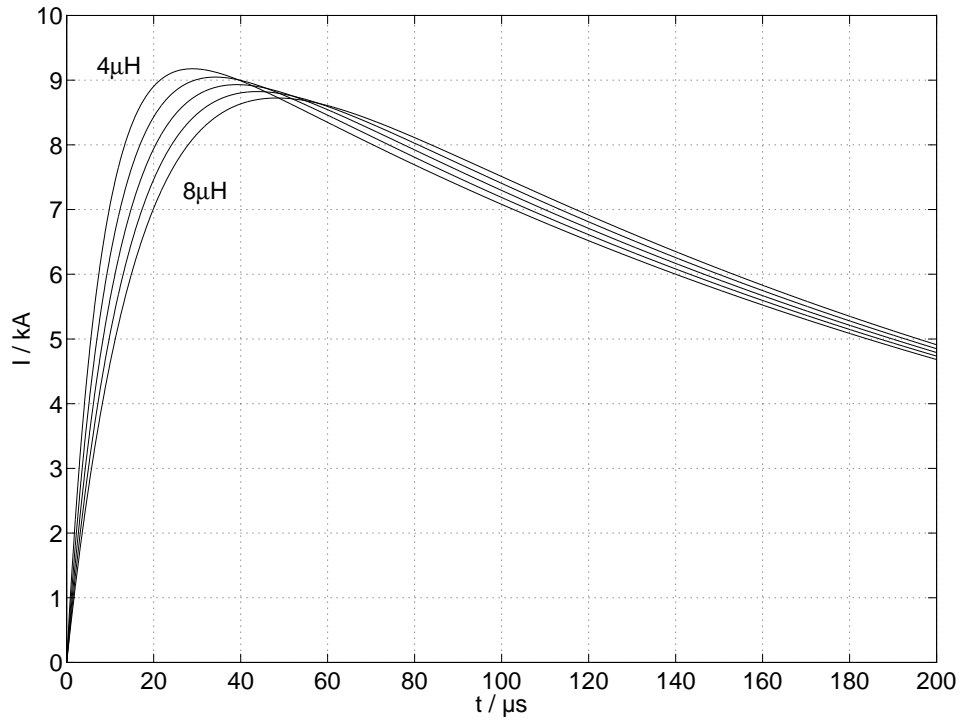


Figure 3.7: Theoretical current (3.16) with inductance L as parameter; $L = 4, 5, 6, 7, 8 \mu H$; I : current; t : time.

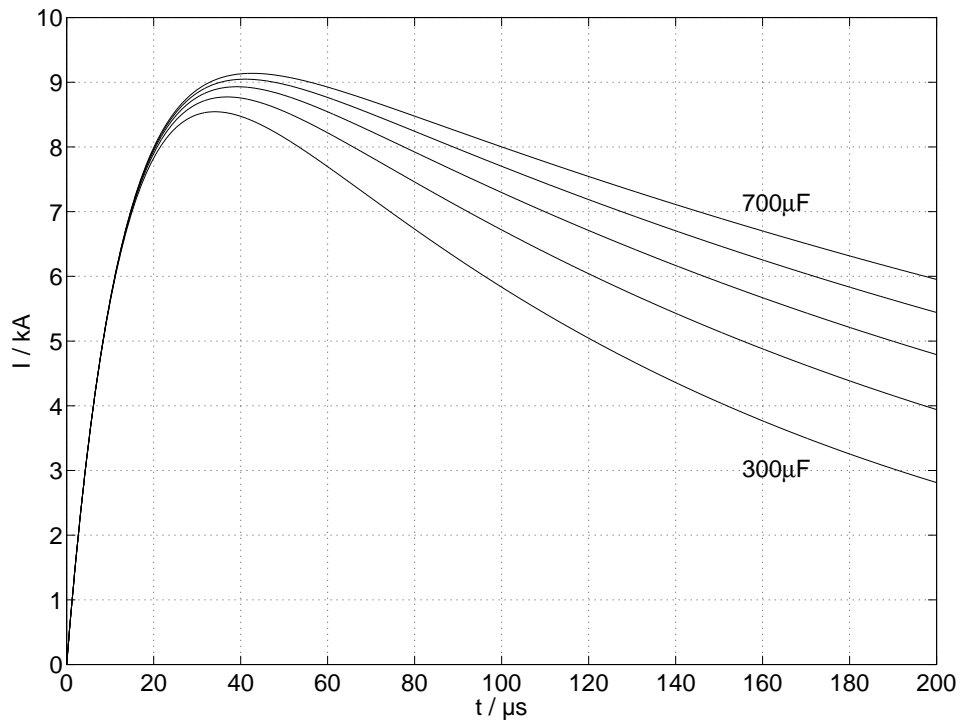


Figure 3.8: Theoretical current (3.16) with capacitance C as parameter; $C = 300, 400, 500, 600, 700 \mu F$; I : current; t : time.

3.2 Voltage correction

The voltage drop U_S across the sample consists of the following three terms:

$$U_S = IR_S + L_S \frac{dI}{dt} + I \frac{dL_S}{dt} \quad (3.25)$$

R_S ... sample resistance

L_S ... sample inductance

The first one is the desired ohmic voltage drop. Only this part contributes to the electric energy, which is dissipated within the wire in form of heat. The other terms describe the influence of the sample inductance. The construction of the discharge chamber is similar to a coaxial cylinder. The sample is the inner conductor and the current flows back in the outer housing. The inductance of this configuration is the sum of three terms (see e.g. Küpfmüller [7]):

- Inductance of inner conductor

$$L_1 = \frac{\mu_0 \mu_{r,S} l}{8\pi} \quad (3.26)$$

$\mu_{r,S}$... relative permeability of sample material

Note that this term is independent from the wire radius.

- Inductance of insulant

$$L_2 = \frac{\mu_0 l}{2\pi} \ln \frac{d_2}{d_1} \quad (3.27)$$

d_1 ... diameter wire

d_2 ... inner diameter discharge chamber

- Inductance of outer conductor

$$L_3 = \frac{\mu_0 l}{2\pi (d_3^2 - d_2^2)} \left(\frac{d_3^4}{d_3^2 - d_2^2} \ln \frac{d_3}{d_2} - \frac{3d_3^2 - d_2^2}{4} \right) \quad (3.28)$$

d_3 ... outer diameter discharge chamber

All three terms increase linear with the length of the sample. For the experiment we usually use wires with a diameter of 0.5 mm. Therefore the inductance per unit length should be constant for different materials. The next numerical example shows the contribution of the different parts.

$$\begin{aligned}
d_1 &= 0.5 \text{ mm} & d_2 &= 80 \text{ mm} & d_3 &= 110 \text{ mm} \\
\mu_{r,S} &= 1 \\
\Rightarrow L_S &= L_1 + L_2 + L_3 = 0.050 + 1.015 + 0.025 = 1.09 \text{ nH/mm}
\end{aligned}$$

We see that the influence of the inner and outer conductor is negligible. L_1 only becomes interesting for ferromagnetic materials, because of the relative permeability $\mu_{r,S}$. So the second term L_2 is the dominating one.

The volume expansion of the wires is usually small (about 7 % from 0 K to melting for fcc-structured metals, see Weißmantel [8], chapter 5.4.2). Applying this to L_2 we find that the third term in (3.25) can be neglected.

These theoretical considerations show the influence of the different parameters to inductance. But the wire length is much smaller than the dimensions of the discharge chamber and the magnetic field is not as homogeneous as in an ideal coaxial cylinder. Hence the above equations are only an estimation and cannot be used for the actual correction of the voltage drop across the sample.

At time $t = 0$ the current I is zero. So equation (3.25) reduces to

$$U_S(t = 0) = L_S \left. \frac{dI}{dt} \right|_{t=0} \quad (3.29)$$

The step in the voltage signal at $t = 0$ is only due to the inductance of the sample. To determine L_S we have to analyse the current gradient at $t = 0$ and also the height of the voltage step. The corrected voltage $U_{S, \text{corr}}$ then is given by

$$U_{S, \text{corr}} = U_S - L_S \frac{dI}{dt} \quad (3.30)$$

The correction of the voltage is the main task of *HOTWIRE*.

3.3 Specific enthalpy

The enthalpy H is a thermophysical quantity which is defined by

$$H = U + pV \quad (3.31)$$

U ... internal energy

p ... pressure

V ... volume

Like the internal energy the enthalpy only depends on the state and not on the previous history of the system. Therefore we have the exact differential

$$dH = dU + p dV + V dp \quad (3.32)$$

At constant pressure ($dp = 0$) we find with the first law of thermodynamics

$$dU = \delta Q - p dV \quad (3.33)$$

δQ ... infinitesimal quantity of heat

the relation

$$dH = \delta Q_p \quad (3.34)$$

δQ_p ... heat change at constant pressure

Subsequently the heat delivered to the sample by the electric energy leads entirely to an increase of enthalpy.

Integrating the above equation we have to fix a reference point where the enthalpy of a pure element is set to zero. This is called the standard state of the material and is defined at room temperature (298 K) and normal pressure (1 atm). At the beginning of the experiment these conditions are well matched and so we can compute the specific enthalpy (per unit mass) simply by

$$H = \frac{1}{m} \int U_{S, \text{corr}} I dt \quad (3.35)$$

m ... sample mass

$U_{S, \text{corr}}$... corrected voltage drop across the sample

I ... current

The mass of the wire is constant during the experiment and can be calculated using density values δ at room temperature from literature. The volume of the sample is determined by its diameter d and its length l between the knife-edge probes. Therefore the mass is given by

$$m = \delta \frac{d^2 \pi}{4} l \quad (3.36)$$

3.4 Specific resistivity

Using Ohm's law we determine the resistance ρ of the wire from the corrected voltage drop $U_{S, corr}$ and the current I .

$$\rho = \frac{U_{S, corr}}{I} \quad (3.37)$$

The specific resistivity ρ_0 is the resistance per unit length and for a unit cross-sectional area. Considering the cylindrical geometry of the sample we find

$$\rho_0 = \frac{U_{S, corr}}{I} \frac{d_0^2 \pi}{4l} \quad (3.38)$$

d_0 ... wire diameter at room temperature

l ... length of wire

While the length does not change during the experiment (because of the short duration) there is a radial expansion. This is measured with a special line camera as described in Chapter 2. The correction of ρ_0 due to volume expansion is not part of *HOTWIRE*.

3.5 Temperature

Theory and practice of radiation thermometry are discussed in detail by DeWitt [10]. The following is a short overview of needed concepts for temperature evaluation in pulse heating experiments.

The sample temperature can be determined by measuring the spectral radiance² L_λ coming from the surface of the wire. For the further analysis we need the concept of blackbody radiation. L_λ is related to the spectral radiance $L_{\lambda,b}$ of a blackbody via the emissivity ϵ by

$$L_\lambda(\lambda, T) = \epsilon(\lambda, T) L_{\lambda,b}(\lambda, T) \quad (3.39)$$

λ ... wavelength

T ... absolute temperature

Note that emissivity depends on wavelength and temperature.

The spectral distribution of blackbody radiation is described by Planck's radiation law. Stated in terms of spectral radiance L_λ , the law is

$$L_{\lambda,b}(\lambda, T) = \frac{c_1}{\pi\lambda^5} \frac{1}{e^{\frac{c_2}{\lambda T}} - 1} \quad (3.40)$$

where c_1 is the first radiation constant ($c_1 = 2\pi hc^2 = 3.7415 \times 10^{-16} \text{ Wm}^2$), and c_2 the second radiation constant ($c_2 = hc/k_B = 1.43879 \times 10^{-2} \text{ mK}$) (h Planck's constant, c speed of light, k_B Boltzmann's constant).

In the experimental setup we use an optical system to project the radiated light onto the photodetector (see chapter 2). The amount of radiant flux Φ_D which reaches the detector is given by the integral

$$\Phi_D(T) = G \int_0^\infty L_\lambda(\lambda, T) T_F(\lambda) T_{OP}(\lambda) S(\lambda) d\lambda \quad (3.41)$$

G ... geometry factor

T_F ... transmittance of the wavelength filter

T_{OP} ... transmittance of the optical path

S ... spectral responsivity of the photodiode

Theoretically the flux is attained by integration over solid angle and wire surface regarding the imaging system. In the above equation this is described by the geometry factor.

By means of an optical band-pass filter a very small wavelength interval is selected from the entire spectrum. Therefore equation (3.41) can be simplified to

$$\Phi_D(T) = G L_\lambda(\lambda_0, T) T_F(\lambda_0) T_{OP}(\lambda_0) S(\lambda_0) \Delta\lambda \quad (3.42)$$

λ_0 ... centre wavelength of filter

The photodetector provides a voltage signal U_D which is linear to the incoming flux Φ_D . Therefore we also can write U_D in the above equation instead of Φ_D , regarding the additional factor within S .

The factors G , T and S remain constant during the experiment and also between different experiments. Hence, if we consider only ratios between different radiance signals, these factors will cancel out.

²The spectral radiance is the flux per unit solid angle in the given direction, per unit projected area perpendicular to the given direction and per unit wavelength interval. The radiant flux is the radiant energy per unit time.

Now there are two concepts of evaluating temperature using the above equations:

- Radiance temperature

In this case the pyrometer is calibrated by means of a tungsten strip lamp. As result we obtain the calibration factor K , which can be used to compute the so called spectral radiance temperature T_λ . This is the temperature of a blackbody emitting the same spectral radiance as measured. If we set $\epsilon = 1$ in (3.39) and use (3.40) and (3.42) we find

$$T_\lambda = \frac{c_2}{\lambda \ln\left(\frac{K}{U_D} + 1\right)} \quad (3.43)$$

Now we can write (3.39) in the form

$$L_\lambda(T) = L_{\lambda,b}(T_\lambda) = \epsilon(T) L_{\lambda,b}(T) \quad (3.44)$$

Inserting equation (3.40) we obtain the true temperature T of the sample.

$$T = \frac{c_2}{\lambda} \frac{1}{\ln\left(\epsilon_\lambda \left(e^{\frac{c_2}{\lambda T_\lambda}} - 1\right) + 1\right)} \quad (3.45)$$

The emissivity ϵ is measured with the DOAP system as described in chapter 5.

- Melting plateau as reference point

Pure elements have a marked melting plateau in the radiance curve and the melting temperatures T_M are well known from literature. If $U_D(T_M)$ is the intensity signal at the melting point we obtain using (3.42), (3.39) and (3.40)

$$\frac{U_D(T)}{U_D(T_M)} = \frac{\epsilon(T)}{\epsilon(T_M)} \frac{e^{\frac{c_2}{\lambda T_M}} - 1}{e^{\frac{c_2}{\lambda T}} - 1} \quad (3.46)$$

$$e^{\frac{c_2}{\lambda T}} - 1 = \frac{\epsilon(T)}{\epsilon(T_M)} \frac{U_D(T_M) \left(e^{\frac{c_2}{\lambda T_M}} - 1\right)}{U_D(T)} =: \frac{K}{U_D(T)} \quad (3.47)$$

Therefore we obtain again equation (3.43), but now for the true temperature. The calibration factor K is given by the melting point data, setting the ratio of the emissivities equal to one. This crude approximation is valid, if we only look a few 100 K into the liquid phase. Further considerations to this topic are given by Seifert [9].

The main advantage of this method is, that one also can use an uncalibrated pyrometer as long as the output signal is linear to the incoming radiant flux.

Additional to *HOTWIRE* some small programs were developed concerning temperature measurement.

- *PLANCK*: Planck's radiation law and Wien's displacement law

This program shows the typical graphs of spectral radiance in the case of blackbody radiation using equation (3.40). The line joining the maxima of the radiance curves indicates Wien's displacement law. It says

$$\lambda_{max} T = 2.8978 \times 10^{-3} \text{ mK} \quad (3.48)$$

The results are shown in Fig. 3.9 for a temperature interval of 1000...2000 *K* and in Fig. 3.10 for 2000...4000 *K*.

- *WIEN*: Wien's approximation to blackbody radiation

At low temperatures, where $\lambda T \ll c_2$, the 1 in the denominator of (3.40) can be neglected and so we come to Wien's approximation to blackbody radiation.

$$L_{\lambda, b}(\lambda, T) = \frac{c_1}{\pi \lambda^5} e^{-\frac{c_2}{\lambda T}} \quad (3.49)$$

The program shows the difference between this approximation and Planck's radiation law.

- *PHOTODET*: Intensity reaching the photodetector as a function of temperature

Choosing an appropriate wavelength filter it is of interest to compare between different centre wavelengths. Therefore the program *PHOTODET* shows the intensity reaching the detector as a function of temperature.

The results for the currently used filters are shown in Fig. 3.11. Comparing both curves one can see that it is necessary to use the infrared pyrometer at 1580 *nm* to obtain temperatures below about 1700 *K*.

- *SIMWIEN*: Error estimation for temperature measurement with a calibrated pyrometer using Wien's approximation instead of Planck's radiation law

As explained before we calculate the true temperature of the sample from the radiance temperature using expression (3.45). In literature

$$\frac{1}{T} - \frac{1}{T_\lambda} = \frac{\lambda}{c_2} \ln(\epsilon) \quad (3.50)$$

is given, which is derived using Wien's approximation (3.49) instead of Planck's radiation law. The program *SIMWIEN* calculates the difference in true temperature between the two considerations. The error depends also on the actual emissivity, so there are curves with emissivity as parameter in the range of 0.2...0.5.

The results are shown in Fig. 3.13 and Fig. 3.14 for the currently used pyrometers.

The figures show that Wien's approximation is not applicable to the temperature range covered by pulse heating experiments. Subsequently the exact expression (3.45) has to be used for temperature evaluation.

- *SIMTEMP*: Error estimation for temperature measurement with an optical pyrometer using a band-pass filter of finite bandwidth

By measuring the temperature with an optical pyrometer we make an error due to the finite bandwidth of the band-pass filter. The program *SIMTEMP* estimates this error, which occurs using approximation (3.42) instead of integral (3.41). The band-pass filter is simulated by the simple model:

$$T_F = \begin{cases} 1 & : \text{ within the interval } [\lambda_0 - \frac{\Delta\lambda}{2}, \lambda_0 + \frac{\Delta\lambda}{2}] \\ 0 & : \text{ outside} \end{cases} \quad (3.51)$$

T_F ... transmittance
 λ_0 ... centre wavelength
 $\Delta\lambda$... bandwidth

If we neglect the wavelength dependence of the other parameters in (3.41), the photodetector receives the intensity

$$I = K \int_{\lambda_0 - \frac{\Delta\lambda}{2}}^{\lambda_0 + \frac{\Delta\lambda}{2}} \frac{c_1}{\pi\lambda^5} \frac{1}{e^{\frac{c_2}{\lambda T}} - 1} d\lambda \quad (3.52)$$

where K is a proportionality factor. Using approximation (3.42) we find

$$I = K' \frac{c_1}{\pi\lambda_0^5} \frac{1}{e^{\frac{c_2}{\lambda_0 T}} - 1} \Delta\lambda \quad (3.53)$$

or to calculate the temperature from this expression

$$T = \frac{c_2}{\lambda_0} \left(\ln \left\{ \frac{c_1 K' \Delta\lambda}{\pi\lambda_0^5 I} + 1 \right\} \right)^{-1} \quad (3.54)$$

To estimate the error, we first compute the intensity (3.52) for a given temperature, and then we come back to the temperature using the last equation. The factors K and K' are set equal to one. The difference between given and calculated temperature is the absolute error in Kelvin.

As described before we also can compute the temperature using the melting plateau as reference point. To check the error in this case we determine K and K' in such a way, that the intensities (3.52) and (3.53) are equal at the melting temperature T_M . Setting $K' = 1$, we find for K

$$K = \frac{\frac{c_1}{\pi\lambda_0^5} \frac{1}{e^{\frac{c_2}{\lambda_0 T_M}} - 1} \Delta\lambda}{\int_{\lambda_0 - \frac{\Delta\lambda}{2}}^{\lambda_0 + \frac{\Delta\lambda}{2}} \frac{c_1}{\pi\lambda^5} \frac{1}{e^{\frac{c_2}{\lambda T_M}} - 1} d\lambda} \quad (3.55)$$

The temperature error is calculated in the same way as described above. By definition the error is now zero at the melting temperature.

The results for the currently used filters (see chapter 2) are shown in Fig. 3.12. The melting temperature was set to 2000 K .

The errors made by this approximation are relatively small. Especially the error for the pyrometer at 710 nm is negligible compared to the statistical uncertainties. For a more accurate evaluation the concepts of effective wavelength have to be established as described by DeWitt [10].

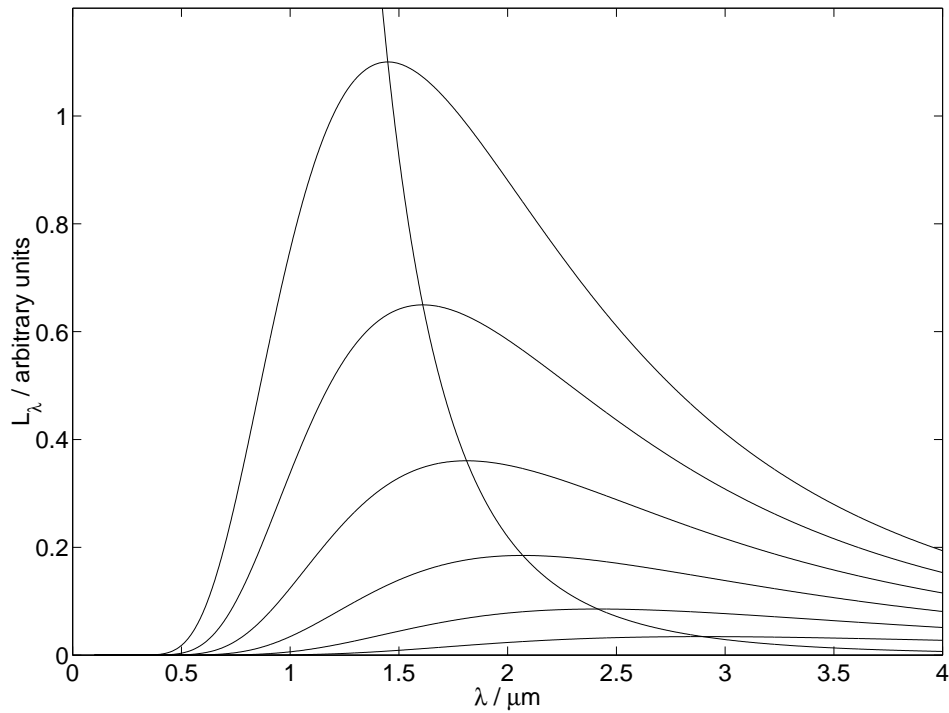


Figure 3.9: Planck's radiation law and Wien's displacement law;
parameter: temperature $T = 1000 \dots 2000 \text{ K}$ in steps
of 200 K
 L_λ : spectral radiance; λ : wavelength.

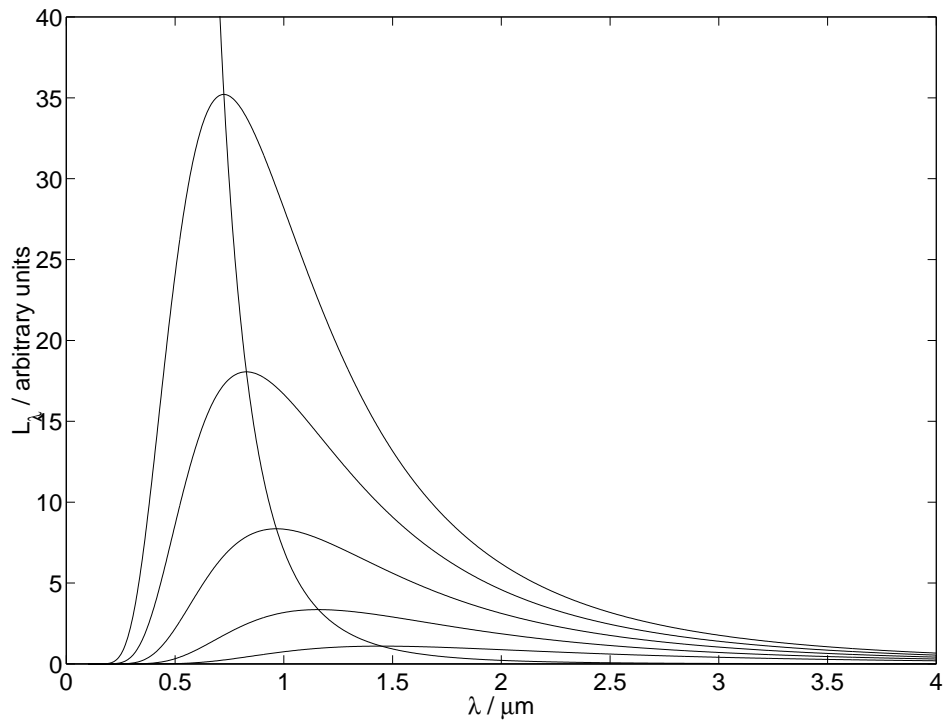


Figure 3.10: Planck's radiation law and Wien's displacement law;
parameter: temperature $T = 2000 \dots 4000 \text{ K}$ in steps
of 500 K
 L_λ : spectral radiance; λ : wavelength.

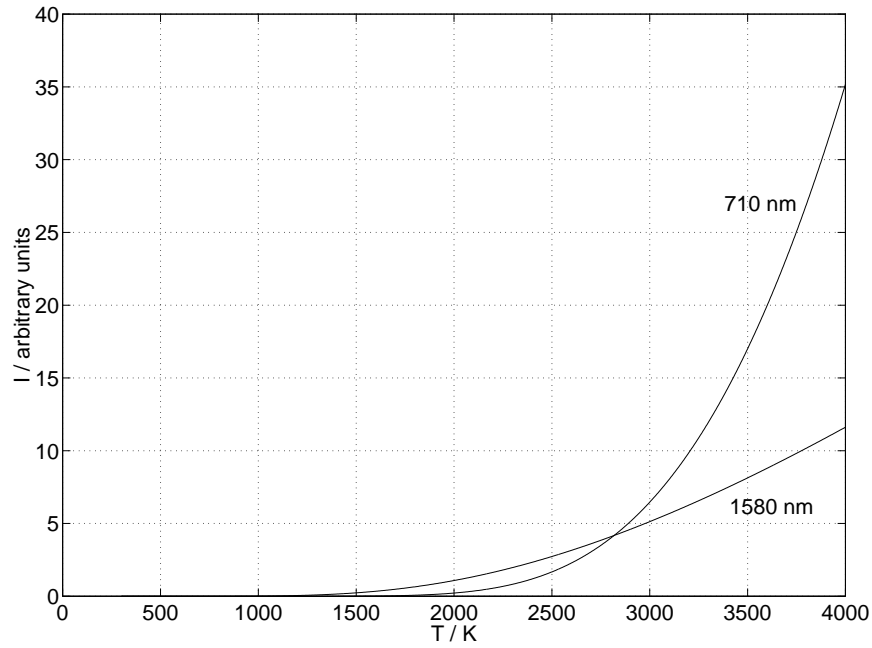


Figure 3.11: Intensity reaching the photodetector as a function of temperature;
I: intensity; *T*: temperature.

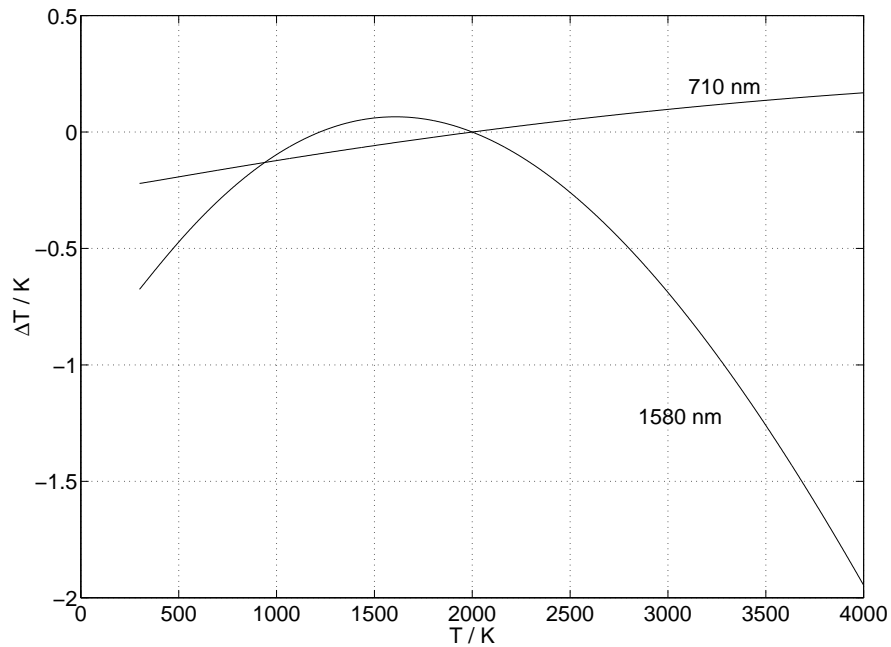


Figure 3.12: Error estimation for temperature measurement with an optical pyrometer using a band-pass filter;
 parameter: $\lambda_0 = 710 \text{ nm}$, $\Delta\lambda = 12.7 \text{ nm}$
 $\lambda_0 = 1580 \text{ nm}$, $\Delta\lambda = 84 \text{ nm}$
 melting temperature: 2000 K
 λ_0 : centre wavelength; $\Delta\lambda$: bandwidth; ΔT : temperature difference; *T*: temperature.

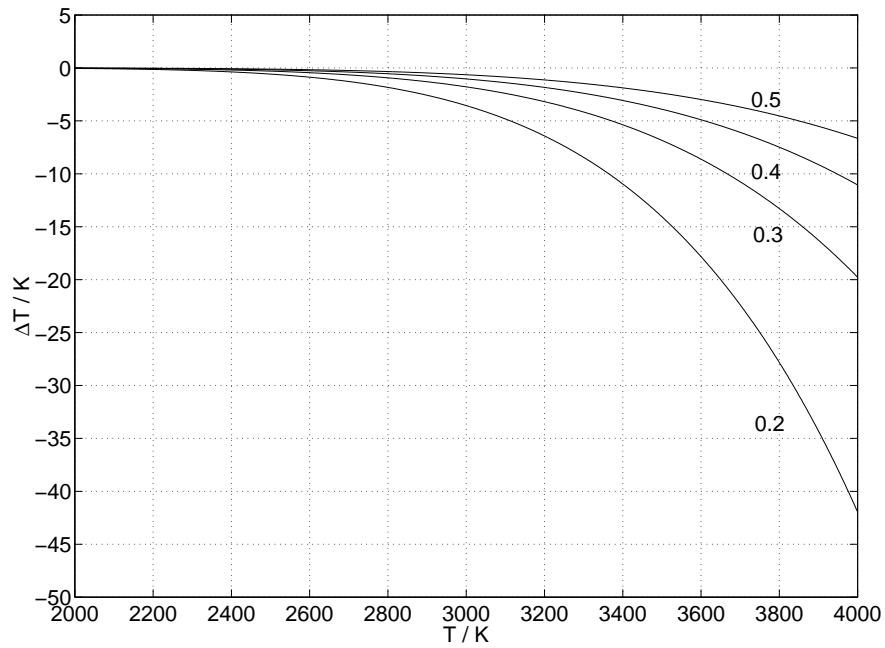


Figure 3.13: Difference of true temperature between calculations by means of Planck's radiation law (3.45) and Wien's approximation (3.50);
 parameter: emissivity $\epsilon = 0.2 \dots 0.5$
 centre wavelength $\lambda_0 = 710 \text{ nm}$
 ΔT : temperature difference; T : temperature.

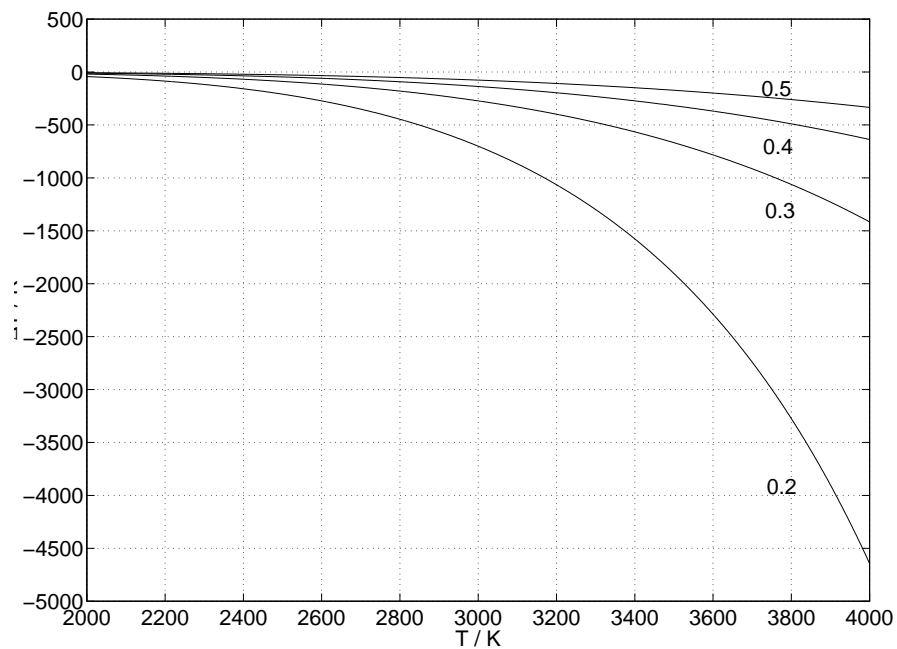


Figure 3.14: Difference of true temperature between calculations by means of Planck's radiation law (3.45) and Wien's approximation (3.50);
 parameter: emissivity $\epsilon = 0.2 \dots 0.5$
 centre wavelength $\lambda_0 = 1580 \text{ nm}$
 ΔT : temperature difference; T : temperature.

Chapter 4

Program HOTWIRE

HOTWIRE is intended for the evaluation of conventional pulse heating data as well as emissivity data from ellipsometry. As mentioned in the introduction, chapter 1, *HOTWIRE* operates in two modes:

- *HOTWIRE*-mode: Evaluation of pulse heating data without emissivity measurement. In this case temperature is calculated using the melting plateau as reference point. The general features of *HOTWIRE* are depicted in the next chapter.
- *DOAP*-mode: Evaluation of pulse heating data combined with emissivity measurement using a division-of-amplitude photopolarimeter (DOAP). In this case the temperature of the sample can be computed directly from radiance temperature using the emissivity data. The *DOAP*-mode is described in chapter 7.1.

4.1 HOTWIRE-mode

Conventional pulse heating data without emissivity measurement are evaluated in *HOTWIRE*-mode, which is described within this chapter.

Data acquisition is done by the software package INSIGHT¹ and delivers raw data in ASCII-format. These are current, voltage hot, voltage cold and intensity of radiation, sampled every 0.1 μs with a capacity of 4096 data points. The imported raw data are preprocessed within *HOTWIRE* in the following manner:

- *Offset correction*

The trigger pulse for data acquisition is typical 200 μs before the start of the experiment. This period is used to correct the offset by averaging the data during this time and subtracting the mean value from the entire signal.

- *Scaling*

Voltage hot, voltage cold and current signal are scaled using the experimental determined factors as mentioned in chapter 2.

- *Smoothing*

An averaging filter algorithm is used to smooth the input data if necessary.

¹INSIGHT v3.28d 12.03.97 von IMTEC, intelligente Messtechnik GmbH

In general *HOTWIRE* offers two kinds of graphical representations:

- Overview

Four graphs on the screen give an overview of thematically grouped data, for instance the raw data \Rightarrow voltage hot, voltage cold, current and intensity as shown in Fig. 4.1.

- Single

A single graph for a closer view and the possibility to zoom in. For an example see Fig. 4.2, which shows the typical current profile during the experiment.

The following list is a detailed description of all available data in *HOTWIRE*-mode. It is grouped in such a way, that to each overview the corresponding four single graphs are depicted. As an example there are some figures on the next pages showing data of an experiment on Niobium.

Input data: Raw data versus time delivered by the acquisition software

- *Voltage hot* \Rightarrow Fig. 4.3
- *Voltage cold* \Rightarrow Fig. 4.4
- *Current* \Rightarrow Fig. 4.5
- *Intensity signal* \Rightarrow Fig. 4.6

Enthalpy, spec. resistivity versus temperature

- *Radiance temperature* \Rightarrow Fig. 4.7
Computed according to equation (3.43)
- *Temperature* \Rightarrow Fig. 4.8
Determined using the melting plateau as reference point as described in chapter 4.4
- *Spec. enthalpy versus temperature* \Rightarrow Fig. 4.9
The specific enthalpy is computed after voltage correction using equation (3.35).
- *Spec. resistivity versus temperature* \Rightarrow Fig. 4.10
The spec. resistivity is computed after voltage correction using equation (3.38).

View/enthalpy, spec. resistivity versus time

- *Spec. enthalpy*
- *Spec. resistivity*
- *Spec. resistivity via spec. enthalpy*

View/additional data voltage correction

- *Enthalpy* \Rightarrow Fig. 4.11
Absolute value of enthalpy converted within the piece of wire between the two knife-edges.
- *Resistance* \Rightarrow Fig. 4.12
Absolute resistance of the piece of wire between the two knife-edges.
- *Error enthalpy corrected / uncorrected* \Rightarrow Fig. 4.13
Error which occurs if one would not perform the voltage correction. The enthalpy (3.35) is calculated once with corrected voltage $U_{S, corr}$ and the other time with uncorrected voltage U_S . Therefore the relative error ΔH_{rel} is given by

$$\Delta H_{rel} = \frac{H_{uncorrected} - H_{corrected}}{H_{corrected}} 100 \% \quad (4.1)$$

- *Error voltage corrected / uncorrected* \Rightarrow Fig. 4.14
Error which occurs if one would not perform the voltage correction. The corrected voltage is denoted by $U_{S, corr}$ and the uncorrected voltage by U_S . Therefore the relative error ΔU_{rel} is given by

$$\Delta U_{rel} = \frac{U_S - U_{S, corr}}{U_{S, corr}} 100 \% \quad (4.2)$$

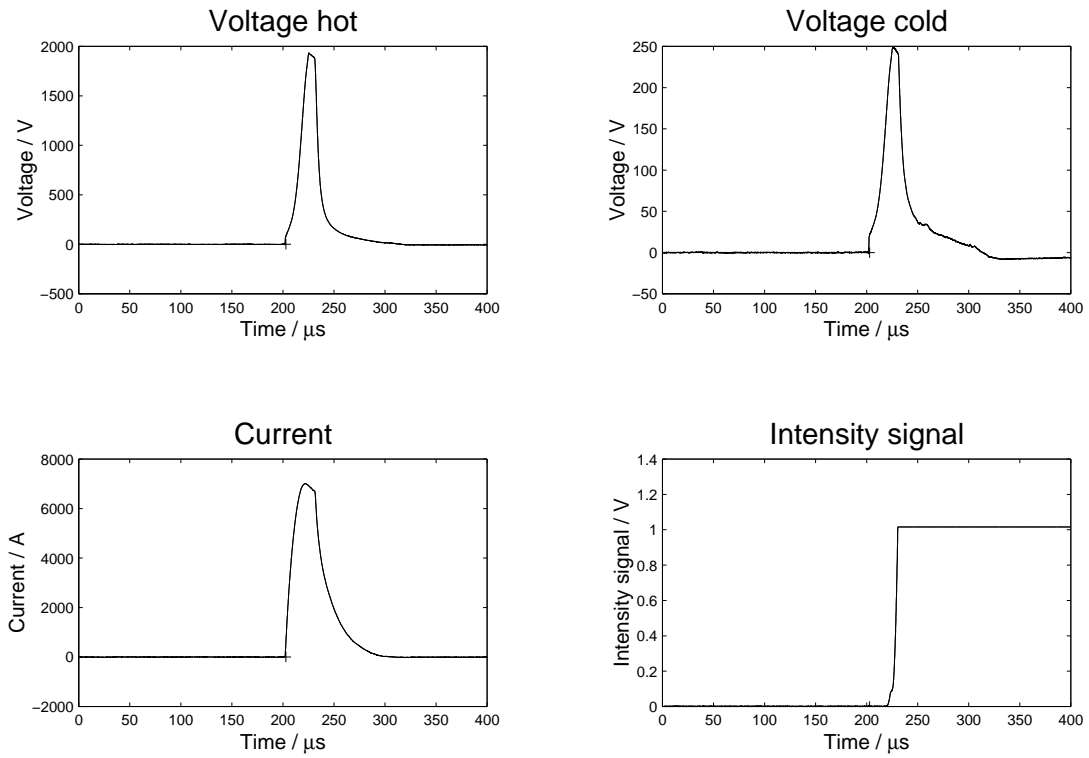


Figure 4.1: Graphical representation of input data voltage hot, voltage cold, current and intensity versus time in overview-mode;

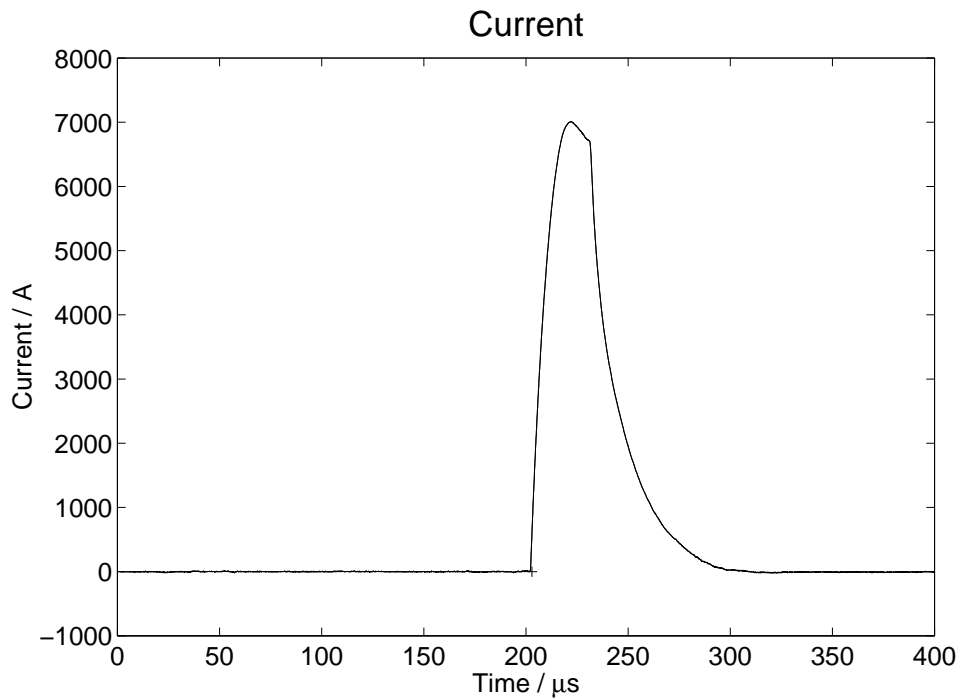


Figure 4.2: Graphical representation of input data current versus time in single-mode;

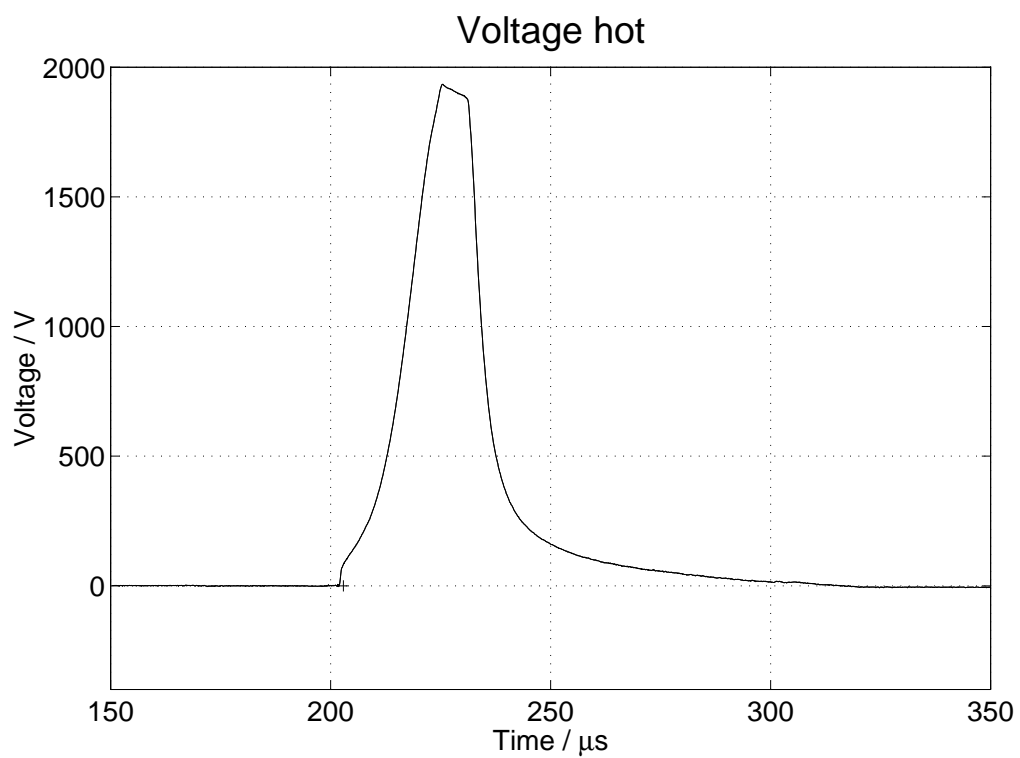


Figure 4.3: Raw data Niobium: voltage hot versus time

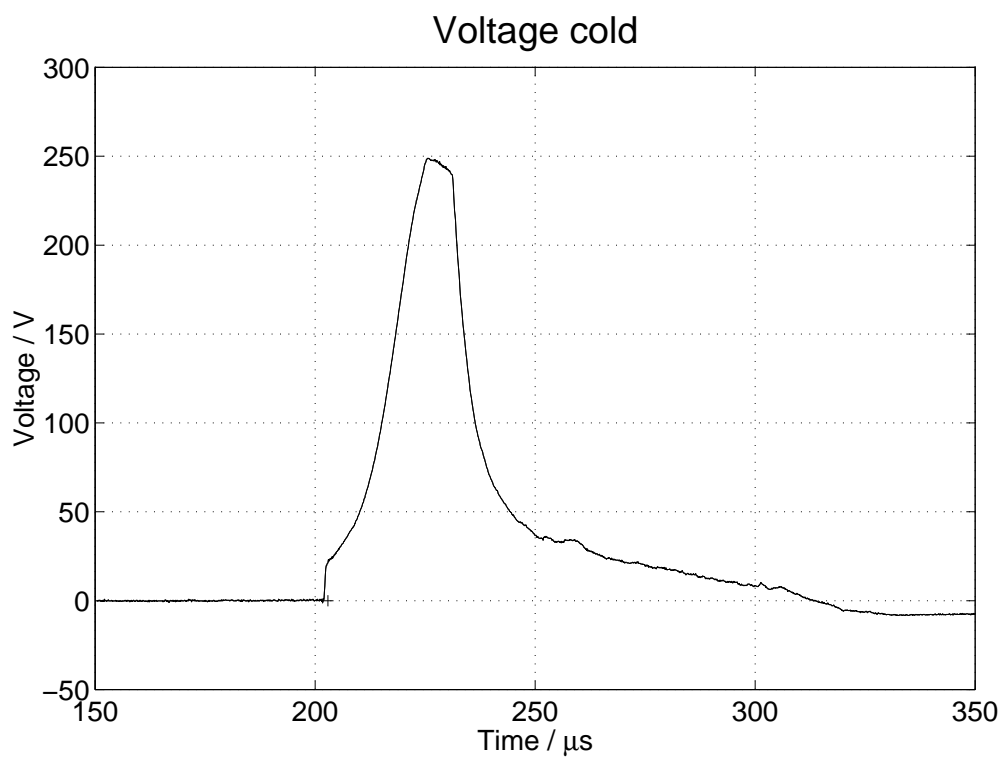


Figure 4.4: Raw data Niobium: voltage cold versus time

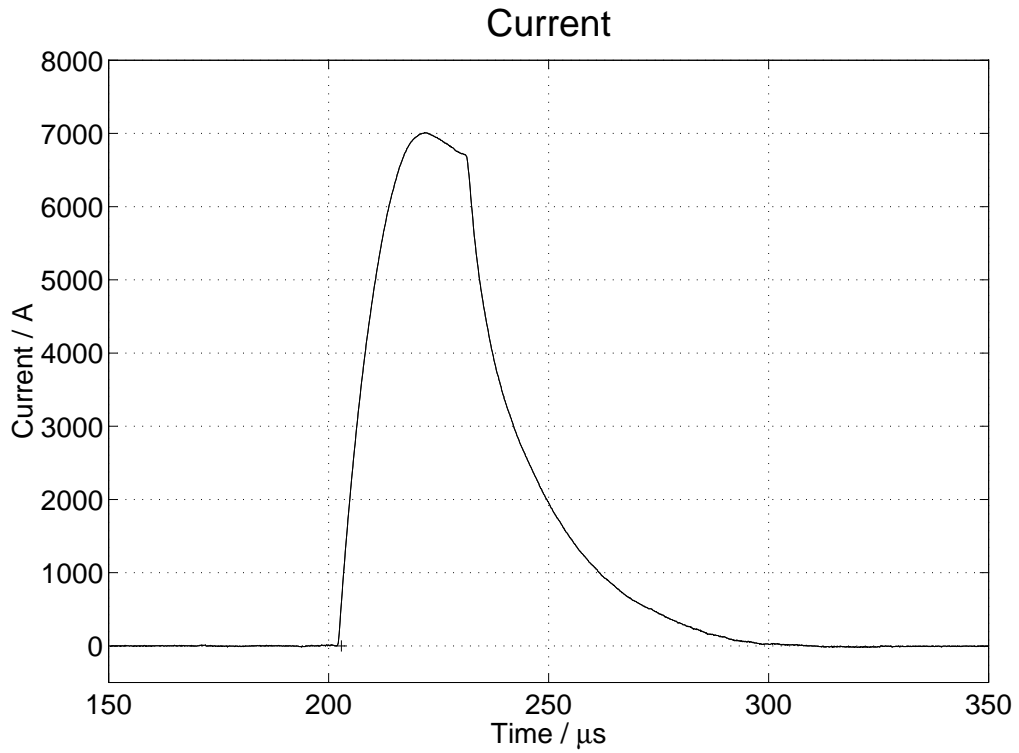


Figure 4.5: Raw data Niobium: current versus time

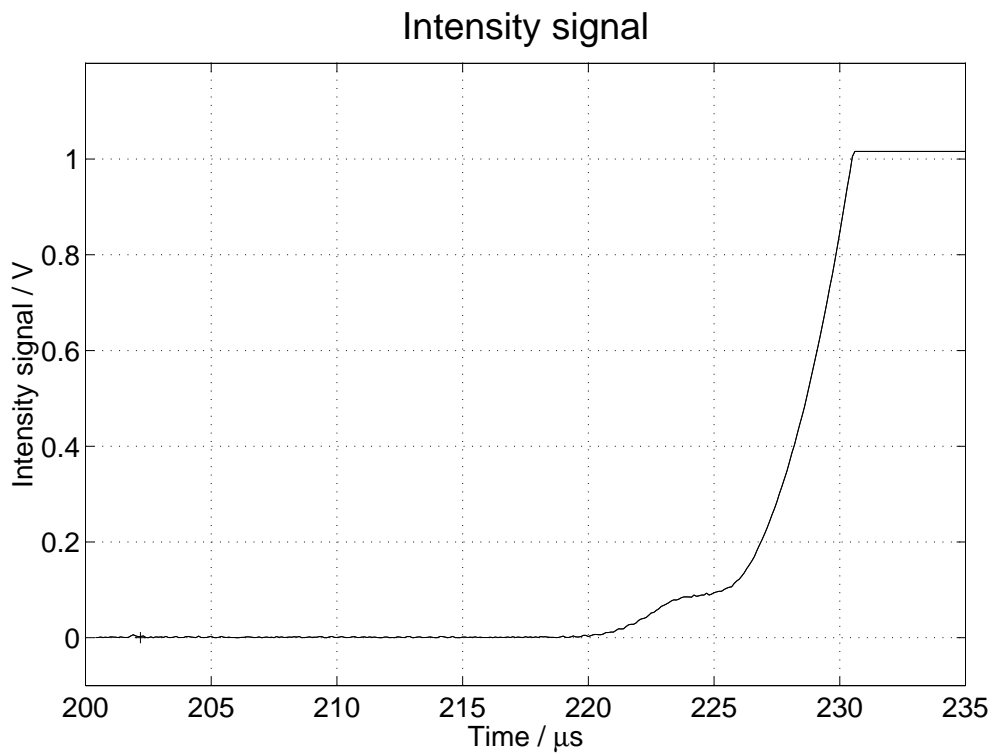


Figure 4.6: Raw data Niobium: intensity signal versus time

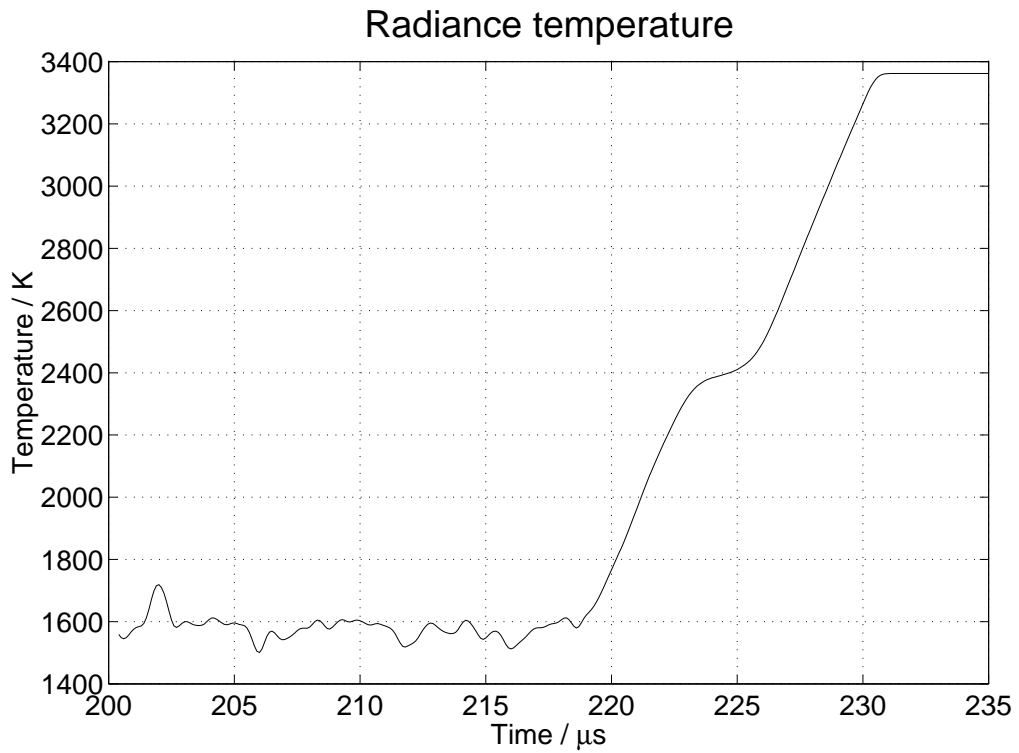


Figure 4.7: Evaluated data Niobium: radiance temperature versus time

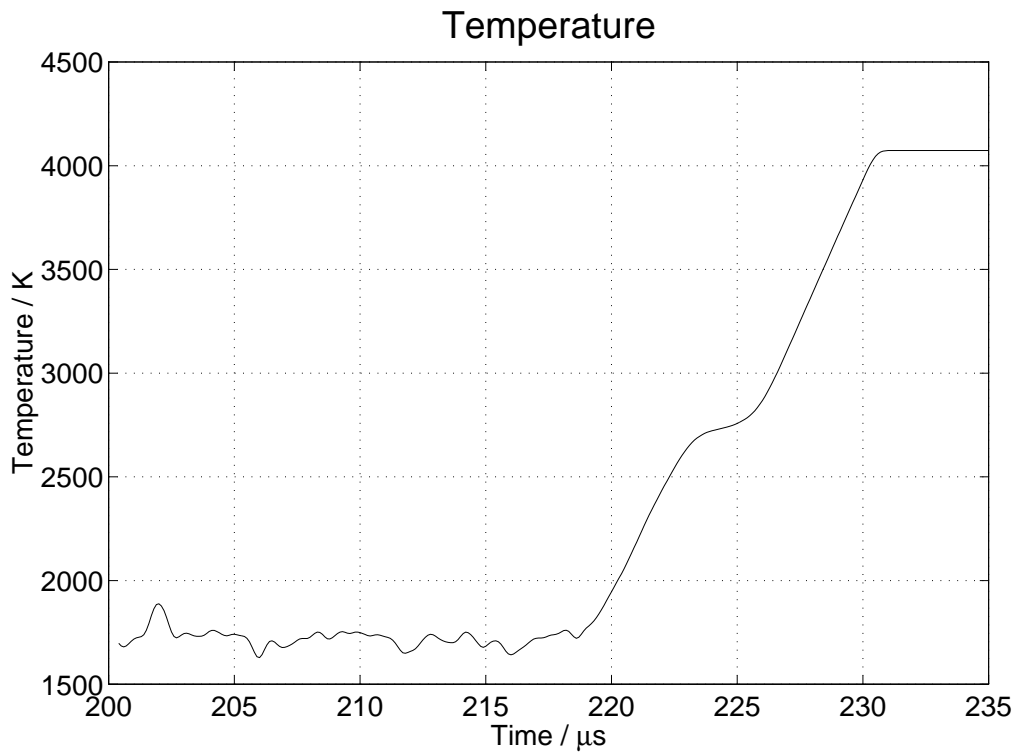


Figure 4.8: Evaluated data Niobium: temperature versus time

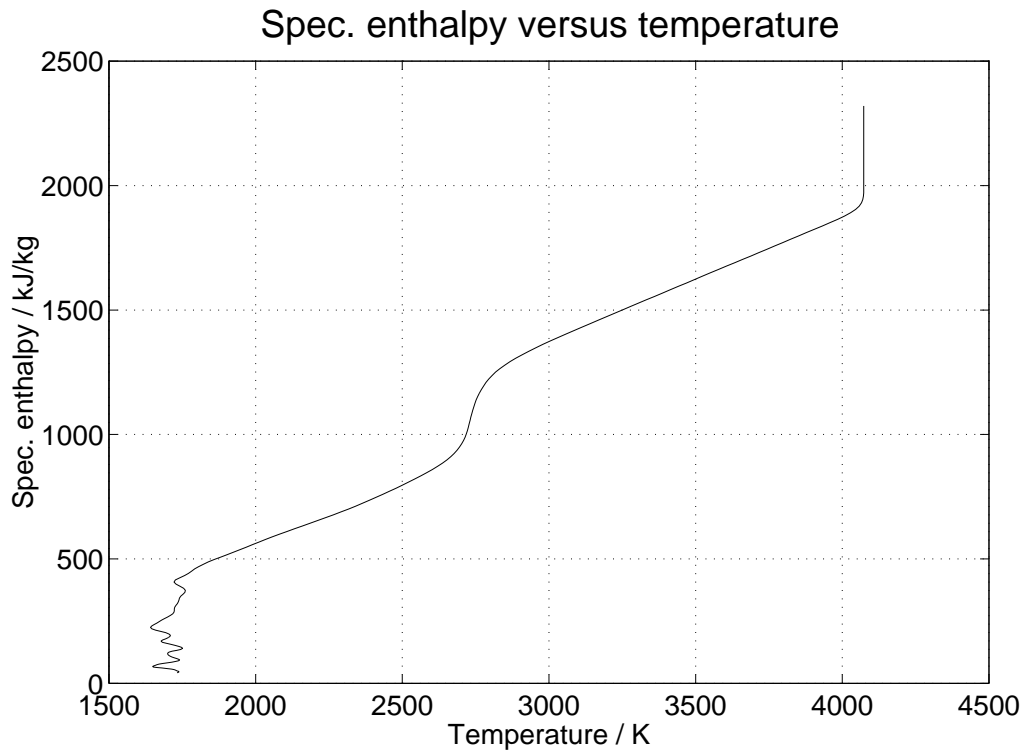


Figure 4.9: Evaluated data Niobium: specific enthalpy versus temperature

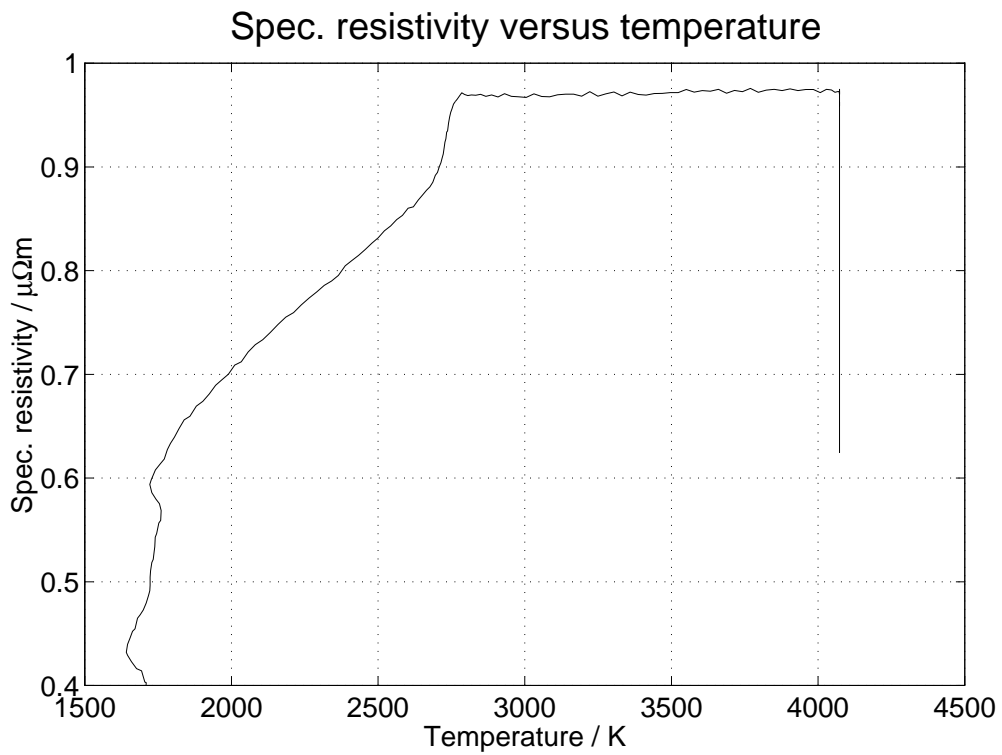


Figure 4.10: Evaluated data Niobium: specific resistivity versus temperature

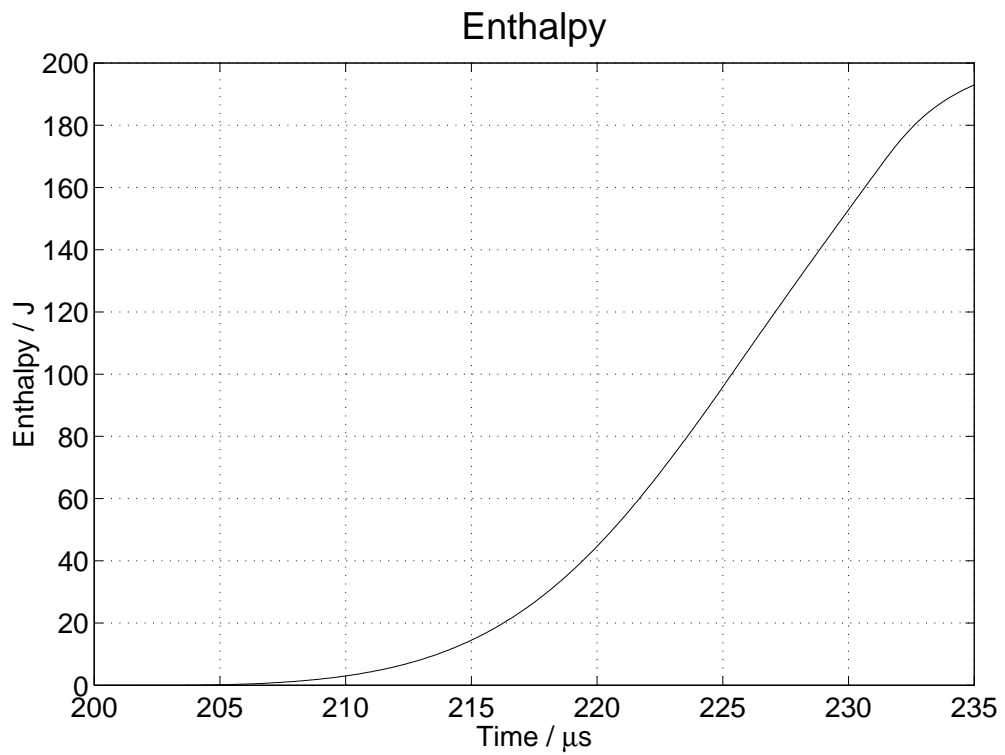


Figure 4.11: Evaluated data Niobium: absolute enthalpy of wire versus time

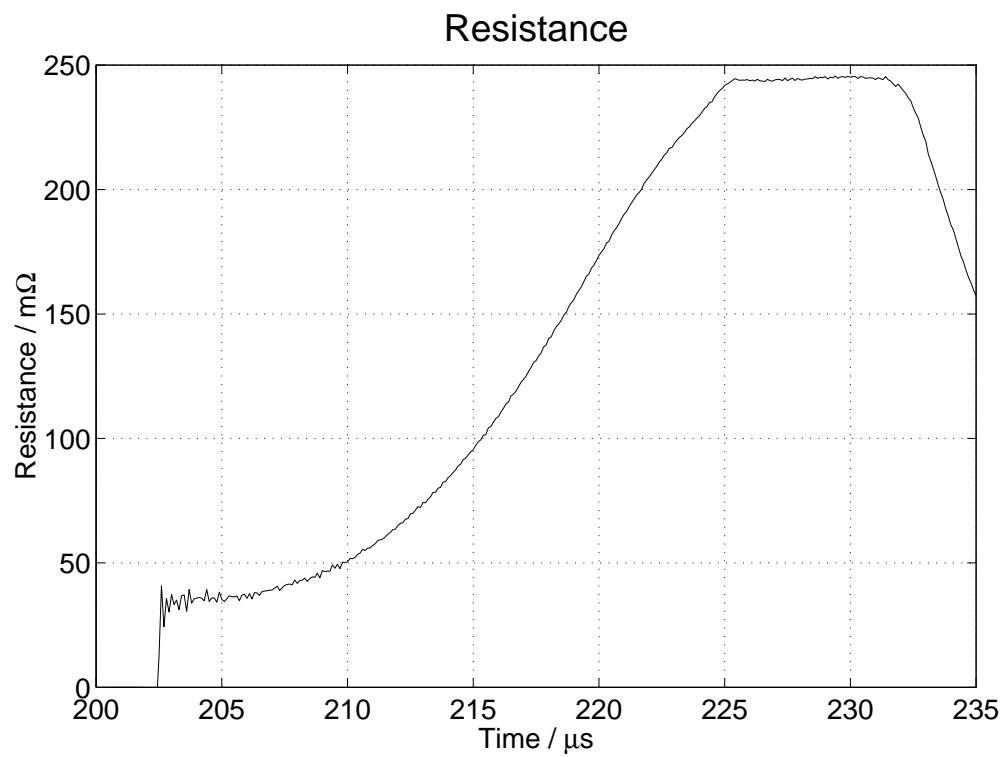


Figure 4.12: Evaluated data Niobium: resistance of wire versus time

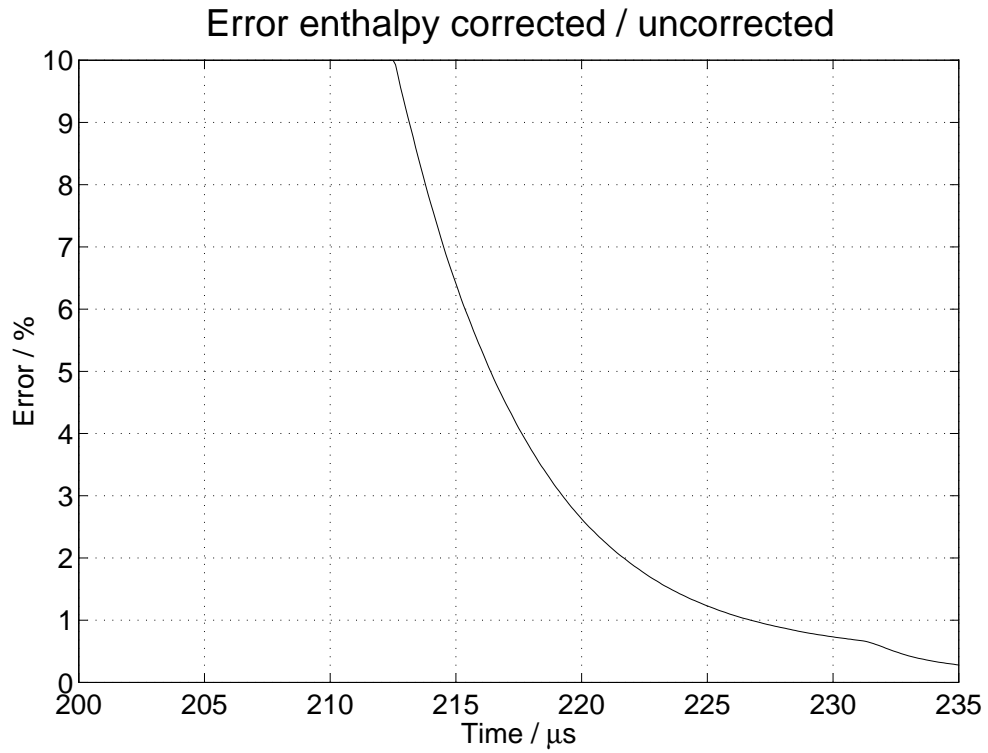


Figure 4.13: Evaluated data Niobium: relative error in specific enthalpy if the voltage correction is not performed

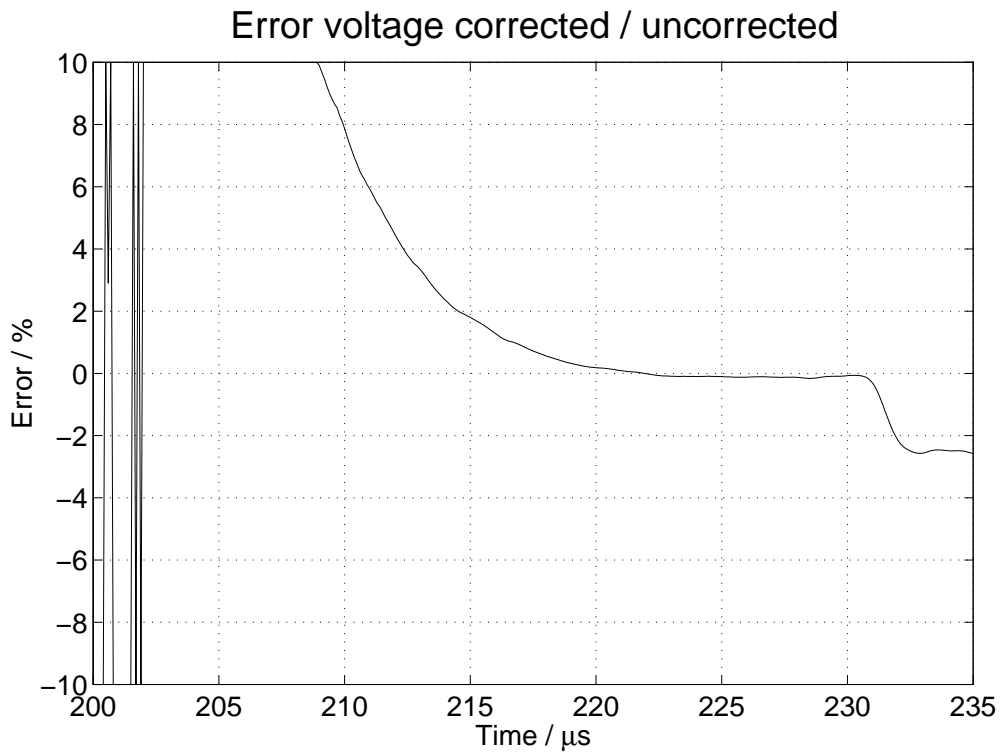


Figure 4.14: Evaluated data Niobium: relative error in voltage if the voltage correction is not performed

In the following chapters voltage correction and determination of temperature are described. When these procedures have been performed, the following data are saved by *HOTWIRE*:

- Time in μs
- Current in A
- Corrected voltage drop across the wire in V
- Radiance temperature in K
- Temperature in K
- Spec. enthalpy in kJ/kg
- Spec. resistivity in $\mu\Omega m$

Additional, a log-file is saved which contains all the parameters used during data evaluation. The log-file from the evaluated Niobium experiment looks like this:

```

HOTWIRE documentation file
Date: 02-May-2000
Time: 16:01:30
Rawdata-file:      nb0301-2.asc  11-Jan-2000 14:37:32
Result data-file: nb0301-2.dat  02-May-2000 16:01:32
Status: - HOTWIRE-mode
        - Manual voltage correction
Length of wire: 49.43 mm
Diameter of wire: 0.5 mm
Density of wire: 8570 kg/m^3
Melting temperature: 2741 K
Centre wavelength interference filter: 710 nm
Calibration factor K for temperature: 420.4 V
Loadvoltage: 5520 V
Voltage divider hot: 1029.4
Voltage divider cold: 309.4
Calibration factor current: 2483.5 A/V
Interval of used data points: [200, 235] us
Offset correction interval for intensity signal: [0, 199] us
Smoothing of input data:
    Voltage and current:  Filtertype:      Without
                        Filterparameter: 5
    Intensity pyrometer:  Filtertype:      Without
                        Filterparameter: 5
Filterparameter smoothing current for derivative: 5
Trigger point: 202.2 us
Crowbar: 232.3 us
Sample interval: 0.1 us
First derivative of current at t=0: 859 A/us
Maximum current: 7005 A
Time maximum current: 222 us
Wire inductance: 53.6 nH
Wire inductance per unit length: 1.08 nH/mm
Averaged spec. resistance of wire at start of experiment: 0.147 uOhmm

```

4.2 Voltage correction

This task is the main part of *HOTWIRE* in *HOTWIRE*-mode as well as in *DOAP*-mode. The theoretical considerations are described in chapter 3.2.

Beginning a new series of experiments the manual voltage correction has to be performed. During this procedure several parameters are stored and allow in the following an automatic voltage correction, as described in the subsequent chapter 4.2.2.

4.2.1 Manual voltage correction

The task is divided into several steps as depicted in the following.

- *Determination of beginning time and current gradient*

A polynomial of typical second order is fitted to the slope of the current. Two vertical marker lines show the range used for the fit, see Fig. 4.15. The result is shown in Fig. 4.16. The intersection of the polynomial with zero gives the exact beginning time t_0 and the first derivative at t_0 is the desired beginning gradient $\frac{dI}{dt}|_{t_0}$.

Additional, if the load voltage is known, the inductance of the whole discharge circuit can be calculated using expression 3.15.

Another possibility is to fit the current with the theoretical waveform equation (3.16). So parameters of the whole discharge circuit can be obtained as described in chapter 4.3.

- *First derivative of current*

Before differentiating there is the possibility of an additional smoothing of the current. This has proved to be necessary, if the raw data are not filtered at all. In *DOAP*-mode a data reduction algorithm is used (see chapter 7.1), which also smooths the input data. In this case the filter option must be switched off. The result is shown in Fig. 4.17.

- *Determination of voltage step and wire inductance*

The uncorrected voltage drop U_S is given by

$$U_S = U_{hot} - U_{cold} \quad (4.3)$$

U_{HOT} ... voltage hot

U_{COLD} ... voltage cold, see Fig. 2.1

A polynomial of typical second order is fitted to the beginning region of the voltage. Two vertical marker lines show the range used for the fit, see Fig. 4.18. The result is shown in Fig. 4.19. At t_0 the polynomial has the value U_0 which is the voltage step due to wire inductance L_S . Using equation (3.29) we obtain

$$L_S = \frac{U_0}{\frac{dI}{dt}|_{t=0}} \quad (4.4)$$

Finally the corrected voltage drop is given by expression (3.30), see also Fig. 4.20.

As described in chapter 3.2 the inductance per unit length $\frac{L_S}{l}$ is constant for wires of same diameter. The value gained within the last steps, as well as parameters for fitting are saved in a file and further can be used for automatic voltage correction.

- *Check voltage correction*

To check the performance of the last steps, the corrected voltage is plotted versus current (U/I-diagram). The slope is nothing else than the resistance of the sample and stays nearly constant during the first time. If a linear regression is applied during this period, the slope of the fitted straight line is the resistance R_0 at room temperature. The intercept d should be zero and is an assessment, how good the voltage correction has been performed. The range used for regression is given between two vertical marker lines, see Fig. 4.18. The result is shown in Fig. 4.19.

4.2.2 Automatic voltage correction

After performing the manual voltage correction the inductance per unit length $\frac{L_S}{l}$ and all the necessary parameters for fitting are saved in a file. Assuming $\frac{L_S}{l}$ doesn't change between different experiments, the wire inductance is simply gained by multiplication with the wire length l . This is the principle of the automatic voltage correction.

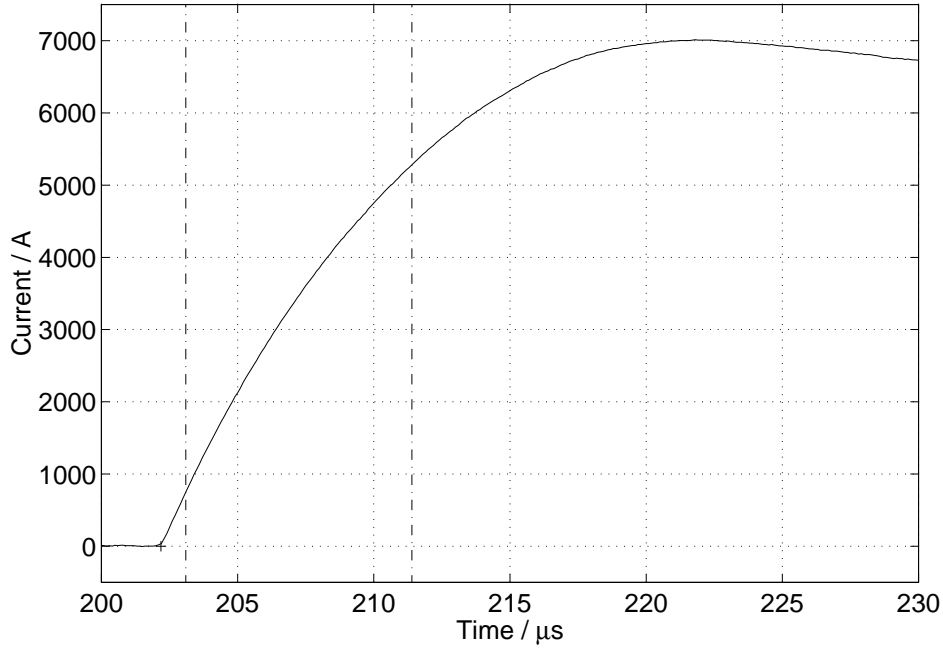


Figure 4.15: Voltage correction: between dotted lines \Rightarrow range for fitting slope of current

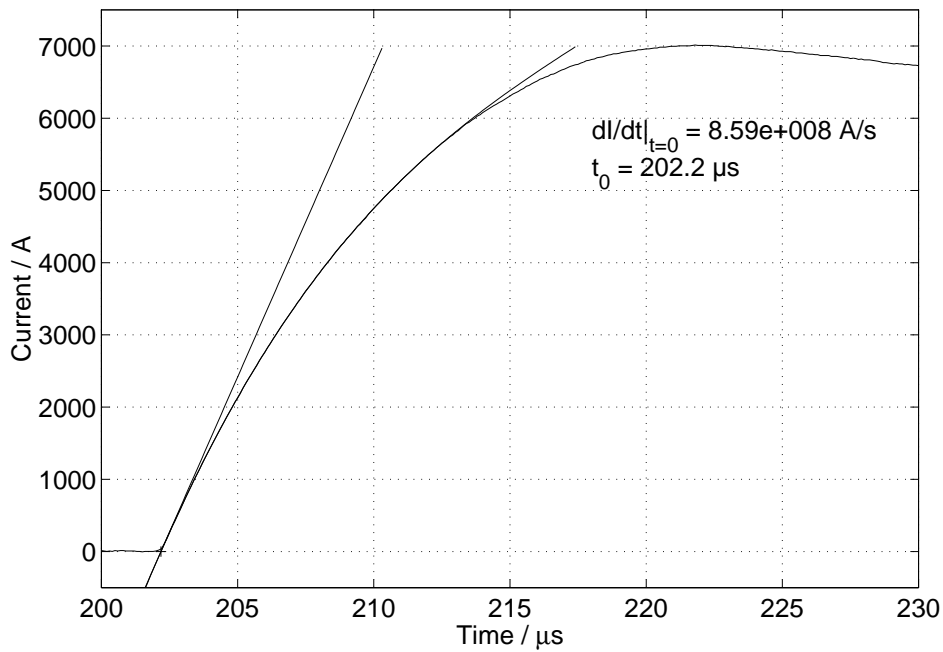


Figure 4.16: Voltage correction: result of fit and tangent at t_0
 t_0 : start of experiment; $\frac{dI}{dt}|_{t_0}$: beginning gradient of current.

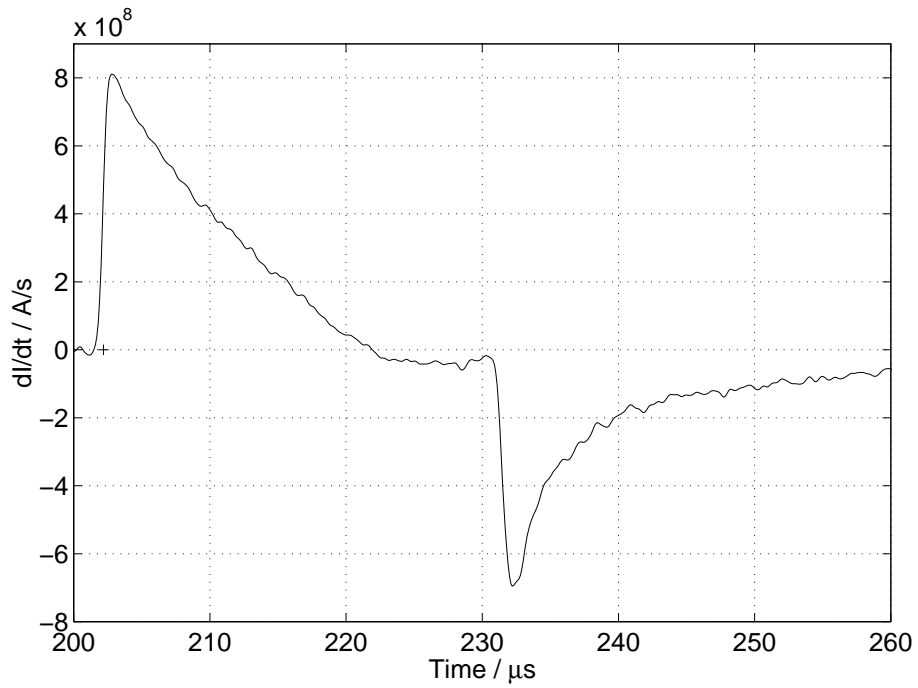


Figure 4.17: Voltage correction: first derivative of current $\frac{dI}{dt}$ versus time

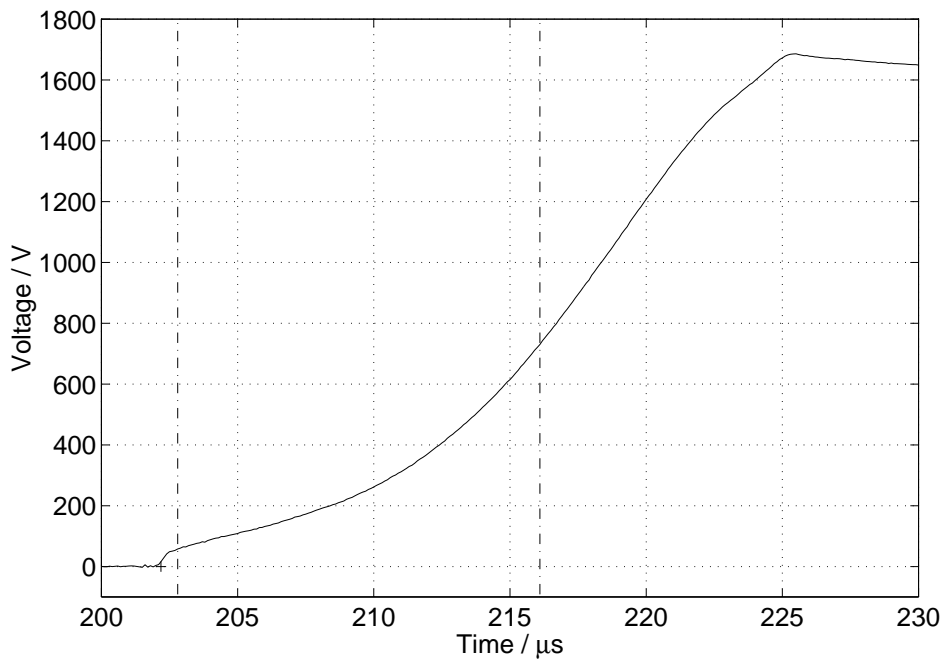


Figure 4.18: Voltage correction: between dotted lines \Rightarrow range for fitting to obtain the voltage step at beginning time t_0

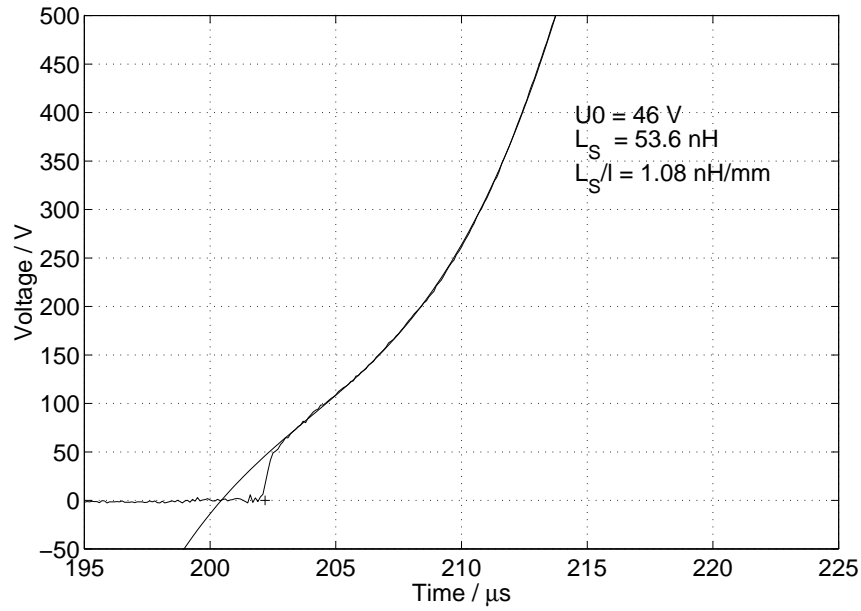


Figure 4.19: Voltage correction: result of fit to obtain the wire inductance

U_0 : voltage step at beginning time t_0 ; L_S : wire inductance;
 L_S/l : wire inductance per unit length.

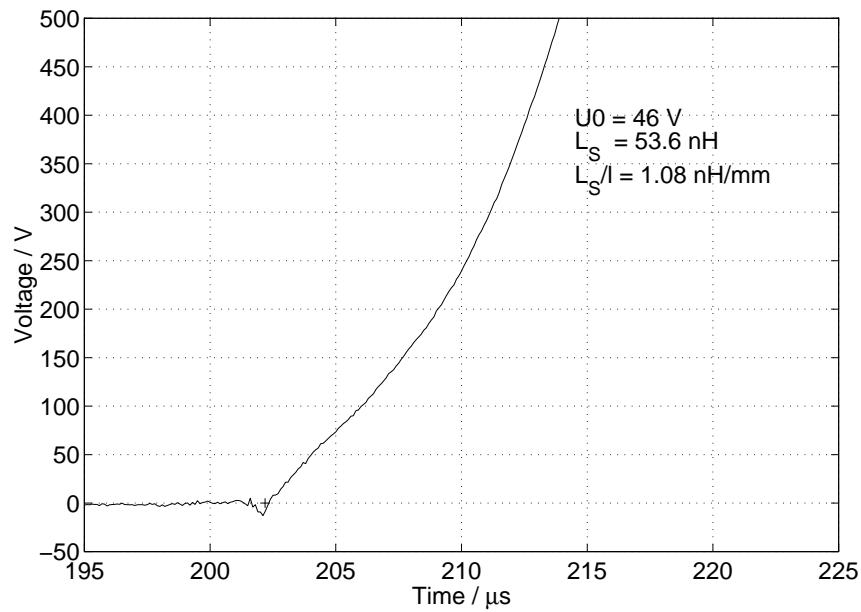


Figure 4.20: Voltage correction: corrected voltage versus time

U_0 : voltage step at beginning time t_0 ; L_S : wire inductance;
 L_S/l : wire inductance per unit length.

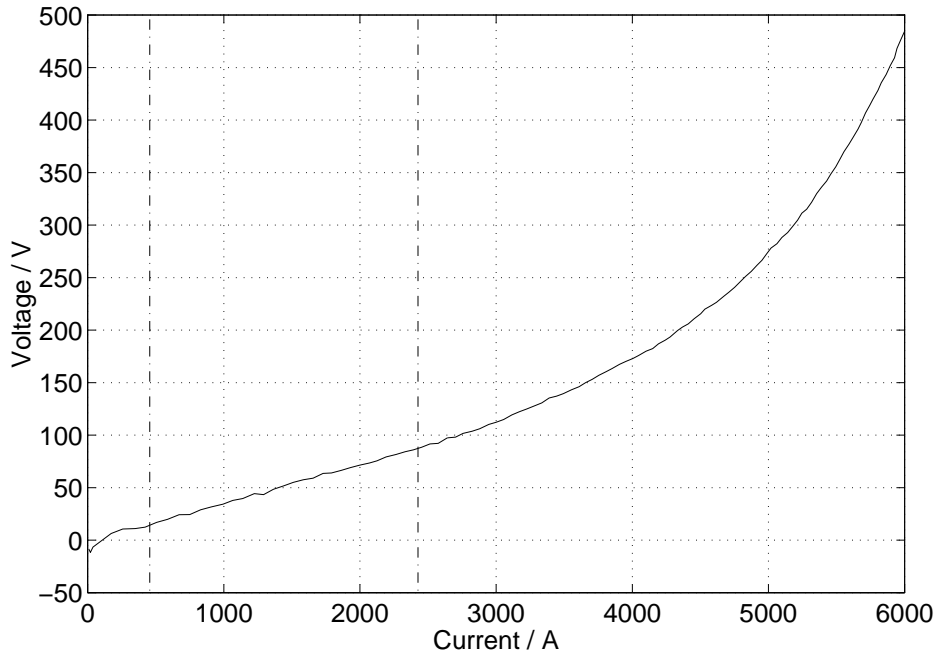


Figure 4.21: Voltage correction: between dotted lines \Rightarrow range for fitting in U/I-diagram

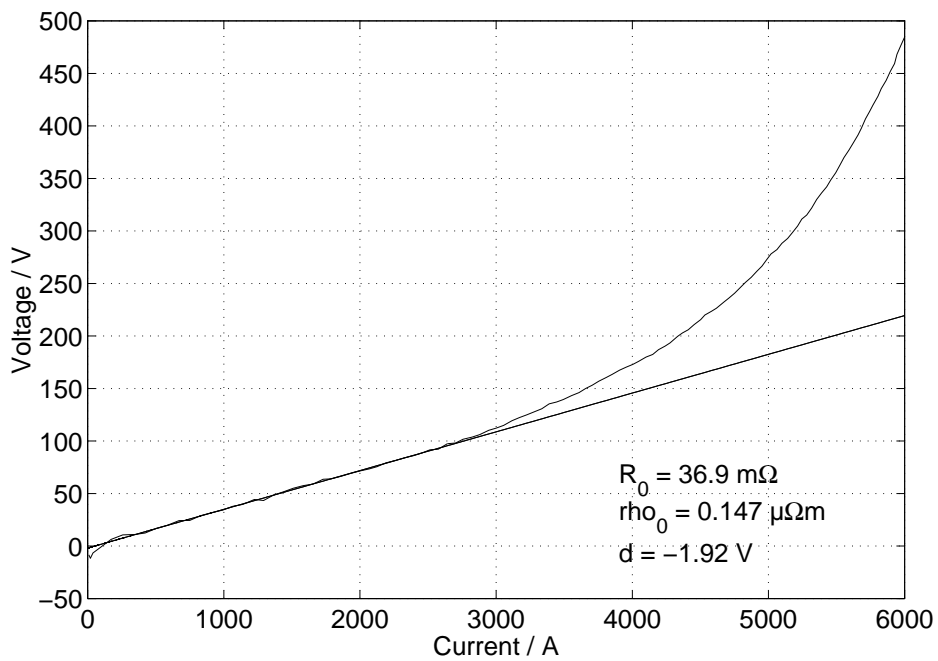


Figure 4.22: Voltage correction: result of fit in U/I-diagram
 R_0 : resistance at room temperature; d : intersection of linear fit.

4.3 Parameters of the whole discharge circuit

Using the concepts of chapter 3.1 it is possible to determine e.g. resistance and inductance of the whole discharge circuit. Therefore the current is fitted with the theoretical waveform, equation (3.16) in the form

$$I(t) = \frac{U_0}{\Omega L} e^{-\delta(t-t_0)} \sinh \Omega(t-t_0) \quad (4.5)$$

$$= \frac{U_0}{2\Omega L} \left[e^{-(\delta-\Omega)(t-t_0)} - e^{-(\delta+\Omega)(t-t_0)} \right] \quad (4.6)$$

$$= a \left[e^{-b(t-t_0)} - e^{-c(t-t_0)} \right] \quad (4.7)$$

with the parameters:

t_0 ... Start of experiment

$$a = \frac{U_0}{2\Omega L}$$

$$b = \delta - \Omega$$

$$c = \delta + \Omega$$

Using expressions (3.7) ... (3.9) and (3.15) we obtain

$$\left. \frac{dI}{dt} \right|_{t=0} = \frac{U_0}{L} = 2a\Omega = a(c-b) \quad (4.8)$$

$$L = \frac{U_0}{2a\Omega} = \frac{U_0}{a(c-b)} \quad (4.9)$$

$$R = 2L\delta = L(b+c) \quad (4.10)$$

$$C = \frac{1}{L(\delta^2 - \Omega^2)} = \frac{1}{Lbc} \quad (4.11)$$

In *HOTWIRE* these calculations are realized within the manual voltage correction as mentioned in the previous chapter.

Performing the fit on data of a "normal" experiment there are problems due to the increasing resistance of the sample during heating up. The capacity C of the capacitor bank is the most sensitive quantity and using an experiment on Niobium we find $C \approx 70 \mu F$ instead of about $500 \mu F$. Therefore this is not applicable to obtain reliable data. The way out is to short the discharge chamber or to use a thick metal wire as sample. Additionally, best results are obtained if the crowbar ignitron is not fired and a long period is recorded, as seen in Figure 4.23. This figure also shows the vertical marker lines to choose the fit range and Fig. 4.24 presents the result.

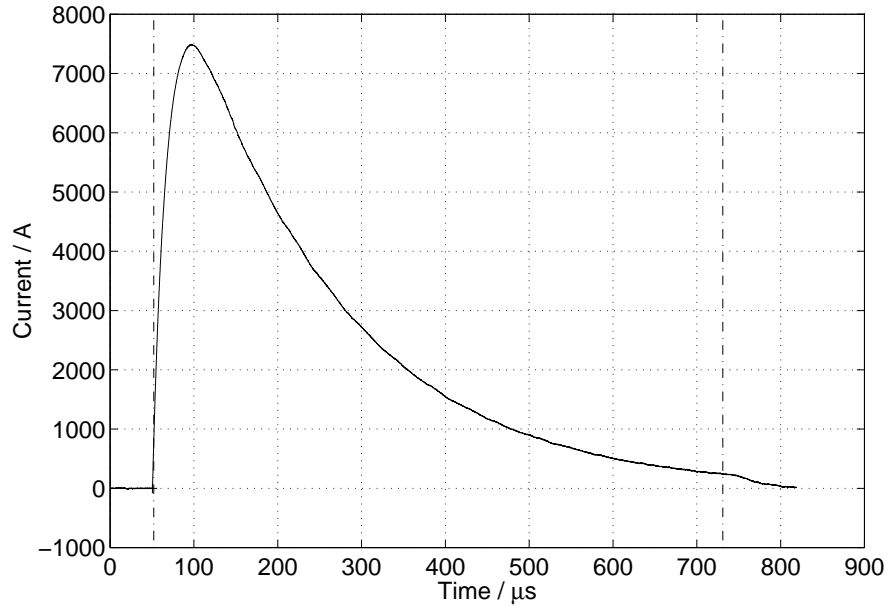


Figure 4.23: Parameters of discharge circuit: between dotted lines
 \Rightarrow range for fitting current

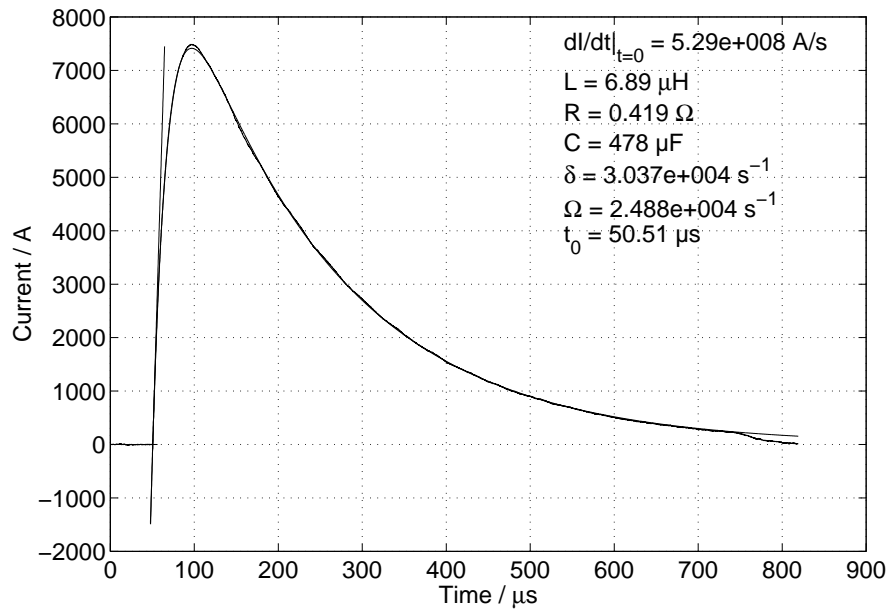


Figure 4.24: Parameters of discharge circuit: result of fit and tangent at t_0
 $\frac{dI}{dt}|_{t_0}$: beginning gradient of current; L : inductance; R : resistance; C : capacitance; δ : damping constant; Ω : angular frequency; t_0 : start of experiment.

4.4 Temperature via melting plateau

The theoretical part of temperature determination using the melting plateau as reference point is described in chapter 3.5 \Rightarrow *Melting plateau as reference point*. The task is divided into two steps, as depicted in the following:

1. Determination of melting plateau

The intensity signal shows a more or less marked melting plateau, see Fig. 4.25. In its middle a horizontal marker line must be positioned, which indicates the intensity signal at melting $U_D(T_M)$. From this the calibration factor K is computed by

$$K = U_D(T_M) \left(e^{\frac{c^2}{\lambda T_M}} - 1 \right) \quad (4.12)$$

2. Temperature

Using the calibration factor K the temperature is given by equation (3.43). The result is directly the true temperature of the wire sample, see Fig. 4.8.

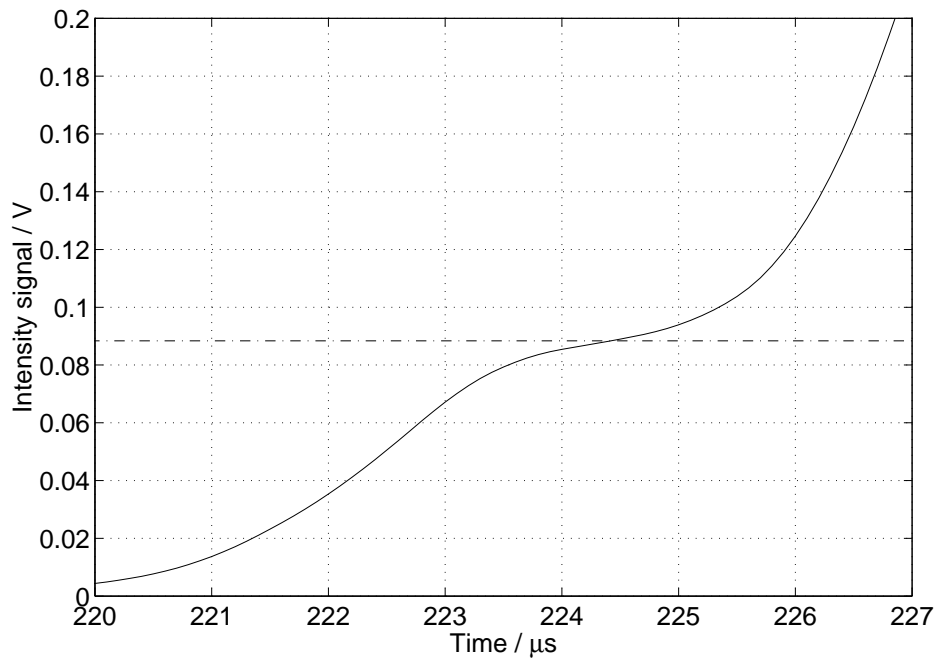


Figure 4.25: Determination of temperature: dotted lines \Rightarrow intensity value at melting

Chapter 5

Ellipsometry

The aim of applying ellipsometry to pulse heating experiments is to obtain emissivity data. So the relationship between emissivity and optical parameters gained by ellipsometry is explained in the following. A thorough discussion can be found in DeWitt [10].

Within an ideal blackbody the radiation field is in thermal equilibrium with the enclosure. This requires that their temperatures are equal. Regarding a point on the inner surface of the blackbody cavity the incident flux of radiation, coming from a given direction, is either reflected or absorbed. To maintain thermal equilibrium the same amount as absorbed has to be emitted in the same (but opposite) direction. Subsequently for a given direction (θ, ϕ) this gives

$$\epsilon(\theta, \phi) = \alpha(\theta, \phi) \tag{5.1}$$

$\epsilon(\theta, \phi)$... directional emissivity
 $\alpha(\theta, \phi)$... directional absorptance

The above considerations are based on a blackbody in thermal equilibrium. An extension is given by Kirchhoff's law which states that equation (5.1) is valid for any bodies and also non-equilibrium conditions.

The radiation balance for incident flux on a semitransparent material can be expressed as

$$\alpha + \rho + \tau = 1 \tag{5.2}$$

α ... absorptance
 ρ ... reflectance
 τ ... transmittance

The quantities α , ρ and τ depend not only on the direction of incident flux, but also on the directions of reflection and transmission. So this is rather complicated, but fortunately it becomes easier, if we only consider normal incidence. Additionally, for an opaque medium transmittance is equal to zero. Therefore normal emissivity $\epsilon(0)$ is obtained from the foregoing equations by

$$\epsilon(0) = \alpha(0) = 1 - \rho(0) \tag{5.3}$$

$\alpha(0)$... normal absorptance
 $\rho(0)$... normal reflectance

In chapter 5.6 we derive the relationship between normal reflectance $\rho(0)$ and the optical constants n_2 and k_2 , see equation (5.78).

$$\rho(0) = \frac{(n_1 - n_2)^2 + k_2^2}{(n_1 + n_2)^2 + k_2^2} \quad (5.4)$$

n_1 ... refractive index ambient

n_2 ... refractive index sample

k_2 ... extinction coefficient

From this normal emissivity is given by

$$\epsilon(0) = 1 - \rho(0) = \frac{4 n_1 n_2}{(n_1 + n_2)^2 + k_2^2} \quad (5.5)$$

This equation shows how emissivity is gained from refractive index n_2 and extinction coefficient k_2 of the material. The determination of these optical parameters in turn is standard task of ellipsometry.

The optical parameters, and therefore emissivity, depend strongly on the wavelength of the light used. Subsequently the foregoing equation is only valid in a narrow wavelength interval. This is denoted by the term *normal-spectral emissivity* and an additional λ in the suffix $\Rightarrow \epsilon_\lambda(0)$. In the experiment a laser at 684.4 nm is used, and therefore the above condition is well matched.

5.1 Polarized light

Light is a transversal electromagnetic wave and is fully described by Maxwell's equations. Beside its amplitude, frequency, wavelength, and direction of propagation, a further important property is the polarization of light. A detailed study to this topic is found e.g. by Azzam and Bashara [12] or by Collins [13]. The following chapters give a short overview and summarize the most important equations used in ellipsometry.

5.1.1 The plane wave

To describe the state of polarization we need the concept of a plane wave, which is one of the simplest solutions of Maxwell's equations. Following the notation given by Papoušek [11] the plane wave can be expressed in the general form

$$\begin{aligned}\mathbf{E}(\mathbf{r}, t) &= \mathbf{A} e^{-i\mathbf{k}\cdot\mathbf{r}} e^{i\omega t} \\ \mathbf{H}(\mathbf{r}, t) &= \frac{1}{\omega\mu_0\mu} (\mathbf{k} \times \mathbf{A}) e^{-i\mathbf{k}\cdot\mathbf{r}} e^{i\omega t} \\ &= \frac{1}{\omega\mu_0\mu} (\mathbf{k} \times \mathbf{E}(\mathbf{r}, t))\end{aligned}\tag{5.6}$$

and the additional conditions

$$\mathbf{k} \cdot \mathbf{k} = k^2 = \omega^2 \epsilon_0 \epsilon \mu_0 \mu \qquad \mathbf{A} \cdot \mathbf{k} = 0\tag{5.7}$$

\mathbf{E}	...	electric field vector
\mathbf{H}	...	magnetic field vector
\mathbf{A}	...	complex amplitude vector
μ_0	...	magnetic constant
μ	...	magnetic permeability
ϵ_0	...	electric constant
ϵ	...	complex electrical permittivity
\mathbf{k}	...	wave vector
$\mathbf{r} = (x, y, z)$...	radius vector
ω	...	angular frequency
t	...	time

where \cdot denotes the scalar product and \times the outer product of vectors.

At an instant t_0 the plane wave solution varies in space depending on the factor $e^{-i\mathbf{k}\cdot\mathbf{r}}$. Amplitude and phase are constant where $\mathbf{k}\cdot\mathbf{r} = \text{constant}$. This describes a plane of infinite extent perpendicular to the direction of propagation, therefore the name *plane wave*. For a non-absorptive medium it arises from (5.6) and (5.7), that magnetic and electric field are perpendicular to each other and also perpendicular to the direction of propagation. In the case of absorptive materials the wave vector k is complex and the situation is much more complicated. So in the following we only consider weak or non-absorptive media.

The magnetic field is uniquely determined by the electric field. So it is usual only to use the electric field for investigations concerning the state of polarization. A further

simplification is to choose the reference frame in a way, that the z -axes is identical to the direction of propagation. In this case (5.6) reduces to

$$\begin{aligned} E_x(z, t) &= A_x e^{-ik_z z} e^{i\omega t} \\ E_y(z, t) &= A_y e^{-ik_z z} e^{i\omega t} \\ E_z(z, t) &= 0 \end{aligned} \quad (5.8)$$

or without complex notation

$$\begin{aligned} e_x(z, t) &= E_x^0 \sin(\omega t + k_z z + \varphi_x) \\ e_y(z, t) &= E_y^0 \sin(\omega t + k_z z + \varphi_y) \\ e_z(z, t) &= 0 \end{aligned} \quad (5.9)$$

$e_x, e_y, e_z \dots$ instantaneous values of electric field

$E_x^0, E_y^0 \dots$ (real) amplitudes of electric field

It is convenient to introduce the quantities α and δ defined by

$$\tan \alpha := \frac{E_y^0}{E_x^0} \quad \delta := \varphi_y - \varphi_x \quad (5.10)$$

where α is the angle between x - and y -component as shown in Fig. 5.1, and δ is the phase difference between these two components. Rewriting equation (5.9) and omitting a general phase factor, which has no influence to the state of polarization, we obtain

$$\begin{aligned} e_x(z, t) &= E^0 \cos \alpha \sin(\omega t + k_z z) \\ e_y(z, t) &= E^0 \sin \alpha \sin(\omega t + k_z z + \delta) \\ e_z(z, t) &= 0 \end{aligned} \quad (5.11)$$

where

$$E^0 = \sqrt{(E_x^0)^2 + (E_y^0)^2} \quad (5.12)$$

Subsequently the state of polarization is uniquely determined by two parameters α and δ . Amplitude, frequency and wave vector also characterize the plane wave, but they don't contribute to the representation of the state of polarization.

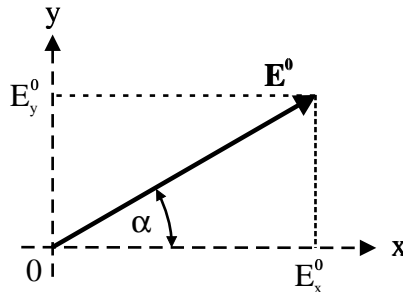


Figure 5.1: Definition of parameter α

$\mathbf{E}^0 = (E_x^0, E_y^0)$: vector of electric field; x, y : reference frame of observer.

The energy flow within the plane wave is represented by the Poynting vector \mathbf{S} which is defined in complex notation by

$$\langle \mathbf{S} \rangle = \frac{1}{2} \text{Re} \{ \mathbf{E} \times \mathbf{H}^* \} \quad (5.13)$$

where $*$ means the complex conjugate, $\text{Re}\{\}$ the real part and $\langle \rangle$ time averaging. The absolute value of the Poynting vector gives the intensity of light (energy per unit time and per unit cross sectional area) and it points in the direction of propagation.

Inserting equation (5.6) we obtain

$$\langle \mathbf{S} \rangle = \text{Re} \{ \mathbf{k} (\mathbf{A} \cdot \mathbf{A}^*) - \mathbf{A} (\mathbf{k} \cdot \mathbf{A}^*) \} \frac{e^{2z \text{Im}\{k_z\}}}{2\omega \mu_0 \mu} \quad (5.14)$$

where $\text{Im}\{\}$ means the imaginary part. For non-absorptive media the wave vector \mathbf{k} is a real quantity, and because of (5.7) we get

$$\mathbf{k} \cdot \mathbf{A}^* = (\mathbf{k}^* \cdot \mathbf{A})^* = (\mathbf{k} \cdot \mathbf{A})^* = 0 \quad (5.15)$$

In the special case of propagation along the z-axis \mathbf{k} is represented by

$$\begin{aligned} \mathbf{k} &= k_z \mathbf{e}_z^0 \\ \mathbf{e}_z^0 &\dots \text{ unit vector in z-direction} \end{aligned} \quad (5.16)$$

and inserting in 5.14 we obtain

$$\langle \mathbf{S} \rangle = \frac{k_z}{2\omega \mu_0 \mu} (A_x A_x^* + A_y A_y^*) \mathbf{e}_z^0 \quad (5.17)$$

In non-absorptive media is $k^2 = \omega^2 \varepsilon_0 \varepsilon \mu_0 \mu$ where ε is the electrical permittivity of the material. The phase velocity v of the plane wave is given by

$$v = \frac{\omega}{k} = \frac{1}{\sqrt{\varepsilon_0 \mu_0 \varepsilon \mu}} = \frac{c}{\sqrt{\varepsilon \mu}} = \frac{c}{n} \quad (5.18)$$

c ... velocity of light in vacuum

n ... refractive index

Using these relationships and $|A_x|^2 + |A_y|^2 = (E_x^0)^2 + (E_y^0)^2 = (E^0)^2$ we finally come to

$$\langle \mathbf{S} \rangle = \frac{1}{2} \frac{c}{n} \varepsilon_0 \varepsilon (E^0)^2 \mathbf{e}_z^0 \quad (5.19)$$

For absorptive media the situation is much more complicated. The electrical permittivity is complex and consequently the refractive index, which in turn can be divided up in a real and an imaginary part, is defined by

$$\eta = \sqrt{\varepsilon \mu} = n - ik \quad (5.20)$$

η ... complex refractive index

n ... real refractive index

k ... extinction coefficient

Now equation (5.15) is no longer valid and even the unit vector in the direction of propagation becomes complex (see Papoušek [11]). For the further considerations we always assume the ambient medium, in which the light wave propagates, to be non-absorptive. So the above formalism is sufficient to cover the field of ellipsometry.

5.1.2 The polarization ellipse

Eliminating time- and space-dependency ($\omega t + k_z z$) from expression (5.11) we come to

$$\frac{e_x^2}{(E^0)^2 \cos^2 \alpha} + \frac{e_y^2}{(E^0)^2 \sin^2 \alpha} - \frac{2 e_x^2 e_y^2 \cos \delta}{(E^0)^2 \sin \alpha \cos \alpha} = \sin^2 \delta \quad (5.21)$$

This is the equation of an ellipse in general location, the so called polarization ellipse. As shown in Fig. 5.2 it is characterized by two angles Ψ and χ . The first parameter Ψ describes the rotation of the axes to the reference frame, and the second parameter χ the ellipticity.

The formation of the polarization ellipse is described by the end points of the electric vector, looking in the direction from which the light is coming. If the ellipse is formed in clockwise sense, the polarization is called *right-handed* and refers to a positive ellipticity ($0 < \chi \leq \frac{\pi}{4}$). In the other case of *left-handed* polarization, the electric vector passes the ellipse in the counterclockwise sense and this refers to negative χ -values ($-\frac{\pi}{4} < \chi \leq 0$).

The relationship between the angles Ψ , χ and the parameters α and δ (defined in (5.10)) are given by (see e.g. Collins [13])

$$\tan 2\Psi = \tan 2\alpha \cos \delta \quad 0 \leq \Psi < \pi \quad (5.22)$$

$$\sin 2\chi = \sin 2\alpha \sin \delta \quad -\frac{\pi}{4} < \chi \leq \frac{\pi}{4} \quad (5.23)$$

In turn there are two parameters Ψ and χ which determine the state of polarization unambiguously.

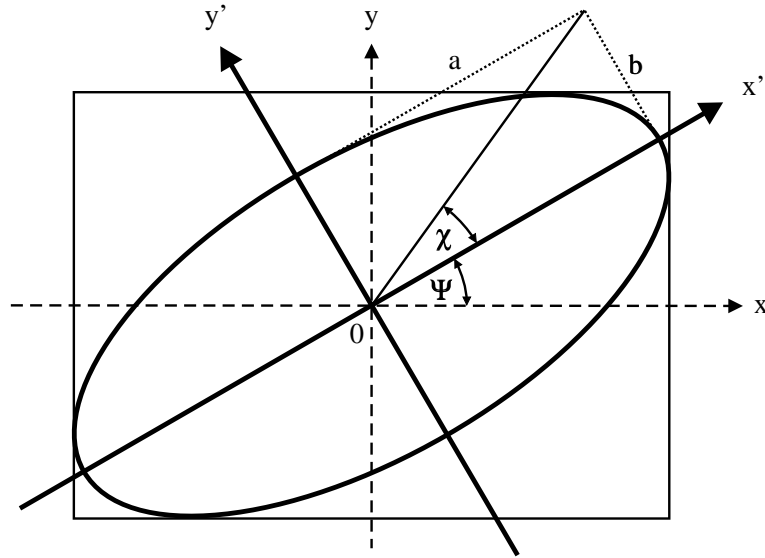


Figure 5.2: Polarization ellipse: The state of polarization is characterized by the angle of rotation Ψ and the ellipticity χ . a, b : major and minor axes; x, y : reference frame of observer; x', y' : reference frame with respect to the polarization ellipse.

5.1.3 The Jones vector and Jones matrix calculus

The concept of a plane wave given in chapter 5.1.1 can still be extended to a convenient mathematical description of the polarizing behavior, the so called Jones matrix calculus. First the state of polarization is represented by the Jones vector \mathbf{J} , which is achieved from equation (5.8) by suppressing the propagator $(\omega t + k_z z)$

$$\mathbf{J} = \begin{pmatrix} A_x \\ A_y \end{pmatrix} = \begin{pmatrix} E_x^0 e^{i\varphi_x} \\ E_y^0 e^{i\varphi_y} \end{pmatrix} \quad (5.24)$$

The intensity of light is the absolute value of the Poynting vector and is calculated using expressions (5.19) and (5.12)

$$I = |\langle \mathbf{S} \rangle| = \frac{1}{2} \frac{c}{n} \varepsilon_0 \varepsilon \begin{pmatrix} A_x^* & A_y^* \end{pmatrix} \begin{pmatrix} A_x \\ A_y \end{pmatrix} = \frac{1}{2} \frac{c}{n} \varepsilon_0 \varepsilon \mathbf{J}^\dagger \mathbf{J} \quad (5.25)$$

where \dagger means complex transposition.

Within the Jones matrix calculus polarizing elements are described by 2×2 -matrices. So the change in state of polarization, when light passes an optical device, is simply calculated by matrix multiplication of the Jones vector \mathbf{J} of the incident beam and the Jones matrix \mathbf{M} according to the device

$$\mathbf{J}' = \mathbf{M} \mathbf{J} \quad (5.26)$$

$$\begin{pmatrix} J'_1 \\ J'_2 \end{pmatrix} = \begin{pmatrix} M_{11} & M_{12} \\ M_{21} & M_{22} \end{pmatrix} \begin{pmatrix} J_1 \\ J_2 \end{pmatrix}$$

This formalism must be used, if there are interference effects between different light beams, e.g. in an interferometer. In this case the amplitudes have to be added first, before calculating the intensity.

For conventional ellipsometry the Jones matrix calculus has mainly two disadvantages:

- it is only applicable to completely polarized light
- one only can measure intensities and not amplitudes

As we have seen in the foregoing chapters, two parameters for the complex amplitudes suffice to describe the state of polarization unambiguously. Subsequently, measuring intensities we will need one more parameter due to the loss of phase information.

5.2 Stokes parameters, Mueller matrix and Poincaré sphere

In 1852 Stokes proofed that the measurement of four intensities suffices to obtain the state of polarization unambiguously. He developed a formalism using the Stokes parameters S_0 to S_3 to describe not only completely polarized light, but also unpolarized and partially polarized light as well. The four parameters become combined to the so called Stokes vector, which is defined by

$$\mathbf{S} = \begin{pmatrix} S_0 \\ S_1 \\ S_2 \\ S_3 \end{pmatrix} = \begin{pmatrix} I_{tot} \\ I_0 - I_{90} \\ I_{+45} - I_{-45} \\ I_{rcp} - I_{lcp} \end{pmatrix} \quad (5.27)$$

I_{tot}	...	total intensity
$I_0 - I_{90}$...	difference in intensities between horizontal and vertical linearly polarized components
$I_{+45} - I_{-45}$...	difference in intensities between linearly polarized components oriented at $+45^\circ$ and -45°
$I_{rcp} - I_{lcp}$...	difference in intensities between right and left circularly polarized components

As depicted in chapter 5.1.1, the intensity of light is equal to the absolute value of the time averaged Poynting vector. From this it can be shown, that the *Stokes vector for completely polarized light* is given by (see e.g. Collins [13])

$$\mathbf{S} = \frac{1}{2} \frac{c}{n} \varepsilon_0 \varepsilon \begin{pmatrix} A_x A_x^* + A_y A_y^* \\ A_x A_x^* - A_y A_y^* \\ A_x A_y^* + A_y A_x^* \\ i(A_x A_y^* - A_y A_x^*) \end{pmatrix} = \frac{1}{2} \frac{c}{n} \varepsilon_0 \varepsilon \begin{pmatrix} (E_x^0)^2 + (E_y^0)^2 \\ (E_x^0)^2 - (E_y^0)^2 \\ 2E_x^0 E_y^0 \cos \delta \\ 2E_x^0 E_y^0 \sin \delta \end{pmatrix} \quad (5.28)$$

Using expressions (5.11), (5.22) and (5.23) we also find

$$\mathbf{S} = I_0 \begin{pmatrix} 1 \\ \cos 2\alpha \\ \sin 2\alpha \cos \delta \\ \sin 2\alpha \sin \delta \end{pmatrix} = I_0 \begin{pmatrix} 1 \\ \cos 2\chi \cos 2\Psi \\ \cos 2\chi \sin 2\Psi \\ \sin 2\chi \end{pmatrix} \quad (5.29)$$

where the total intensity I_0 is given by

$$I_0 = |\langle \mathbf{S} \rangle| = \frac{1}{2} \frac{c}{n} \varepsilon_0 \varepsilon (E^0)^2 \quad (5.30)$$

Usually, only the state of polarization is of interest. Therefore the total intensity I_0 is omitted in the above equations and we get the normalized Stokes vector of polarized light where $S_0 = 1$. This is the most customary form normally used. For completely polarized light we find in this way

$$\sqrt{S_1^2 + S_2^2 + S_3^2} = 1 \quad (5.31)$$

As examples for the representation of polarized light in terms of Stokes vectors we consider in the following the most important states of polarization.

- Linear polarized light

For linear polarized light the phase difference δ between x - and y -component of the electrical field is zero. Inserting in equation (5.29) we find

$$\mathbf{S} = \begin{pmatrix} 1 \\ \cos 2\alpha \\ \sin 2\alpha \\ 0 \end{pmatrix} \quad (5.32)$$

where α describes the ratio of x - and y -amplitudes, see Fig. 5.1.

Special cases are:

- Horizontal (+) and vertical (–) polarized light

$$\mathbf{S} = \begin{pmatrix} 1 \\ \pm 1 \\ 0 \\ 0 \end{pmatrix} \quad (5.33)$$

- Linear polarized light oriented at $+45^\circ$ (+) and -45° (–)

$$\mathbf{S} = \begin{pmatrix} 1 \\ 0 \\ \pm 1 \\ 0 \end{pmatrix} \quad (5.34)$$

- Circularly polarized light

For circularly polarized light the ellipticity angle of the polarization ellipse is equal to $\pm\pi/4$. Inserting in equation (5.29) we find

$$\mathbf{S} = \begin{pmatrix} 1 \\ 0 \\ 0 \\ \pm 1 \end{pmatrix} \quad (5.35)$$

where + is for right circularly polarized (rcp) and – for left circularly polarized (lcp).

Unpolarized light can be seen as a statistical mixture of all possible states of polarization. In this case the intensities of different states are equal, and consequently the terms in S_1 to S_3 of equation (5.27) cancel out. The *normalized Stokes vector of unpolarized light* therefore is given by

$$\mathbf{S} = \begin{pmatrix} 1 \\ 0 \\ 0 \\ 0 \end{pmatrix} \quad (5.36)$$

For the representation of partially polarized light we decompose the optical field into unpolarized and polarized portions, which are mutually independent. The fraction of polarized light is described by the *degree of polarisation* P . Therefore the *normalized Stokes vector of partially polarized light* is given by

$$\begin{pmatrix} 1 \\ S_1 \\ S_2 \\ S_3 \end{pmatrix} = (1 - P) \begin{pmatrix} 1 \\ 0 \\ 0 \\ 0 \end{pmatrix} + P \begin{pmatrix} 1 \\ S'_1 \\ S'_2 \\ S'_3 \end{pmatrix} \quad (5.37)$$

where the second term represents completely polarized light ($\sqrt{S_1'^2 + S_2'^2 + S_3'^2} = 1$).

We also see

$$\sqrt{S_1^2 + S_2^2 + S_3^2} = P \leq 1 \quad (5.38)$$

Subsequently P describes the various polarization conditions. We get summarizingly

Completely polarized light:	$P = 1$
Partially polarized light:	$P < 1$
Unpolarized light:	$P = 0$

Similar to Jones matrix calculus, the change of the polarization state due to optical devices can be obtained by matrix multiplication. In this case a polarizing element is represented by a 4×4 Mueller matrix \mathbf{M} . Therefore, if \mathbf{S} denotes the Stokes vector of the incident beam, we obtain the state of polarization of the emerging beam \mathbf{S}' by

$$\mathbf{S}' = \mathbf{M}\mathbf{S} \quad (5.39)$$

$$\begin{pmatrix} S'_0 \\ S'_1 \\ S'_2 \\ S'_3 \end{pmatrix} = \begin{pmatrix} M_{00} & M_{01} & M_{02} & M_{03} \\ M_{10} & M_{11} & M_{12} & M_{13} \\ M_{20} & M_{21} & M_{22} & M_{23} \\ M_{30} & M_{31} & M_{32} & M_{33} \end{pmatrix} \begin{pmatrix} S_0 \\ S_1 \\ S_2 \\ S_3 \end{pmatrix}$$

In principle, to derive the Mueller matrix of an optical device, the Stokes parameters of the emerging beam are represented as a function of the Stokes parameters of the incident beam. Then the elements of the Mueller matrix are found by coefficient comparison. An example is given in the next chapter 5.3, where the Mueller matrix for reflection at an interface between two media is derived.

A graphical representation of the states of polarization is the so-called Poincaré sphere, see Fig. 5.3. The reference frame x, y, z corresponds in this precedence to linear horizontal, linear $+45^\circ$ and right circularly polarized light. As shown in chapter 5.1.2, each polarization state is characterized by the rotation Ψ and ellipticity χ of the polarization ellipse. Using these two angles in the way as depicted in Fig. 5.3, each state of polarization is unambiguously described by a point P located on the sphere. So for instance linear polarized light is represented by points on the equator and rcp and lcp by the north and south poles. Generally, all right handed states are found in the upper and left handed states in the lower hemisphere.

For completely polarized light the radius vector is of unit length, and from equation (5.29) we see that it's components correspond to the normalized Stokes parameters S_1 to S_3 . So the Poincaré sphere allows a convenient graphical representation of the Stokes formalism.

A further remarkable property of the Poincaré sphere is, that the change in state of polarization due to an optical device is described by a rotation of the sphere. More to this topic is found by Collins [13].

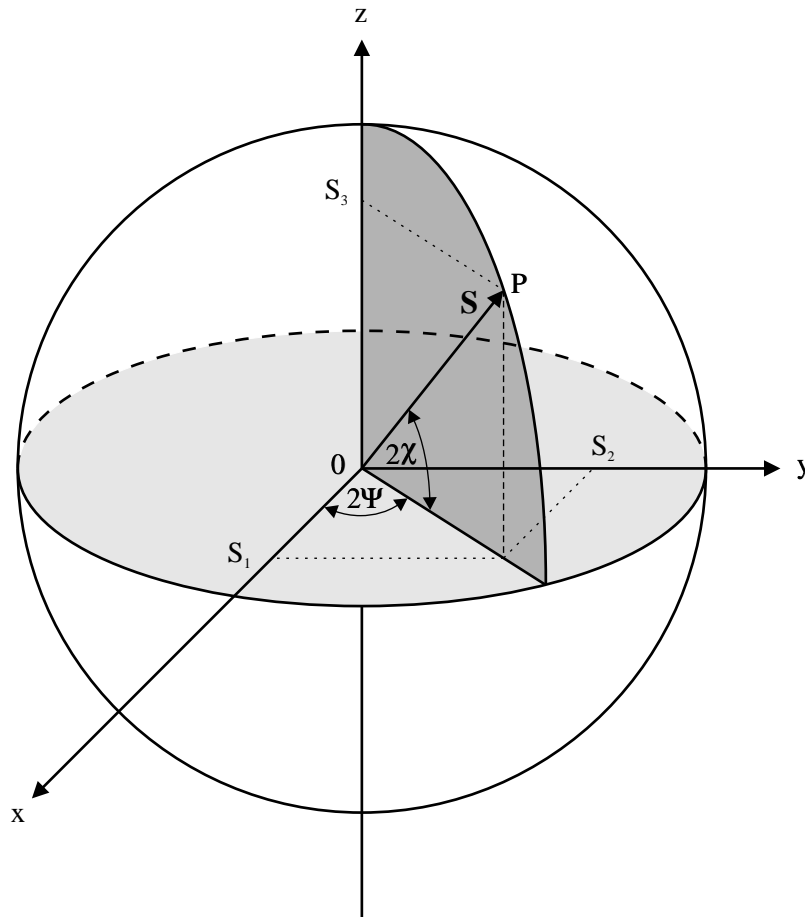


Figure 5.3: Representation of the state of polarization in the Poincaré sphere

$\mathbf{S} = (S_1 \ S_2 \ S_3)$: Stokes vector; Ψ, χ : angle of rotation and ellipticity of the polarization ellipse; x, y, z : reference frame of observer.

5.3 Mueller matrix for reflection

When light is reflected at an interface between two media, in general the state of polarization will change. This is described in the Stokes formalism by the Mueller matrix for reflection, which is derived in the following.

We assume the interface to be ideally smooth, so that there is only specular reflection. Fig. 5.4 shows the used coordinate system. The electric vector is decomposed in two components, one parallel (index p) and the other perpendicular (index s) to the plane of incidence. This is the plane which contains the incident beam as well as the reflected beam (drawing plane in Fig. 5.4).

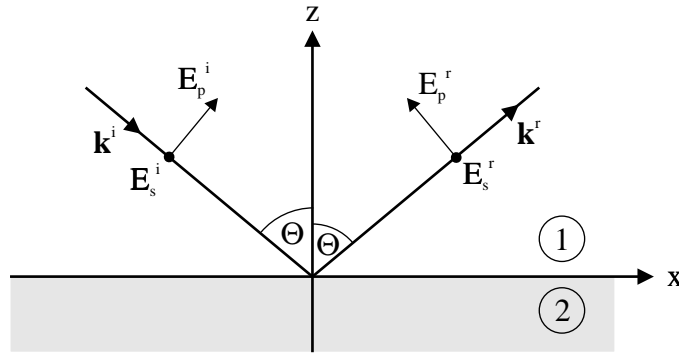


Figure 5.4: Reflection at an interface between two media 1 and 2
 \mathbf{k} : wave vector; E_p, E_s : components of electric vector parallel and perpendicular to the plane of incidence; i, r : indices for incident and reflected components; Θ : angle of incidence; x, y, z : reference frame of observer.

At the interface the electric and magnetic field obey certain boundary conditions. This is described by electrodynamics and the result is given by (see Papoušek [11])

$$\begin{aligned} E_p^r &= r_{12} E_p^i \\ E_s^r &= \overline{r_{12}} E_s^i \end{aligned} \quad (5.40)$$

E_p, E_s ... components of electric vector parallel and perpendicular to the plane of incidence
 i, r ... indices for incident and reflected components

where r_{12} and $\overline{r_{12}}$ are the Fresnel coefficients for reflection

$$\begin{aligned} r_{12} &= \frac{\epsilon_2 k_z^i - \epsilon_1 k_z^t}{\epsilon_2 k_z^i + \epsilon_1 k_z^t} \\ \overline{r_{12}} &= \frac{\mu_2 k_z^i - \mu_1 k_z^t}{\mu_2 k_z^i + \mu_1 k_z^t} \end{aligned} \quad (5.41)$$

ϵ ... complex electrical permittivity
 μ ... magnetic permeability
 k_z^i ... z -component wave vector of incident beam
 k_z^t ... z -component wave vector of transmitted beam

Generally, in ellipsometry the interface is seen to be vertically oriented. Therefore p -polarized means horizontal and s -polarized vertical linear polarized. With respect to the reference frame introduced in chapter 5.2, we obtain the relationship

$$\begin{aligned} E_x &= E_p \\ E_y &= E_s \end{aligned} \quad (5.42)$$

and using equation (5.28) we find for the incident beam

$$\mathbf{S}^i = \begin{pmatrix} S_0^i \\ S_1^i \\ S_2^i \\ S_3^i \end{pmatrix} = \frac{1}{2} \frac{c}{n} \varepsilon_0 \varepsilon \begin{pmatrix} E_p^i E_p^{i*} + E_s^i E_s^{i*} \\ E_p^i E_p^{i*} - E_s^i E_s^{i*} \\ E_p^i E_s^{i*} + E_s^i E_p^{i*} \\ i(E_p^i E_s^{i*} - E_s^i E_p^{i*}) \end{pmatrix} \quad (5.43)$$

The reflected beam is given by

$$\begin{aligned} \mathbf{S}^r &= \begin{pmatrix} S_0^r \\ S_1^r \\ S_2^r \\ S_3^r \end{pmatrix} = \frac{1}{2} \frac{c}{n} \varepsilon_0 \varepsilon \begin{pmatrix} E_p^r E_p^{r*} + E_s^r E_s^{r*} \\ E_p^r E_p^{r*} - E_s^r E_s^{r*} \\ E_p^r E_s^{r*} + E_s^r E_p^{r*} \\ i(E_p^r E_s^{r*} - E_s^r E_p^{r*}) \end{pmatrix} \\ &= \frac{1}{2} \frac{c}{n} \varepsilon_0 \varepsilon \begin{pmatrix} r_{12} r_{12}^* E_p^i E_p^{i*} + \overline{r_{12}} \overline{r_{12}^*} E_s^i E_s^{i*} \\ r_{12} r_{12}^* E_p^i E_p^{i*} - \overline{r_{12}} \overline{r_{12}^*} E_s^i E_s^{i*} \\ r_{12} \overline{r_{12}^*} E_p^i E_s^{i*} + \overline{r_{12}} r_{12}^* E_s^i E_p^{i*} \\ i(r_{12} \overline{r_{12}^*} E_p^i E_s^{i*} - \overline{r_{12}} r_{12}^* E_s^i E_p^{i*}) \end{pmatrix} \end{aligned} \quad (5.44)$$

This expression becomes simpler by representing the complex Fresnel coefficients in polar coordinates

$$\begin{aligned} r_{12} &=: \varrho_p e^{i\phi_p} \\ \overline{r_{12}} &=: \varrho_s e^{i\phi_s} \end{aligned} \quad (5.45)$$

$\varrho_p, \varrho_s \dots$ absolute values of complex fresnel coefficients

$\phi_p, \phi_s \dots$ phases of complex fresnel coefficients

and defining the phase difference Δ by

$$\Delta = \phi_p - \phi_s \quad (5.46)$$

In this way we come to

$$\mathbf{S}^r = \begin{pmatrix} S_0^r \\ S_1^r \\ S_2^r \\ S_3^r \end{pmatrix} = \frac{1}{2} \frac{c}{n} \varepsilon_0 \varepsilon \begin{pmatrix} \varrho_p^2 E_p^i E_p^{i*} + \varrho_s^2 E_s^i E_s^{i*} \\ \varrho_p^2 E_p^i E_p^{i*} - \varrho_s^2 E_s^i E_s^{i*} \\ \varrho_p \varrho_s e^{i\Delta} E_p^i E_s^{i*} + \varrho_p \varrho_s e^{-i\Delta} E_s^i E_p^{i*} \\ i(\varrho_p \varrho_s e^{i\Delta} E_p^i E_s^{i*} - \varrho_p \varrho_s e^{-i\Delta} E_s^i E_p^{i*}) \end{pmatrix} \quad (5.47)$$

The same result is obtained by matrix multiplication

$$\mathbf{S}^r = \mathbf{M}_{Reflection} \mathbf{S}^i \quad (5.48)$$

$$\begin{pmatrix} S_0^r \\ S_1^r \\ S_2^r \\ S_3^r \end{pmatrix} = \frac{1}{2} \begin{pmatrix} \varrho_p^2 + \varrho_s^2 & \varrho_p^2 - \varrho_s^2 & 0 & 0 \\ \varrho_p^2 - \varrho_s^2 & \varrho_p^2 + \varrho_s^2 & 0 & 0 \\ 0 & 0 & 2 \varrho_p \varrho_s \cos \Delta & 2 \varrho_p \varrho_s \sin \Delta \\ 0 & 0 & -2 \varrho_p \varrho_s \sin \Delta & 2 \varrho_p \varrho_s \cos \Delta \end{pmatrix} \begin{pmatrix} S_0^i \\ S_1^i \\ S_2^i \\ S_3^i \end{pmatrix}$$

So we have derived the Mueller matrix for reflection at an interface between two media.

In ellipsometry it is customary to use the so-called *ellipsometric parameters* ψ and Δ , where ψ is defined by

$$\frac{r_{12}}{r_{12}} = \frac{\varrho_p}{\varrho_s} e^{i\Delta} =: \tan \psi e^{i\Delta} \quad (5.49)$$

and Δ is already given by (5.46).

Extracting the term $(\varrho_p^2 + \varrho_s^2)$ from equation (5.48) and using the identities

$$\frac{1 - \tan^2 \psi}{1 + \tan^2 \psi} = \cos 2\psi \quad \frac{2 \tan \psi}{1 + \tan^2 \psi} = \sin 2\psi \quad (5.50)$$

we finally obtain the *Mueller matrix for reflection* in the form

$$\mathbf{M}_{Reflection} = \frac{\varrho_p^2 + \varrho_s^2}{2} \begin{pmatrix} 1 & -\cos 2\psi & 0 & 0 \\ -\cos 2\psi & 1 & 0 & 0 \\ 0 & 0 & \sin 2\psi \cos \Delta & \sin 2\psi \sin \Delta \\ 0 & 0 & -\sin 2\psi \sin \Delta & \sin 2\psi \cos \Delta \end{pmatrix} \quad (5.51)$$

5.4 Measurement of the ellipsometric parameters

The measurement of the ellipsometric parameters is done by applying $+45^\circ$ linear polarized light to the sample, and determining the state of polarization of the reflected light in form of a Stokes vector. In this case the calculation becomes rather simple as will be shown during this chapter.

The polarization state of the incident $+45^\circ$ linear polarized beam is represented by the Stokes vector \mathbf{S}^i

$$\mathbf{S}^i = \begin{pmatrix} 1 \\ 0 \\ 1 \\ 0 \end{pmatrix} \quad (5.52)$$

The state of the reflected beam \mathbf{S}^r is theoretically obtained by multiplication with the Mueller matrix of reflection (5.51)

$$\begin{aligned} \mathbf{S}^r &= \mathbf{M}_{Reflection} \mathbf{S}^i \\ &= \frac{\varrho_p^2 + \varrho_s^2}{2} \begin{pmatrix} 1 & -\cos 2\psi & 0 & 0 \\ -\cos 2\psi & 1 & 0 & 0 \\ 0 & 0 & \sin 2\psi \cos \Delta & \sin 2\psi \sin \Delta \\ 0 & 0 & -\sin 2\psi \sin \Delta & \sin 2\psi \cos \Delta \end{pmatrix} \begin{pmatrix} 1 \\ 0 \\ 1 \\ 0 \end{pmatrix} \\ \Rightarrow \begin{pmatrix} S_0^r \\ S_1^r \\ S_2^r \\ S_3^r \end{pmatrix} &= \frac{\varrho_p^2 + \varrho_s^2}{2} \begin{pmatrix} 1 \\ -\cos 2\psi \\ \sin 2\psi \cos \Delta \\ -\sin 2\psi \sin \Delta \end{pmatrix} \end{aligned} \quad (5.53)$$

On the other hand, when the Stokes vector of the reflected beam is measured, we can calculate the ellipsometric parameters from this equation. Additionally, when we form ratios between the different Stokes parameters, the leading factor $\frac{1}{2}(\varrho_p^2 + \varrho_s^2)$ will cancel out. So we come to the form

$$\tan \Delta = \frac{-S_3^r}{S_2^r} \quad (5.54)$$

$$\tan 2\psi = \frac{\sqrt{(S_2^r)^2 + (S_3^r)^2}}{-S_1^r} \quad (5.55)$$

5.5 The fundamental equation of ellipsometry

In the foregoing chapter we investigated how to obtain the ellipsometric parameters by measurement. Now we are interested in calculating the optical parameters from these quantities. The result will be given by the fundamental equation of ellipsometry.

Using the definition of the ellipsometric parameters (5.49) and also the Fresnel coefficients (5.41) we get

$$\begin{aligned} \rho := \tan \psi e^{i\Delta} &= \frac{r_{12}}{r_{12}} \\ &= \frac{(\epsilon_2 k_z^i - \epsilon_1 k_z^t)(\mu_2 k_z^i + \mu_1 k_z^t)}{(\epsilon_2 k_z^i + \epsilon_1 k_z^t)(\mu_2 k_z^i - \mu_1 k_z^t)} \end{aligned} \quad (5.56)$$

where ρ is a complex factor combining the ellipsometric parameters ψ and Δ .

Introducing the complex refractive index $\eta = \sqrt{\epsilon\mu}$ of the material (see equation (5.20)) we also can write the above expression in the form

$$\rho = \frac{\eta_2^2 (k_z^i)^2 - \eta_1^2 (k_z^t)^2 + k_z^i k_z^t \left(\frac{\mu_1}{\mu_2} \eta_2^2 - \frac{\mu_2}{\mu_1} \eta_1^2 \right)}{\eta_2^2 (k_z^i)^2 - \eta_1^2 (k_z^t)^2 - k_z^i k_z^t \left(\frac{\mu_1}{\mu_2} \eta_2^2 - \frac{\mu_2}{\mu_1} \eta_1^2 \right)} \quad (5.57)$$

Up to now there were no constraints to the media on both sides of the interface. For further analysis it is necessary to consider two points:

- Both materials are non-magnetic, therefore $\mu_1 = 1$ and $\mu_2 = 1$.
- Medium 1 is non-absorptive, therefore $\eta_1 = n_1$ and also k_1 are real numbers.

Because of the second point it is possible to introduce the angle of incidence, whereas for absorptive media phase, amplitude and energy don't have the same directions. So in this case it would not make sense to define an angle of refraction.

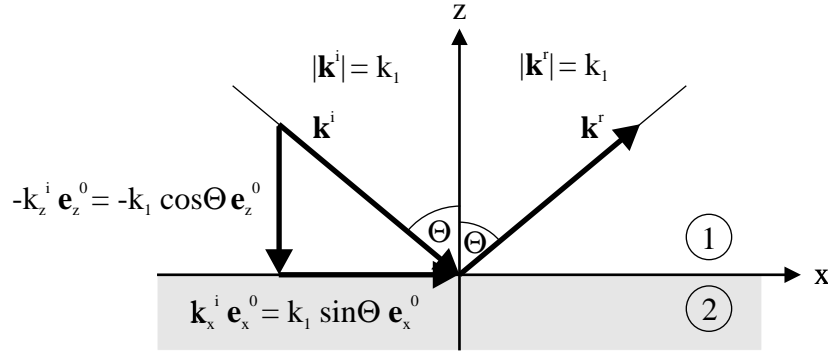


Figure 5.5: Components of the wave vector of the incident beam $\mathbf{k} = (k_x \ k_y \ k_z)$: wave vector; i, r : indices for incident and reflected components; Θ : angle of incidence; $\mathbf{e}_x^0, \mathbf{e}_z^0$: unit vector in x - and z -direction; x, y, z : reference frame of observer.

The components of the wave vector of the incident beam are shown in Fig. 5.5. The tangential part of k (the x -component) must be continuous at the interface and therefore the z -component of the wave vector of the transmitted beam is given by

$$k_z^t = -\sqrt{(k_2)^2 - (k_x^i)^2} = -\sqrt{(k_2)^2 - (k_1)^2 \sin^2 \Theta} \quad (5.58)$$

In this way and using equation (5.7)

$$k^2 = \omega^2 \varepsilon_0 \epsilon \mu_0 \mu = \omega^2 \varepsilon_0 \mu_0 \eta^2 \quad (5.59)$$

we are able to rewrite expression (5.57) after some rearrangements in the form

$$\rho = \frac{n_1 \sin^2 \Theta - \cos \Theta \sqrt{\eta_2^2 - n_1^2 \sin^2 \Theta}}{n_1 \sin^2 \Theta + \cos \Theta \sqrt{\eta_2^2 - n_1^2 \sin^2 \Theta}} \quad (5.60)$$

Solving for the complex refractive index η_2 we find

$$\eta_2 = n_2 - ik_2 = n_1 \sin \Theta \sqrt{1 + \tan^2 \Theta \left(\frac{1 - \rho}{1 + \rho} \right)^2} \quad (5.61)$$

or in an other form

$$\eta_2 = n_2 - ik_2 = n_1 \tan \Theta \sqrt{1 - \frac{4\rho \sin^2 \Theta}{(1 + \rho)^2}} \quad (5.62)$$

This expression is called the *fundamental equation of ellipsometry*. It allows the determination of the optical constants n_2 and k_2 of the material of interest.

In MATLAB there is the possibility to directly calculate the real and imaginary parts of η_2 to obtain the optical constants. If one uses an other program which doesn't support this feature, one needs to decompose the above equation in real and imaginary part. This is done by elementary but rather time-consuming operations. As an intermediary step we find

$$n_2^2 - k_2^2 = n_1^2 \sin^2 \Theta \left[1 + \tan^2 \Theta \frac{\cos^2 2\psi - \sin^2 2\psi \sin^2 \Delta}{(1 + \sin 2\psi \cos \Delta)^2} \right] \quad (5.63)$$

$$n_2 k_2 = n_1^2 \sin^2 \Theta \tan^2 \Theta \frac{\sin 2\psi \cos 2\psi \sin \Delta}{(1 + \sin 2\psi \cos \Delta)^2} \quad (5.64)$$

or in terms of Stokes parameters

$$n_2^2 - k_2^2 = n_1^2 \sin^2 \Theta \left[1 + \tan^2 \Theta \frac{(S_1^r)^2 - (S_3^r)^2}{(1 + S_2^r)^2} \right] \quad (5.65)$$

$$n_2 k_2 = n_1^2 \sin^2 \Theta \tan^2 \Theta \frac{S_1^r S_3^r}{(1 + S_2^r)^2} \quad (5.66)$$

When we use the abbreviations

$$n_2^2 - k_2^2 =: A \quad (5.67)$$

$$n_2 k_2 =: B \quad (5.68)$$

and after squaring the second expression and combining with the first one, we get quadratic equations. After solving these, we finally find for the optical constants

$$n_2^2 = \frac{A}{2} + \frac{\sqrt{A^2 + 4B^2}}{2} \quad (5.69)$$

$$k_2^2 = -\frac{A}{2} + \frac{\sqrt{A^2 + 4B^2}}{2} \quad (5.70)$$

5.6 Reflectance

With regard to the determination of emissivity from the optical constants we need the normal reflectance ρ_0 as depicted in chapter 5.

In general, the reflectance ρ is the fraction of incident flux reflected by a surface. Similarly, the transmittance τ is the fraction of incident flux which is transmitted through the interface between the two media. Because the flux is given by the product of intensity and cross sectional area of the beam, and in turn intensity is the absolute value of the time averaged Poynting vector, we can write (see Fig. 5.6)

$$\rho = \frac{|\langle \mathbf{S}^r \rangle| A \cos \Theta^r}{|\langle \mathbf{S}^i \rangle| A \cos \Theta^i} = \frac{\langle S_z^r \rangle}{\langle S_z^i \rangle} \quad (5.71)$$

$$\tau = \frac{|\langle \mathbf{S}^t \rangle| A \cos \Theta^t}{|\langle \mathbf{S}^i \rangle| A \cos \Theta^i} = \frac{\langle S_z^t \rangle}{\langle S_z^i \rangle} \quad (5.72)$$

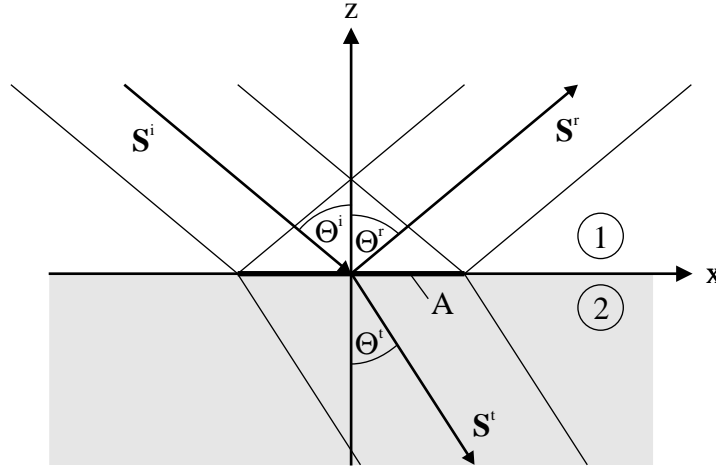


Figure 5.6: To the definition of reflectance and transmittance
A: radiated area at interface; \mathbf{S}^i , \mathbf{S}^r , \mathbf{S}^t : Poynting vector of incident, reflected and transmitted beam; Θ^i , Θ^r , Θ^t : incidence, reflection and transmittance angle; x, z : reference frame of observer.

From equation (5.19) we can see that the absolute value of the Poynting vector (= intensity) is proportional to the square of the amplitude of the electric vector. If we only consider p-polarized light, the reflectance ρ_p is given by

$$\rho_p = \frac{\langle S_{zp}^r \rangle}{\langle S_{zp}^i \rangle} = \frac{|\langle \mathbf{S}_p^r \rangle|}{|\langle \mathbf{S}_p^i \rangle|} = \frac{(E_{0p}^r)^2}{(E_{0p}^i)^2} = |r_{12}|^2 = \varrho_p^2 \quad (5.73)$$

where the second equality holds because of $\Theta^i = \Theta^r$. To avoid misunderstandings, it should be noted that the coordinate system in the case of reflection is drawn with respect to the interface (see Fig. 5.6), whereas the reference frame used in equation (5.19) is oriented with the z-axes parallel to the direction of propagation of the plane wave.

Using the definitions made in the foregoing chapter we obtain

$$\begin{aligned}\rho_p &= \left| \frac{\epsilon_2 k_z^i - \epsilon_1 k_z^t}{\epsilon_2 k_z^i + \epsilon_1 k_z^t} \right|^2 \\ &= \left| \frac{\eta_2^2 \cos \Theta - n_1 \sqrt{\eta_2^2 - n_1^2 \sin^2 \Theta}}{\eta_2^2 \cos \Theta + n_1 \sqrt{\eta_2^2 - n_1^2 \sin^2 \Theta}} \right|^2\end{aligned}\quad (5.74)$$

and similar for s-polarized light

$$\rho_s = \frac{\langle S_{zs}^r \rangle}{\langle S_{zs}^i \rangle} = \frac{|\langle \mathbf{S}_s^r \rangle|}{|\langle \mathbf{S}_s^i \rangle|} = \frac{(E_{0s}^r)^2}{(E_{0s}^i)^2} = |\overline{r_{12}}|^2 = \varrho_s^2 \quad (5.75)$$

$$\begin{aligned}\rho_s &= \left| \frac{\mu_2 k_z^i - \mu_1 k_z^t}{\mu_2 k_z^i + \mu_1 k_z^t} \right|^2 \\ &= \left| \frac{n_1 \cos \Theta - \sqrt{\eta_2^2 - n_1^2 \sin^2 \Theta}}{n_1 \cos \Theta + \sqrt{\eta_2^2 - n_1^2 \sin^2 \Theta}} \right|^2\end{aligned}\quad (5.76)$$

The equations become simpler, when we confine ourself to normal incidence $\Theta = 0$. In this case the reflectance for p- and s-polarized light become equal and we write $\rho(0)$ instead of $\rho_p(\Theta = 0)$ and $\rho_s(\Theta = 0)$. So we obtain

$$\rho(0) = \left| \frac{\eta_2 - n_1}{\eta_2 + n_1} \right|^2 \quad (5.77)$$

or using the optical constants n_2 and k_2

$$\rho(0) = \frac{(n_1 - n_2)^2 + k_2^2}{(n_1 + n_2)^2 + k_2^2} \quad (5.78)$$

So we have derived the normal reflectance $\rho(0)$, which connects the optical constants with emissivity ϵ , as described in chapter 5, equation (5.5).

5.7 Simulation of the reflective behavior

Additional to *HOTWIRE* some small programs were developed concerning the simulation of reflective behavior and emissivity.

- *SIMREFLECTION*: Simulation of the reflective behavior

As shown in the last chapter the reflectance ρ_p and ρ_s for p- and s-polarized light (equations (5.74) and (5.76)) are given by the optical parameters of the material at which the light is reflected, and of the ambient. In most applications this is air or vacuum and so we have $n_1 = 1$. The program *SIMREFLECTION* computes ρ_p and ρ_s as a function of incident angle. The results are shown in Fig. 5.7 for BK7-glass, which is practically non-absorptive, and in Fig. 5.8 for an absorptive medium.

The ellipsometric parameters ψ and Δ can be obtained using equations (5.56) and (5.60) where $\tan \psi$ is the absolute value of the complex factor ρ and Δ its phase. The results are represented in Fig. 5.9 and Fig. 5.10, in turn for BK7-glass and an absorptive medium.

In the experiment $+45^\circ$ -polarized light is reflected at an interface and the Stokes parameters of the emerging beam are measured. On the other hand the Stokes parameters can be simulated from expression (5.53). The so obtained results are shown in Fig. 5.11 and Fig. 5.12.

- *BREWSTER*: Pseudo-brewster angle of absorptive media

For non-absorptive media the reflectance ρ_p of p-polarized light becomes zero at the so-called *Brewster angle* Θ_B , see Fig. 5.7. This angle is related to the refractive indices by

$$\tan \Theta_B = \frac{n_2}{n_1} \quad (5.79)$$

As shown in Fig. 5.8 for absorptive media, ρ_p only has on a minimum at the now so-called *pseudo-Brewster angle*, and there is no simple expression like (5.79). The small program *BREWSTER* evaluates the pseudo-Brewster angles as a function of refractive index n_2 and the extinction coefficient k_2 as parameter. The results are shown in Fig. 5.13 and Fig. 5.14.

In appendix A, table A.2, the optical parameters of some selected metals at room temperature are given, and also the calculated pseudo-Brewster angles. One can see that the values ranges from about 70° to 80° .

- *EMISSIVITY*: Parameter curves for constant emissivity

A given emissivity can be achieved by different values of refractive index n_2 and extinction coefficient k_2 . This can be seen by solving expression (5.5) for k_2

$$k_2^2 = \frac{4 n_1 n_2}{\epsilon} - (n_1 + n_2)^2 \quad (5.80)$$

The small program *EMISSIVITY* computes k_2 as a function of n_2 for different emissivity values as parameter. The result is represented in Fig. 5.15 and more detailed for small n_2 -values in Fig. 5.16.

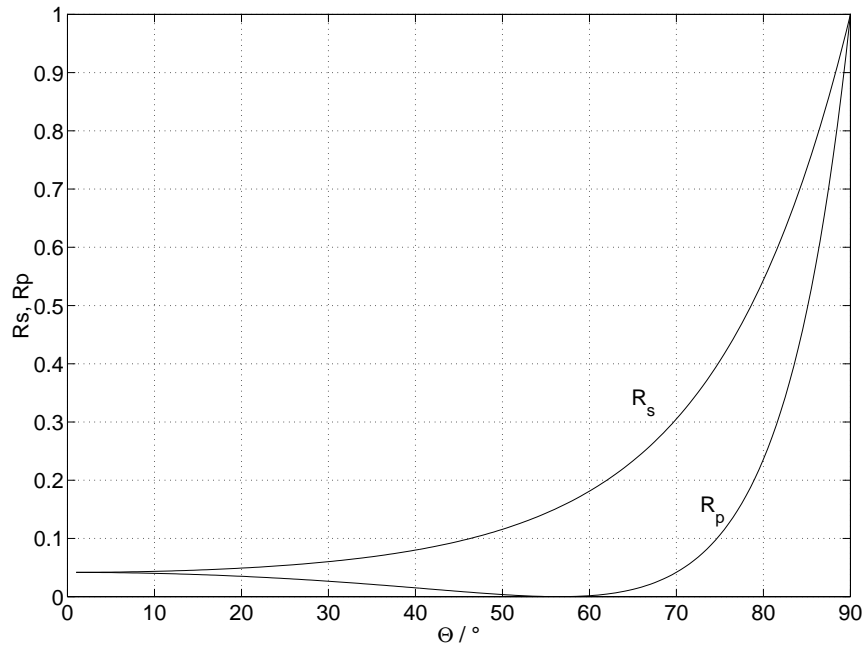


Figure 5.7: Simulation of the reflective behavior of a non-absorptive material (BK7-glass, $n = 1.5135$ and $k = 0$ at $\lambda = 684.4 \text{ nm}$)
 R_s, R_p : reflectance for s- and p-polarized light; λ : wavelength;
 Θ : angle of incidence.

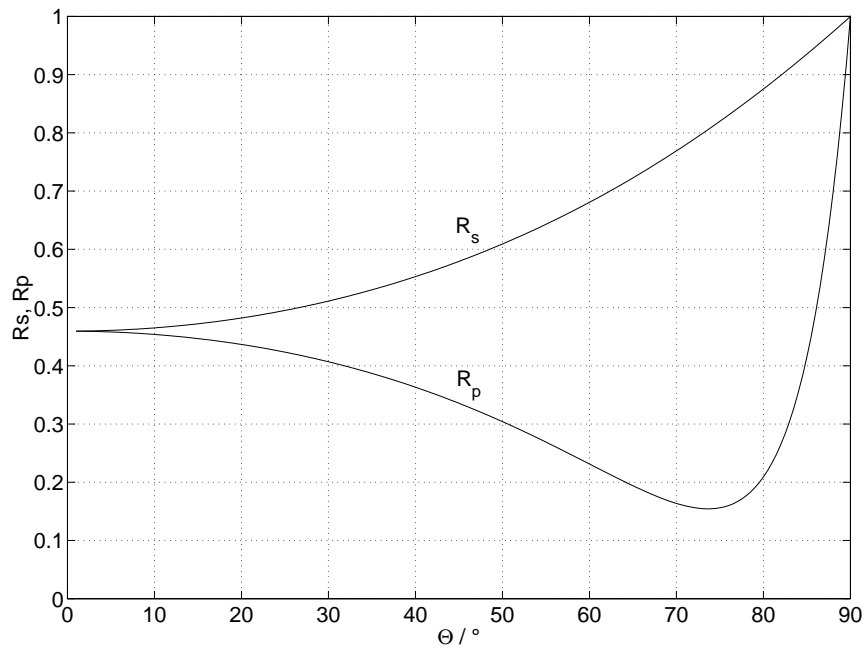


Figure 5.8: Simulation of the reflective behavior of an absorptive material ($n = 2.5$ and $k = 2.5$)
 R_s, R_p : reflectance for s- and p-polarized light; Θ : angle of incidence.

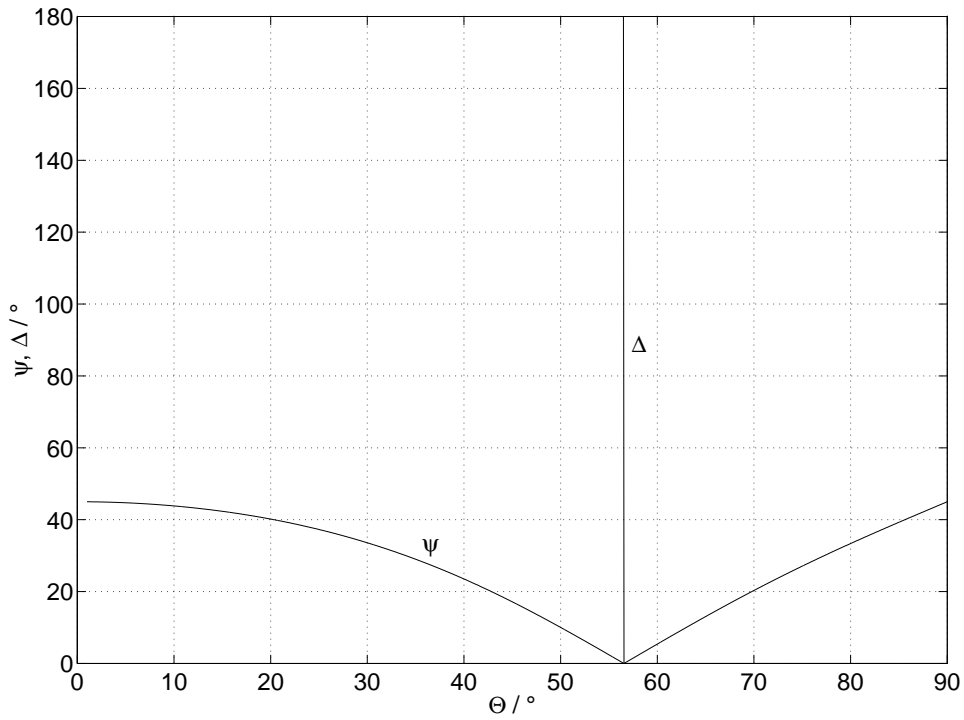


Figure 5.9: Simulation of the ellipsometric parameters for BK7-glass ($n = 1.5135$ and $k = 0$ at $\lambda = 684.4 \text{ nm}$); Parameter Δ is a step function from 180° to 0° ; S_1, S_2, S_3 : Stokes parameters; Θ : angle of incidence.

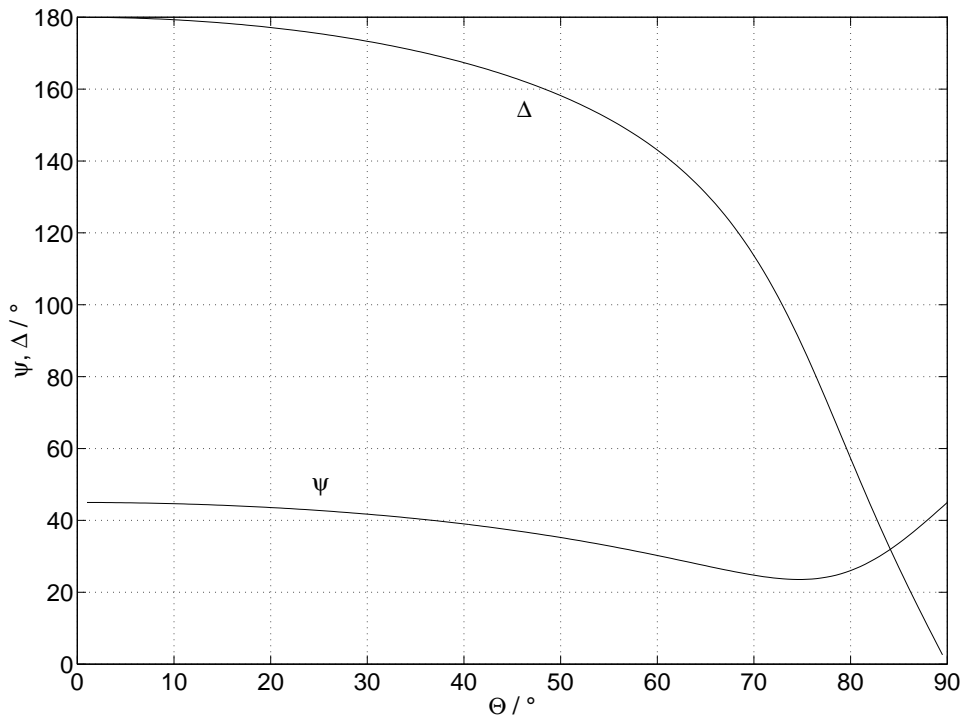


Figure 5.10: Simulation of the ellipsometric parameters for an absorptive medium ($n = 2.5$ and $k = 2.5$); S_1, S_2, S_3 : Stokes parameters; Θ : angle of incidence.

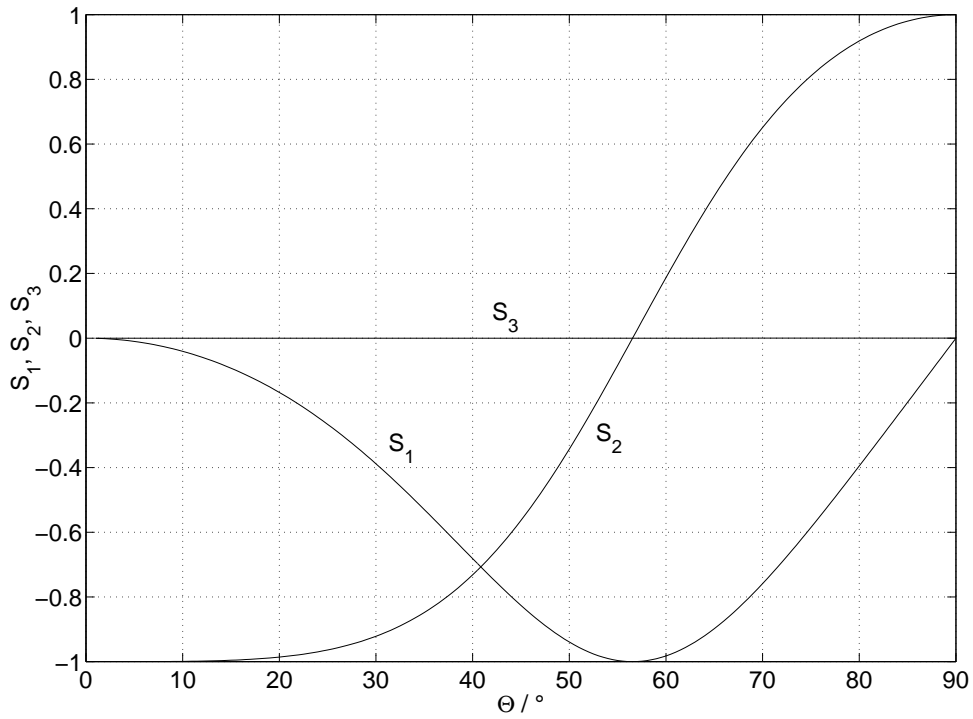


Figure 5.11: Simulation of the Stokes parameters for BK7-glass ($n = 1.5135$ and $k = 0$ at $\lambda = 684.4 \text{ nm}$)
 ψ, Δ : ellipsometric parameters; λ : wavelength; Θ : angle of incidence.

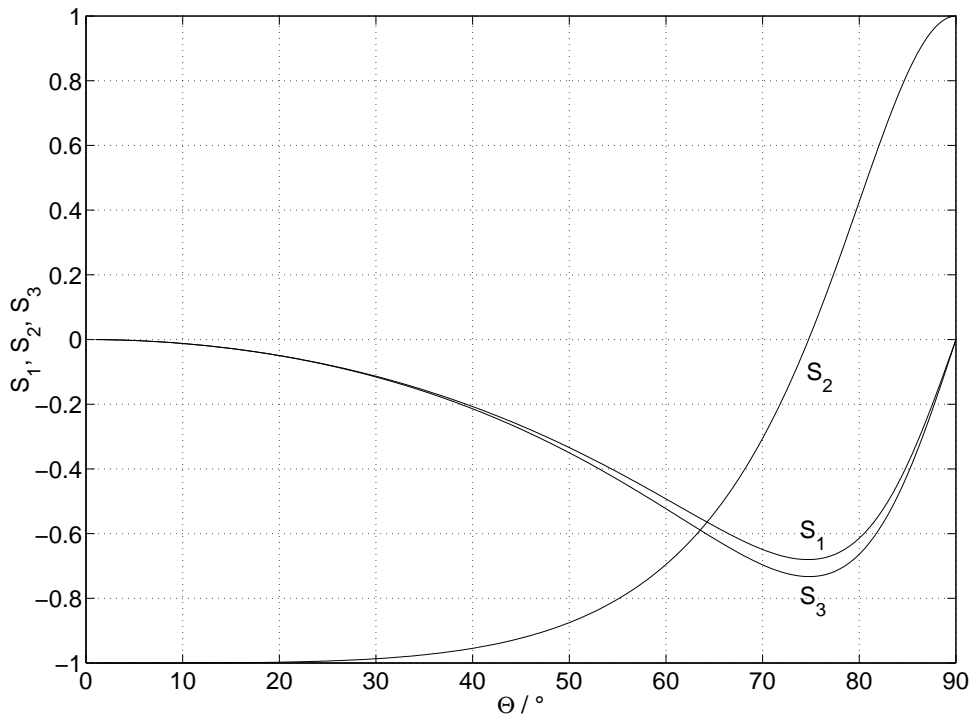


Figure 5.12: Simulation of the Stokes parameters for an absorptive medium ($n = 2.5$ and $k = 2.5$)
 ψ, Δ : ellipsometric parameters; Θ : angle of incidence.

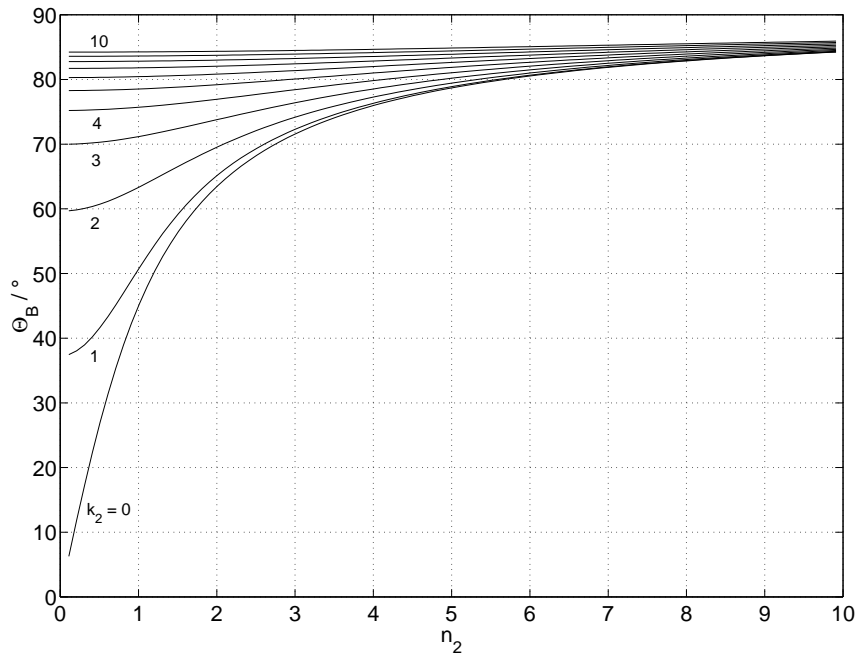


Figure 5.13: Pseudo-Brewster angle as a function of optical parameters
 Θ_B : pseudo-Brewster angle; n_2 : refractive index; k_2 : extinction coefficient.

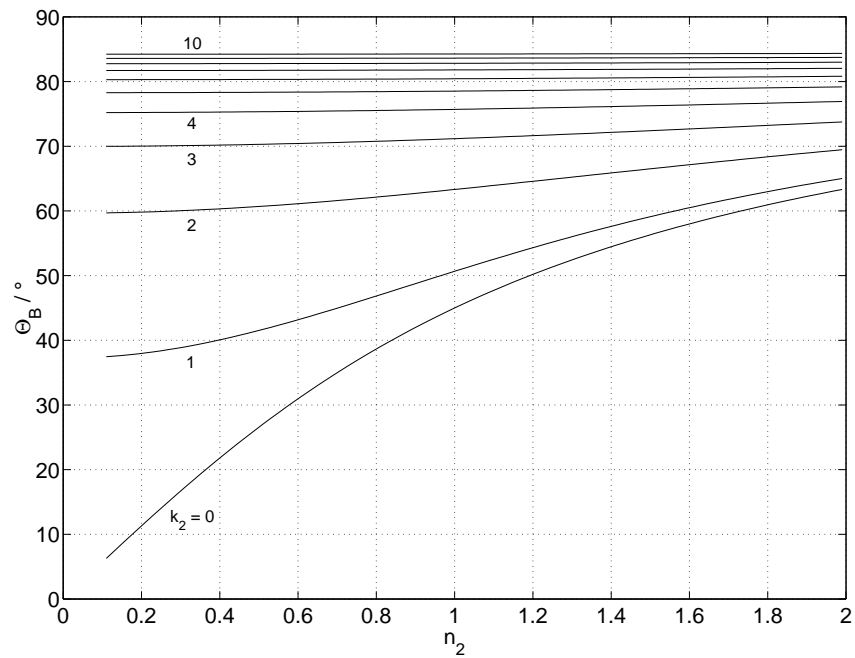


Figure 5.14: Pseudo-Brewster angle as a function of optical parameters
 Θ_B : pseudo-Brewster angle; n_2 : refractive index; k_2 : extinction coefficient.

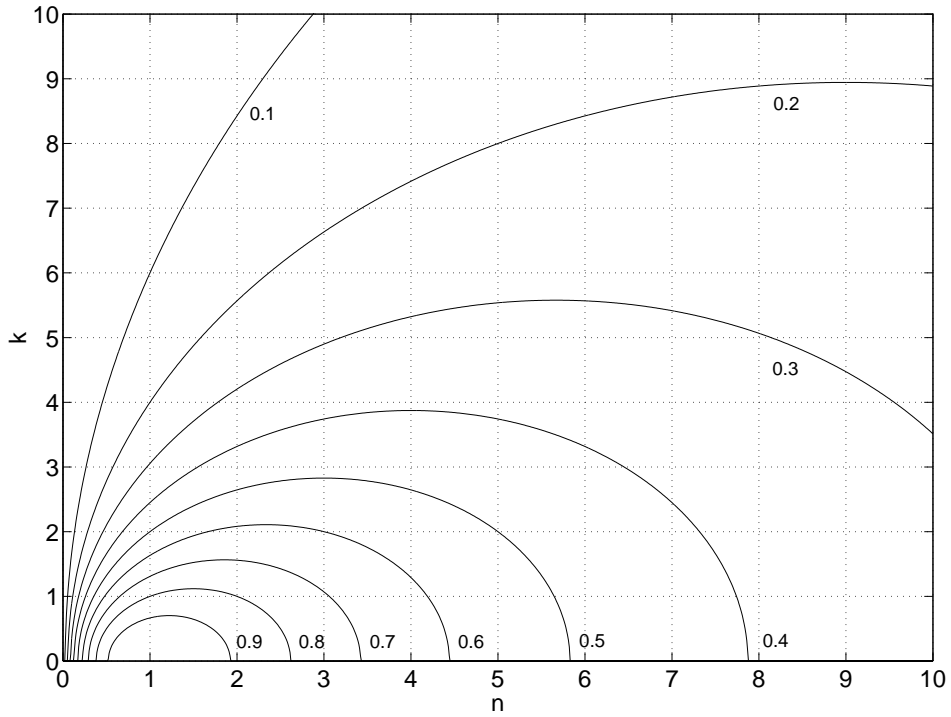


Figure 5.15: Parameter curves of constant normal emissivity
 n : refractive index; k : extinction coefficient.

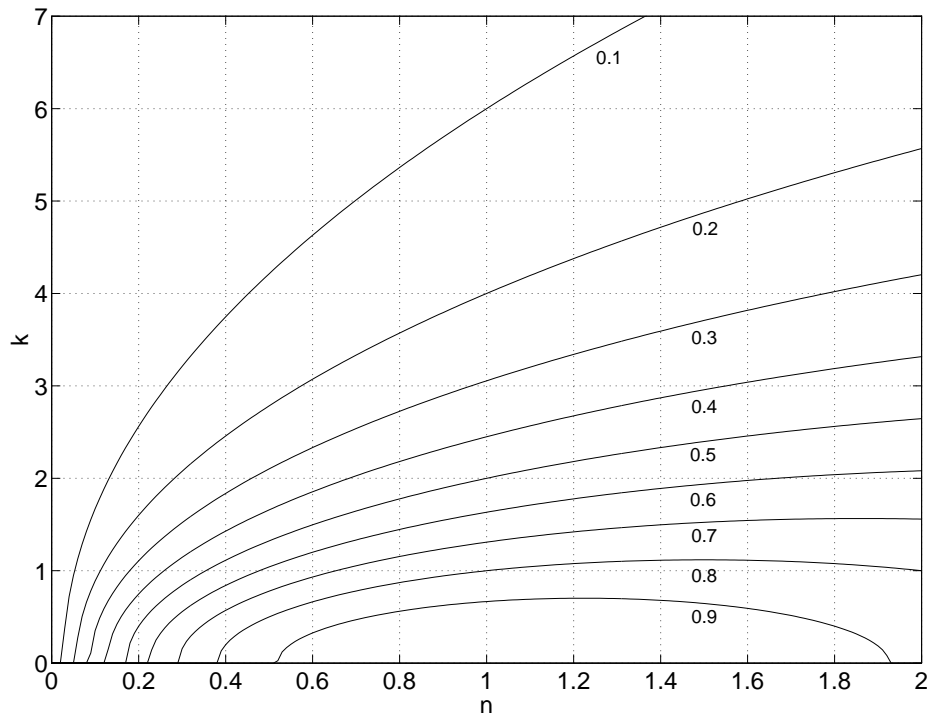


Figure 5.16: Parameter curves of constant normal emissivity
 n : refractive index; k : extinction coefficient.

5.8 Polarizing elements and generation of arbitrary polarized states

This chapter provides a list of Mueller matrices of the most important optical elements used in ellipsometry. Finally these are used to describe an arrangement of a linear polarizer and a quarter-wave retarder to generate arbitrary polarized states.

The reference frame is chosen as shown in Fig. 5.17 where the x -axis corresponds to linear horizontal polarized light. The polarization state of the incident beam is represented by the Stokes vector \mathbf{S} and the state of the emerging beam by \mathbf{S}' . The change of polarization is described by the appropriate Mueller matrix in the way of equation (5.39)

$$\mathbf{S}' = \mathbf{M}\mathbf{S} \quad (5.81)$$

When the polarizing element is rotated with its characteristic axes x'_p and y'_p through an angle θ (see Fig. 5.17), the Mueller matrix \mathbf{M}_{rot} of the rotated element is obtained by

$$\mathbf{M}_{rot} = \mathbf{M}_R(-2\theta)\mathbf{M}\mathbf{M}_R(2\theta) \quad (5.82)$$

where \mathbf{M} means the Mueller matrix of the non-rotated element. $\mathbf{M}_R(2\theta)$ is the Mueller matrix for rotation, which is given by

$$\mathbf{M}_R(2\theta) = \begin{pmatrix} 1 & 0 & 0 & 0 \\ 0 & \cos 2\theta & \sin 2\theta & 0 \\ 0 & -\sin 2\theta & \cos 2\theta & 0 \\ 0 & 0 & 0 & 1 \end{pmatrix} \quad (5.83)$$

This matrix corresponds to passive coordinate transformation. The argument 2θ shows that the rotation is influenced twice by the angle of rotation θ . This is due to the fact that the Stokes formalism deals with intensities and not with amplitudes.

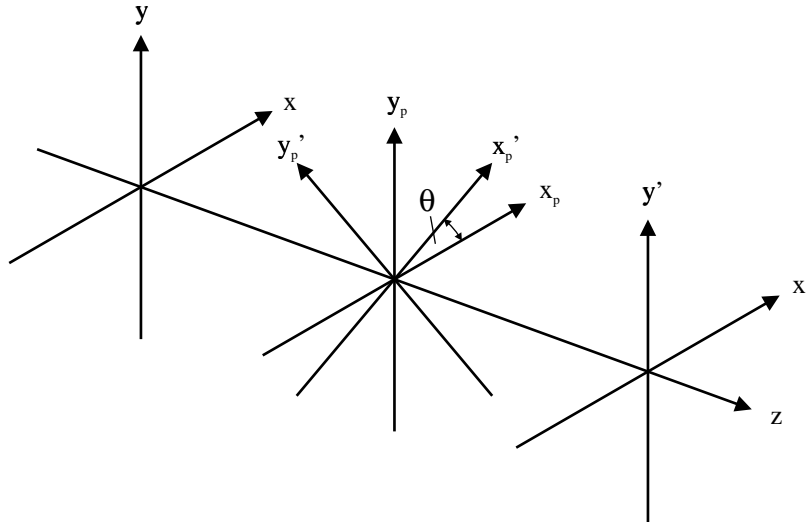


Figure 5.17: Reference frames to describe the polarizing behavior of optical elements

x, y : reference frame of incident beam; x_p, y_p : polarizing element; x'_p, y'_p : rotated polarizing element; x', y' : emerging beam; θ : angle of rotation; z : direction of propagation.

- Neutral density filter

The neutral density filter doesn't change the state of polarization, but the intensity of the incident beam is reduced by a factor p . So the Mueller matrix is proportional to the unit matrix and is given by

$$\mathbf{M}_{NDF} = p \begin{pmatrix} 1 & 0 & 0 & 0 \\ 0 & 1 & 0 & 0 \\ 0 & 0 & 1 & 0 \\ 0 & 0 & 0 & 1 \end{pmatrix} \quad (5.84)$$

- Linear polarizer

The Mueller matrix of a linear polarizer with its transmission axes parallel to x (a linear horizontal polarizer) is given by

$$\mathbf{M}_{LHP} = \frac{1}{2} \begin{pmatrix} 1 & 1 & 0 & 0 \\ 1 & 1 & 0 & 0 \\ 0 & 0 & 0 & 0 \\ 0 & 0 & 0 & 0 \end{pmatrix} \quad (5.85)$$

which can easily be seen by applying to unpolarized light

$$\frac{1}{2} \begin{pmatrix} 1 & 1 & 0 & 0 \\ 1 & 1 & 0 & 0 \\ 0 & 0 & 0 & 0 \\ 0 & 0 & 0 & 0 \end{pmatrix} \begin{pmatrix} 1 \\ 0 \\ 0 \\ 0 \end{pmatrix} = \frac{1}{2} \begin{pmatrix} 1 \\ 1 \\ 0 \\ 0 \end{pmatrix} \quad (5.86)$$

Note, that the intensity behind the polarizer is half the incident intensity.

For a linear horizontal polarizer, which is rotated with its transmission axes through an angle θ , we apply equation (5.82) and find

$$\mathbf{M}_{LP}(2\theta) = \frac{1}{2} \begin{pmatrix} 1 & \cos 2\theta & \sin 2\theta & 0 \\ \cos 2\theta & \cos^2 2\theta & \sin 2\theta \cos 2\theta & 0 \\ \sin 2\theta & \sin 2\theta \cos 2\theta & \sin^2 2\theta & 0 \\ 0 & 0 & 0 & 0 \end{pmatrix} \quad (5.87)$$

From this it is easy to obtain some special cases:

- Linear vertical polarizer

$$\mathbf{M}_{LVP} = \frac{1}{2} \begin{pmatrix} 1 & -1 & 0 & 0 \\ -1 & 1 & 0 & 0 \\ 0 & 0 & 0 & 0 \\ 0 & 0 & 0 & 0 \end{pmatrix} \quad (5.88)$$

- Linear $\pm 45^\circ$ polarizer

$$\mathbf{M}_{\pm 45LP} = \frac{1}{2} \begin{pmatrix} 1 & 0 & \pm 1 & 0 \\ 0 & 0 & 0 & 0 \\ \pm 1 & 0 & 1 & 0 \\ 0 & 0 & 0 & 0 \end{pmatrix} \quad (5.89)$$

where (+) is for the $+45^\circ$ and (–) for -45° polarizer.

- Retarder

A retarder is a polarizing element, which introduces a phase shift ϕ between the orthogonal components of the incident beam. When the fast axes of the retarder is along the x -axes, this is accomplished by causing a phase shift of $-\phi/2$ along the x -axes and a phase shift of $+\phi/2$ along the y -axes. The Mueller matrix \mathbf{M}_C of a retarder ¹ with it's fast axes along the x -axes is given by

$$\mathbf{M}_C = \begin{pmatrix} 1 & 0 & 0 & 0 \\ 0 & 1 & 0 & 0 \\ 0 & 0 & \cos \phi & \sin \phi \\ 0 & 0 & -\sin \phi & \cos \phi \end{pmatrix} \quad (5.90)$$

For the rotated retarder we find from equation (5.82)

$$\mathbf{M}_C(2\theta) = \begin{pmatrix} 1 & 0 & 0 & 0 \\ 0 & \cos^2 2\theta + \cos \phi \sin^2 2\theta & (1 - \cos \phi) \sin 2\theta \cos 2\theta & -\sin \phi \sin 2\theta \\ 0 & (1 - \cos \phi) \sin 2\theta \cos 2\theta & \sin^2 2\theta + \cos \phi \cos^2 2\theta & \sin \phi \cos 2\theta \\ 0 & \sin \phi \sin 2\theta & -\sin \phi \cos 2\theta & \cos \phi \end{pmatrix} \quad (5.91)$$

From this it is easy to obtain some special cases:

- Quarter-wave retarder

It is also called a $\lambda/4$ -plate. The phase shift ϕ is 90° and we find

$$\mathbf{M}_{\lambda/4}(2\theta) = \begin{pmatrix} 1 & 0 & 0 & 0 \\ 0 & \cos^2 2\theta & \sin 2\theta \cos 2\theta & -\sin 2\theta \\ 0 & \sin 2\theta \cos 2\theta & \sin^2 2\theta & \cos 2\theta \\ 0 & \sin 2\theta & -\cos 2\theta & 0 \end{pmatrix} \quad (5.92)$$

and for a quarter-wave plate with it's fast axes along the x -direction

$$\mathbf{M}_{\lambda/4} = \begin{pmatrix} 1 & 0 & 0 & 0 \\ 0 & 1 & 0 & 0 \\ 0 & 0 & 0 & 1 \\ 0 & 0 & -1 & 0 \end{pmatrix} \quad (5.93)$$

Applying linear $+45^\circ$ polarized light to the last case we have

$$\begin{pmatrix} 1 & 0 & 0 & 0 \\ 0 & 1 & 0 & 0 \\ 0 & 0 & 0 & 1 \\ 0 & 0 & -1 & 0 \end{pmatrix} \begin{pmatrix} 1 \\ 0 \\ 1 \\ 0 \end{pmatrix} = \begin{pmatrix} 1 \\ 0 \\ 0 \\ -1 \end{pmatrix} \quad (5.94)$$

So the result is left circularly polarized light.

¹In standard ellipsometry the quarter-wave plate is used as a compensator, therefore the index C

– Half-wave plate

It is also called a $\lambda/2$ -plate. The phase shift ϕ is 180° and we find

$$\mathbf{M}_{\lambda/2}(4\theta) = \begin{pmatrix} 1 & 0 & 0 & 0 \\ 0 & \cos 4\theta & \sin 4\theta & 0 \\ 0 & \sin 4\theta & -\cos 4\theta & 0 \\ 0 & 0 & 0 & -1 \end{pmatrix} \quad (5.95)$$

and for a half-wave plate with its fast axes along the x -direction

$$\mathbf{M}_{\lambda/2} = \begin{pmatrix} 1 & 0 & 0 & 0 \\ 0 & 1 & 0 & 0 \\ 0 & 0 & -1 & 0 \\ 0 & 0 & 0 & -1 \end{pmatrix} \quad (5.96)$$

For a detailed derivation of the here introduced equations see e.g. Collins [13].

Generation of arbitrary polarized states

To obtain arbitrary polarized states we use a linear polarizer followed by a quarter-wave plate as shown in Fig. 5.18. The incident beam is unpolarized and therefore the Stokes vector \mathbf{S}^P after the polarizer is represented by

$$\mathbf{M}_{LHP}(2\theta_P) \mathbf{S}^i = \mathbf{S}^P$$

$$\frac{1}{2} \begin{pmatrix} 1 & \cos 2P & \sin 2P & 0 \\ \cos 2P & \cos^2 2P & \sin 2P \cos 2P & 0 \\ \sin 2P & \sin 2P \cos 2P & \sin^2 2P & 0 \\ 0 & 0 & 0 & 0 \end{pmatrix} \begin{pmatrix} 1 \\ 0 \\ 0 \\ 0 \end{pmatrix} = \frac{1}{2} \begin{pmatrix} 1 \\ \cos 2P \\ \sin 2P \\ 0 \end{pmatrix} \quad (5.97)$$

where we write P and C instead of θ_P and θ_C for the sake of simplicity. After passing the retarder the state of polarization becomes finally

$$\mathbf{M}_{\lambda/4}(2\theta_C) \mathbf{S}^P = \mathbf{S}'$$

$$\begin{pmatrix} 1 & 0 & 0 & 0 \\ 0 & \cos^2 2C & \sin 2C \cos 2C & -\sin 2C \\ 0 & \sin 2C \cos 2C & \sin^2 2C & \cos 2C \\ 0 & \sin 2C & -\cos 2C & 0 \end{pmatrix} \frac{1}{2} \begin{pmatrix} 1 \\ \cos 2P \\ \sin 2P \\ 0 \end{pmatrix} =$$

$$= \frac{1}{2} \begin{pmatrix} 1 \\ \cos(2C - 2P) \cos 2C \\ \cos(2C - 2P) \sin 2C \\ \sin(2C - 2P) \end{pmatrix} = \frac{1}{2} \begin{pmatrix} 1 \\ 1/2 \cos 2P + 1/2 \cos(4C - 2P) \\ 1/2 \sin 2P + 1/2 \sin(4C - 2P) \\ \sin(2C - 2P) \end{pmatrix} \quad (5.98)$$

Subsequently any polarized state can be achieved by rotating polarizer and quarter-wave plate independent from each other. The factor $1/2$ doesn't influence the state of polarization and is mostly suppressed.

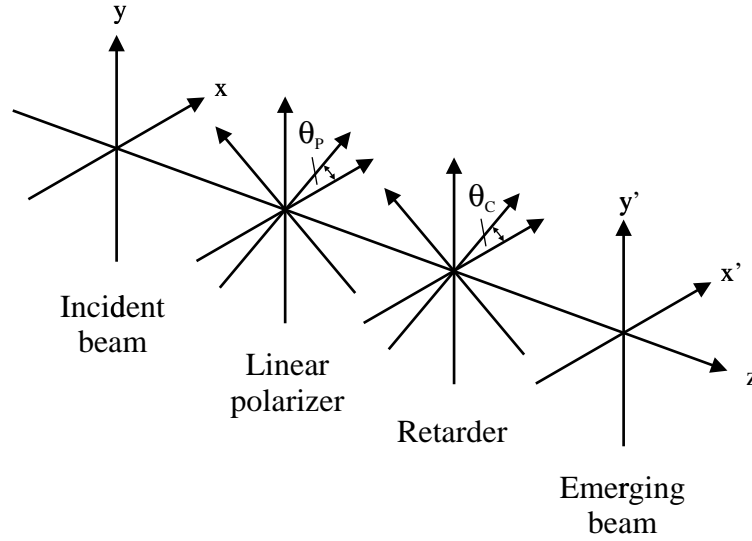


Figure 5.18: Generation of arbitrary states of polarization using a linear polarizer and a quarter-wave retarder
 x, y : reference frame of incident beam; x', y' : emerging beam;
 θ_P : angle of rotation of the linear polarizer; θ_C : angle of rotation of the quarter-wave retarder; z : direction of propagation.

The polarization state generator (PSD) of the DOAP system is exactly the arrangement from Fig. 5.18. For the calibration and verification procedures we have to generate three special cases of polarized light (see chapter 6):

- Linear polarized states

Rotating polarizer and retarder through the same angle ($\theta_P = \theta_C$), or using the polarizer without quarter-wave plate, we obtain linear polarized states only. When the incident light is unpolarized, the Stokes vector of the emerging beam is given by equation (5.97)

$$\mathbf{S}' = \begin{pmatrix} 1 \\ \cos 2P \\ \sin 2P \\ 0 \end{pmatrix} \quad (5.99)$$

The Stokes parameter S_1 and S_2 are sinusoidal functions of the angle of rotation θ_P . This is graphically represented in Fig. 5.19.

- Circularly polarized states

When polarizer and retarder are rotated through $\pm 45^\circ$ to each other, it follows $2C - 2P = \pm 90^\circ$. Consequently we find using expression (5.98)

$$\mathbf{S}' = \begin{pmatrix} 1 \\ 0 \\ 0 \\ \pm 1 \end{pmatrix} \quad (5.100)$$

In this case we have generated circularly polarized light.

- Elliptically polarized states

For the verification procedure the linear polarizer is set to $\theta_P = 0$, and only the retarder is rotated. Therefore we find from equation (5.98)

$$\mathbf{S}' = \begin{pmatrix} 1 \\ \cos^2 2C \\ \cos 2C \sin 2C \\ \sin 2C \end{pmatrix} = \begin{pmatrix} 1 \\ 1/2 (1 + \cos 4C) \\ 1/2 \sin 4C \\ \sin 2C \end{pmatrix} \quad (5.101)$$

This is graphically represented in Fig. 5.20.

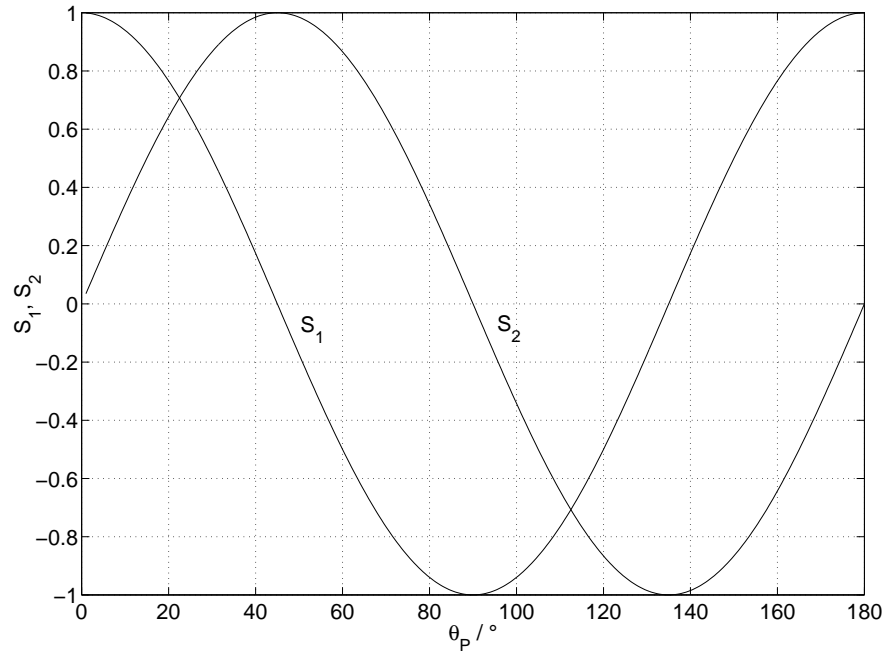


Figure 5.19: Simulation of the generation of linear polarized states S_1, S_2 : Stokes parameters of polarized light; θ_P : angle of rotation of the polarizer.

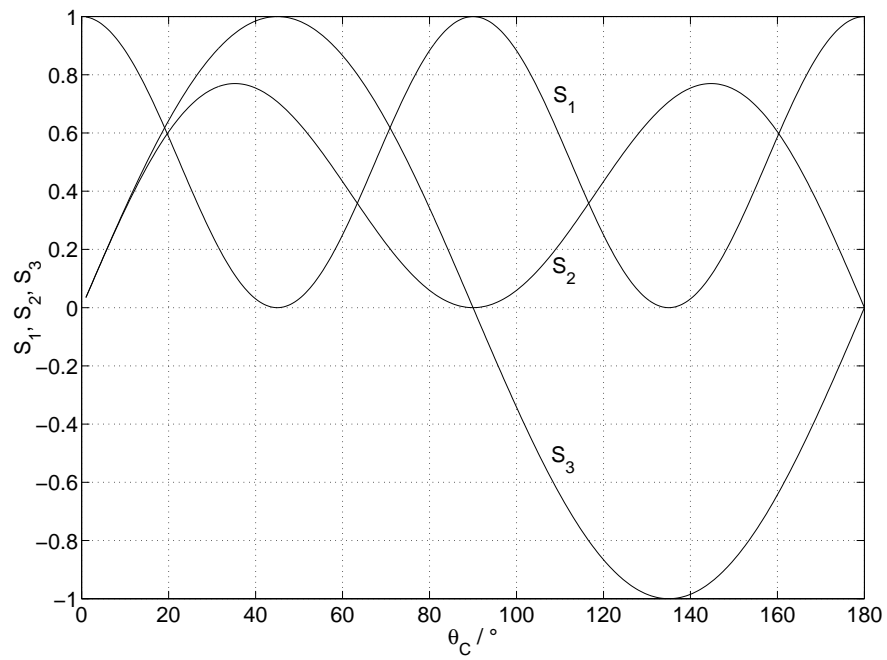


Figure 5.20: Simulation of the generation of elliptically polarized states
 S_1, S_2, S_3 : Stokes parameters of polarized light; θ_C : angle of rotation of the quarter-wave retarder.

Chapter 6

Division-of-amplitude photopolarimeter (DOAP)

6.1 The principle of the DOAP

The division-of-amplitude photopolarimeter is an ellipsometer without any mechanically rotated components. It is predestined for high-speed ellipsometry and therefore most eligible for the application to pulse heating experiments.

The DOAP consists of two major parts, the polarization state generator (PSG) and the polarization state detector (PSD). In chapter 6.2 setup and mode of operation of these two components are thoroughly described. They are arranged as shown in Fig. 6.1 a) for calibration and Fig. 6.1 b) for measurement.

In general the PSD delivers four intensities $I_0 \dots I_3$, which are linearly independent with respect to the state of polarization. In a calibration procedure several known polarization states are generated by the PSG, which consists of a linear polarizer and a quarter-wave plate. Each state is represented by a Stokes vector \mathbf{S}_i and corresponds in an unambiguous manner to a set of intensities $I_{0i} \dots I_{3i}$. These are also combined to a vector \mathbf{I}_i , and therefore we write the relationship in matrix algebra as

$$\mathbf{I}_i = \mathbf{A}\mathbf{S}_i \quad (6.1)$$

where \mathbf{A} is a 4×4 -matrix, the so called *instrument matrix*.

In general four independent states would suffice to determine \mathbf{A} unambiguously. This is designated as the *four-point calibration method*, and is described by Azzam et al. [14]. But to overcome errors due to imperfections in the optical elements of the PSG, the *equator-pole calibration method* is used. This method was developed by Azzam and Lopez [15] and was further investigated for the use with the DOAP by Krishnan [16]. In this case a set of linear and circularly polarized states are applied and \mathbf{A} is computed by means of a least squares algorithm. More details to the calibration are given in chapter 6.3.

Once the instrument matrix is obtained, any state of polarization can be detected. For this purpose the intensity vector \mathbf{I} is measured by the PSD and the appropriate Stokes vector \mathbf{S} is computed by inverting equation (6.1)

$$\mathbf{S} = \mathbf{A}^{-1}\mathbf{I} \quad (6.2)$$

During the pulse-heating experiment $+45^\circ$ linear polarized light is applied to the wire sample and the PSD collects the reflected light at an angle of about 140° (see Fig. 6.1 b)). From the measured Stokes vector we finally obtain normal-spectral emissivity $\epsilon_\lambda(0)$ at 684.4 nm , using the formalism introduced in chapter 5.

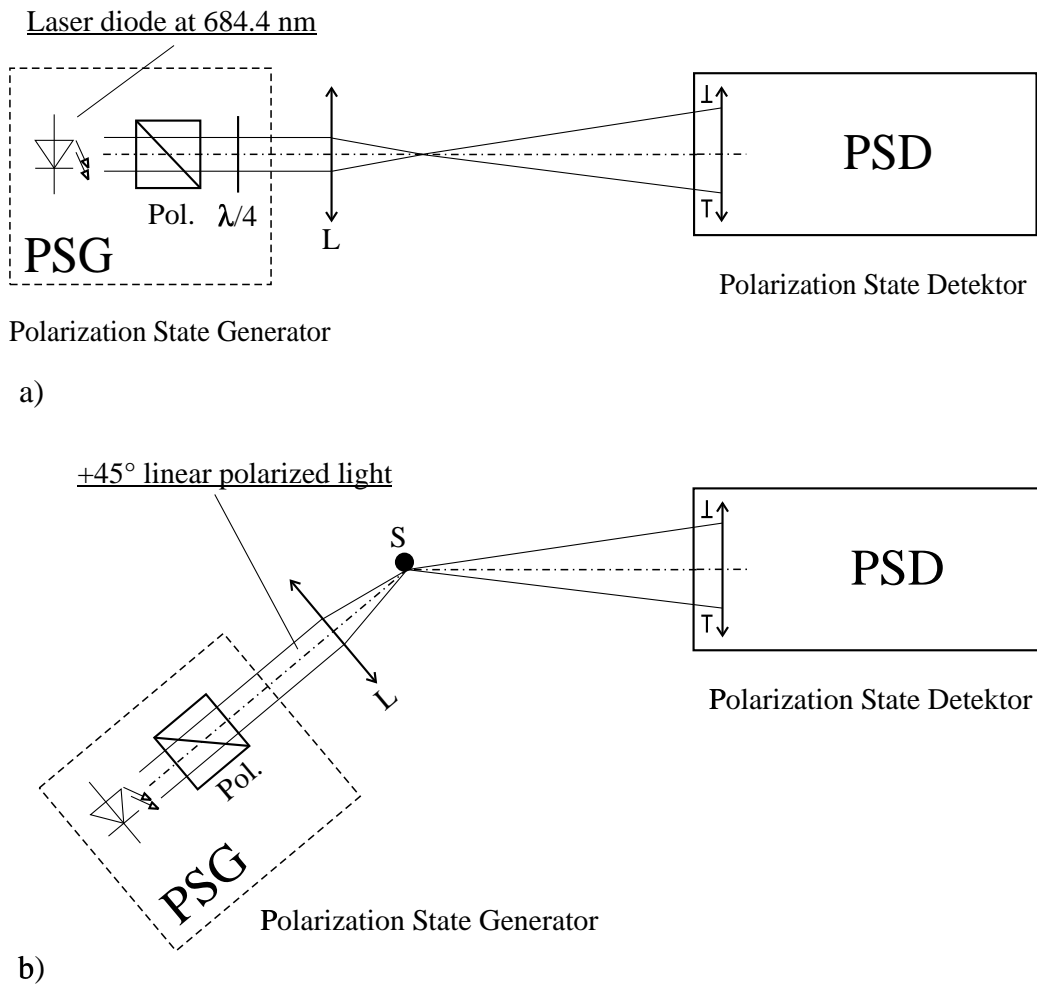


Figure 6.1: Principle of the division-of-amplitude photopolarimeter (DOAP)

a) in calibration position

b) in measurement position

Pol.: Polarizer; $\lambda/4$: quarter-wave plate; *L*: lens; *S*: sample.

6.2 Experimental setup

The polarization state detector (PSD) is the heart of the DOAP, and so this device is discussed first. The schematic drawing is shown in Fig. 6.2.

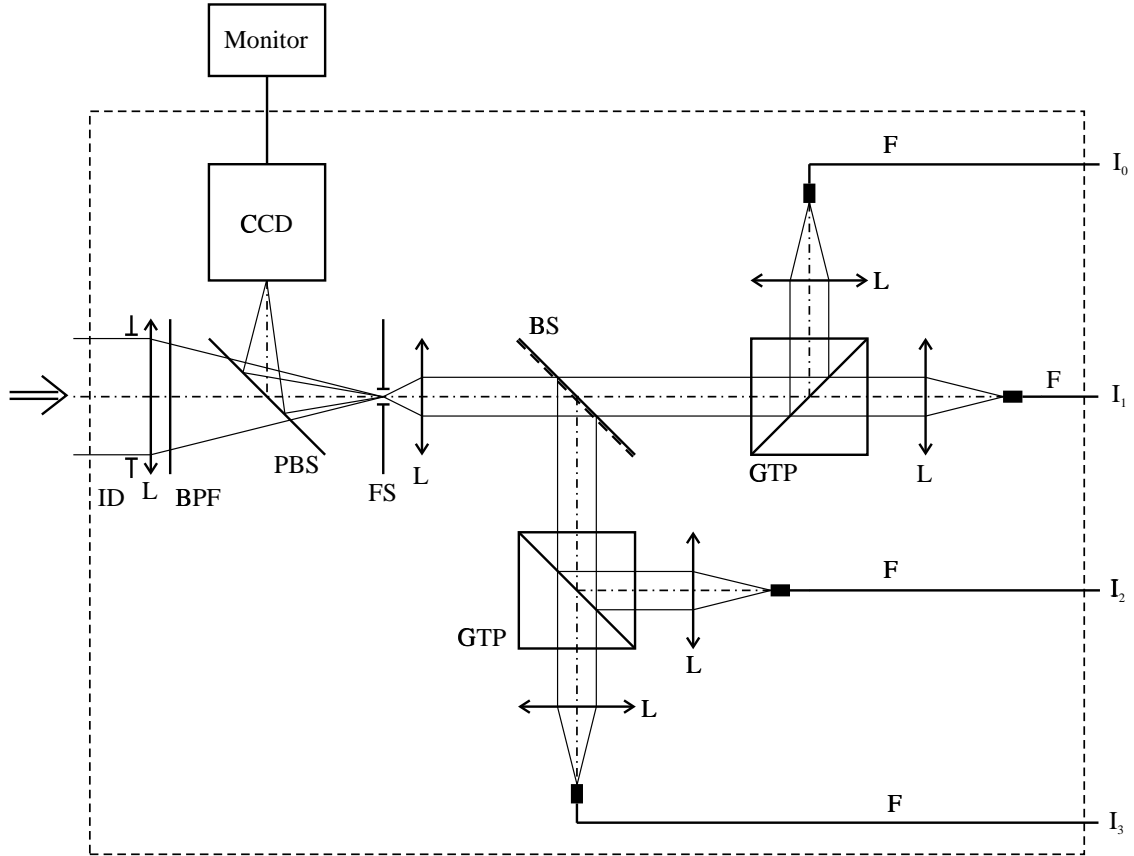


Figure 6.2: Schematic drawing of the polarization state detector (PSD)

CCD: CCD-camera for alignment works; *PBS*: pellicle beam splitter; *BS*: coated beam splitter; *GTP*: Glan-Thompson-prism; *ID*: iris diaphragm; *FS*: field stop; *L*: lens; *BPF*: band-pass filter at 684.4 nm ; *F*: single-mode fiber; $I_0 \dots I_3$: four intensities representing unambiguously the state of polarization.

The incoming light passes first an iris diaphragm for variable light attenuation. This allows to restrict the intensity signals to avoid overloads in the electronic input stages. The light originates from a laser diode at 684.4 nm , see Fig. 6.1, and passes in the PSD a narrow band-pass filter *BPF* of the same wavelength. This is due to reject most of the background light and particularly the incandescent radiation of the sample. A pellicle beam splitter *BPS* images the surface of the field stop *FS* onto a CCD-camera. Therefore the position of the incoming beam focused onto *FS* can be observed, which is used to align the PSD.

In the following the light of unknown state of polarization is divided up into two beams by the beam splitter *BS*, which is made of zinc sulfide and is coated with a thin layer of magnesium fluoride. This produces a phase shift between the reflected and transmitted components. The thickness of the magnesium fluoride layer as well as the reflectance and transmittance angles of the beam splitter are chosen to minimize the uncertainties arising from the inversion of the instrument matrix (see chapter 6.5).

The exiting beams are analysed by Glan-Thompson prisms GTP . These are linear polarizers with outputs for the two orthogonal components. Finally the four outgoing beams are coupled into optical single-mode fibers and are converted into electrical signals by silicon photodiodes in the electronics box.

The key is that the four intensity signals represent the state of polarization in an unambiguous manner. But as outlined in the foregoing chapter, a calibration procedure is needed to assign these intensities to the appropriate Stokes vector. Fig. 6.3 shows the setup of the DOAP system in calibration position.

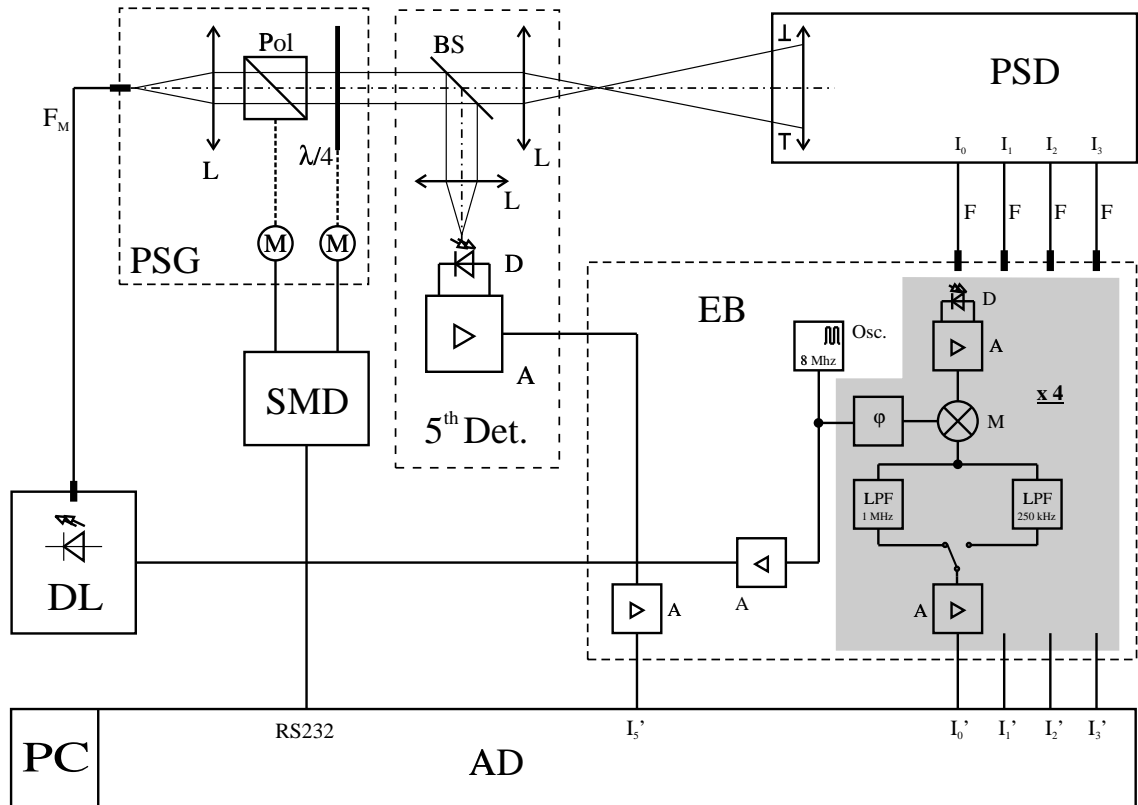


Figure 6.3: Schematic experimental setup of the DOAP in calibration position
 PSG : polarization state generator; PSD : polarization state detector; $5^{th} Det.$: 5^{th} -detector for laser intensity measurement; SMD : stepper motor driver; DL : diode laser at 684.4 nm ; EB : electronics box; PC : personal computer; AD : analog-to-digital converter; L : lens; Pol : linear polarizer; $\lambda/4$: quarter-wave retarder; M : motorized rotary stage; BS : beam splitter; D : photodiode; A : amplifier; $Osc.$: oscillator for lock in technique; φ : phase shifter; M : mixer; LPF : low-pass filter; F_M : multi-mode fiber; F : single-mode fiber; $I_0 \dots I_3$: intensities from PSD ; $I'_0 \dots I'_3$: intensity signals after demodulation; I'_5 : intensity signal 5^{th} -detector; $RS232$: RS-232 serial interface.

The light coming from the laser diode DL is coupled into an optical multimode fiber. The laser itself and all the electronics are placed in the shielded room together with the other data acquisition equipment, see chapter 2. The fibers are non conducting and therefore provide ideal isolation between the shielded room and the experimental setup outside.

The PSG consists of a linear polarizer and a quarter-wave retarder, both mounted in motorized rotary stages. With the use of a stepper motor controller each state of polarization can be achieved by computer control.

Within the calibration procedure the intensity of the laser light incident on the PSD has to be known. The difficulty of this task is to have a transmitting detector, which doesn't change the state of polarization. This is done by a specially designed beam splitter and the whole device is called the 5th-detector.

After calibration arbitrary polarized states can be detected with the PSD. The goal of applying the DOAP to pulse heating experiments is to achieve emissivity of the sample material. For this reason the PSG is set to produce +45° linear polarized light. The PSD is arranged under an angle of about 140°, see Fig. 6.4, and collects the reflected light coming from the sample surface.

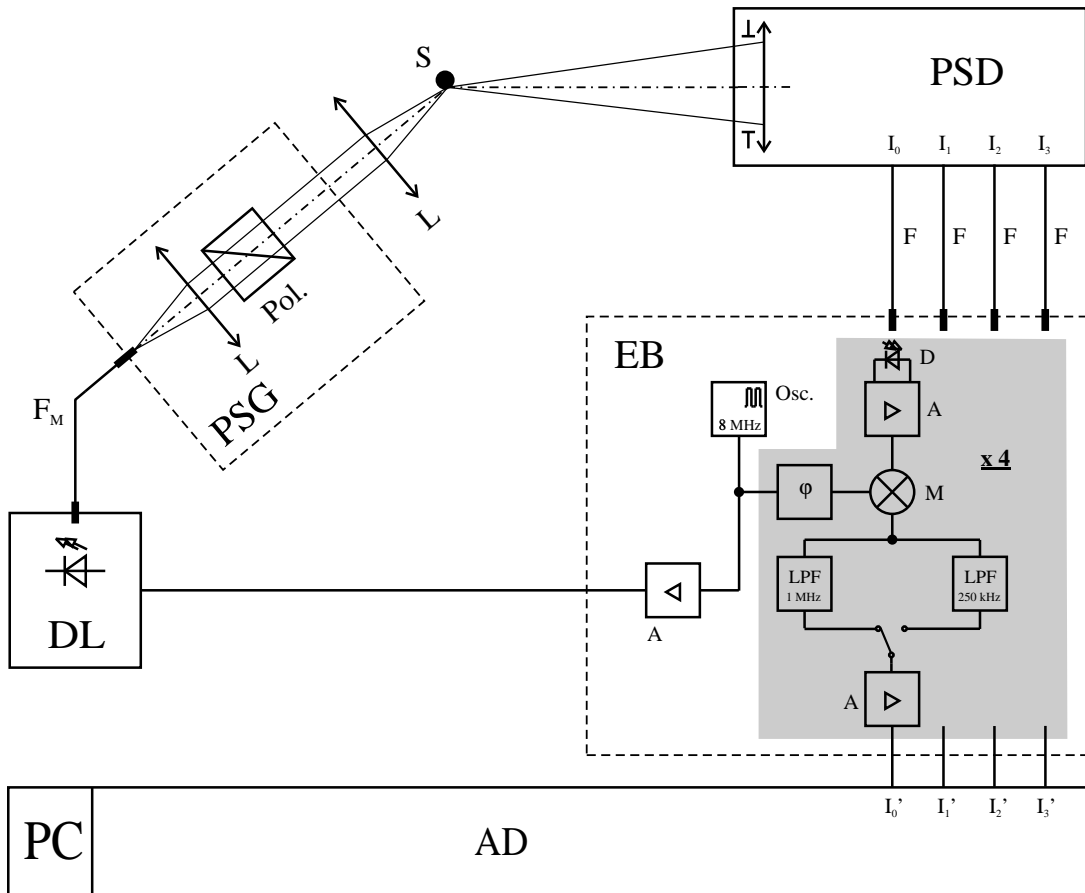


Figure 6.4: Schematic experimental setup of the DOAP in measurement position
 PSG: polarization state generator; PSD: polarization state detector; S: sample; DL: diode laser at 684.4 nm ; EB: electronics box; PC: personal computer; AD: analog-to-digital converter; L: lens; Pol: linear polarizer; D: photodetector; A: amplifier; Osc.: oscillator for lock in technique; φ: phase shifter; M: mixer; LPF: low pass filter; F_M: multi-mode fiber; F: single-mode fiber; I₀ . . . I₃: intensities from PSD; I'₀ . . . I'₃: intensity signals after demodulation.

Electronics

During the experiment the wire sample is heated up far above the melting point. To reject the incandescent radiation of the wire sample and also any background light, a lock-in technique is used. In this case the laser light is modulated by an 8 MHz square-wave signal, the so-called carrier, which simply switches the laser on and off. For this purpose a PPMT LASER DIODE OEM SYSTEM with a wavelength of 684.4 nm from Power Technology Incorporated is used, which is designed for external TTL compatible modulation and to actively control the laser temperature. During the 'on'-period the laser diode is driven by a constant current, and the output power is not monitored as in other systems. Therefore the 5th-detector is needed to check the total intensity during calibration. The wavelength depends on temperature of the laser diode, and so an active temperature stabilization is implemented within the laser module.

The four intensities from the PSD are transmitted by optical fibers and are converted into electrical signals by silicon photodiodes. The block diagram of the input stage is shown in Fig. 6.5. The input amplifiers are specially designed for high gain, high speed and low noise. Additionally a low-pass filter with a time constant of about 0.1 ms is applied to the feedback-loop. This acts as an active suppression of the incandescent radiation coming from the wire sample, while the high-frequency component of the lock-in system at 8 MHz is not affected.

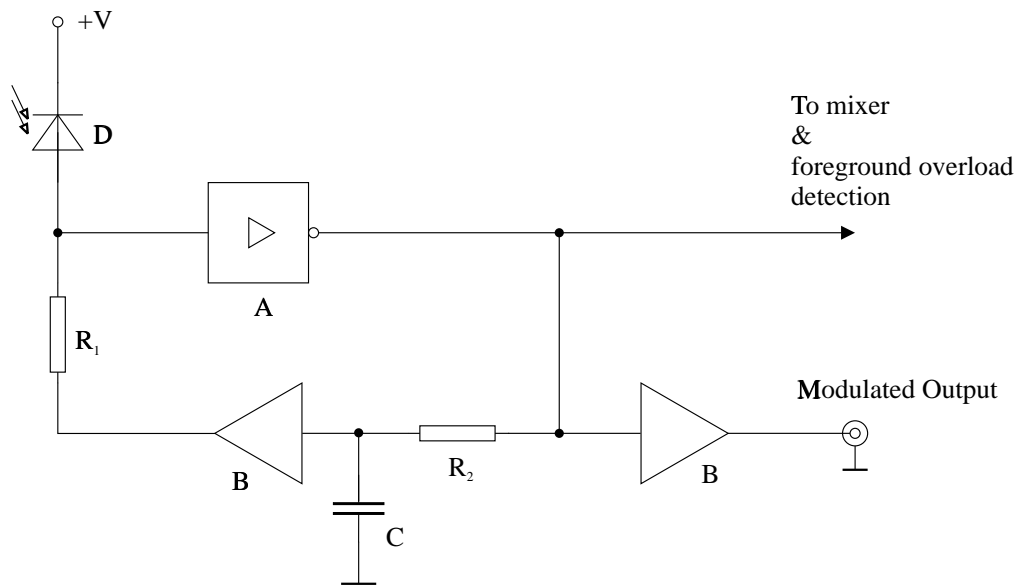


Figure 6.5: Block diagram of the DOAP input stages

+V: positive voltage supply; D: photodiode; A: high speed - low noise amplifier; R_1 : feedback-resistor; C, R_2 : low-pass filter; B: buffer amplifier.

The output signals of the input amplifiers are directly available at the back of the electronics box via BNC-connectors labelled 'Modulated Output'. On the other hand the signals are supplied to an overload detector. So if the levels exceed a certain value the detector signals the error by a LED at the front of the electronics box. The overload state is also stored by a flip-flop, which must be either set back manually at the front panel or by computer control. Additionally, a background overload detector was foreseen, but due to problems with unwanted oscillations in the electronics it actually is not connected.

The heart of the lock-in detector is the mixer. It is an analog multiplier, which is fed on one side by the output signals of the input amplifiers and on the other side by the reference signal of the oscillator. A phase shifter compensates the propagation delay of the measuring signals. At the mixer output there occur the demodulated signal as well as the 8 MHz -component of the carrier. Therefore a low-pass filter is used to separate these two components. The DOAP system provides two filters, one at 250 MHz and the other at 1 MHz . They are selected by a switch on the front panel of the electronics box.

The demodulated signals are available at the output BNC-connectors labelled 'Output to Digitizers'. These are connected to a plug-in four-channel AD-converter card (Datel PCI-416) with 12 bit resolution and a maximum sampling rate of 2.5 MHz (minimum sample interval 0.4 μs). The sample depth is normally set to 1024 bytes per channel. A second four-channel AD-converter card is foreseen for sampling the pulse heating signals such as voltages, current and intensity of radiation. But the consisting INSIGHT - data acquisition is preferred due to the higher sampling rate of 10 MHz . More to this topic and the necessary data reduction see chapter 7.1.

During calibration the total intensity is measured by the 5th-detector. The output signal is digitized by a slow 16-bit AD-conversion card (Computerboards Dash 1602/16). This card also provides digital I/O-channels to control the electronics box via computer.

6.3 Calibration procedure

Before the DOAP can be used to measure optical parameters, the instrument matrix has to be determined during the calibration procedure. As mentioned in chapter 6.1 this is done using the *equator-pole calibration method*, which will be described within this chapter. The DOAP is arranged as shown in Fig. 6.3 and therefore a lot of alignment work has to be performed. These will be described thoroughly by Seifter [4].

In the first step of calibration only linear polarized states are applied. Therefore the retarder is removed from the PSG and the linear polarizer is rotated in steps of 10° from 0° to 360° . The so generated states of polarization are described by the Stokes vector (5.99). The theoretical values for S_1 and S_2 as a function of rotation angle θ_P of the linear polarizer are shown in Fig. 5.19. They are periodic by 180° and consequently the intensities are the same at θ_P and $\theta_P + 180^\circ$. For the further evaluation the mean of these two values is used

$$I_i(\theta_P) = \frac{I'_i(\theta_P) + I'_i(\theta_P + 180^\circ)}{2} \quad \begin{array}{l} \theta_P = 0, 10, 20, \dots 180^\circ \\ i = 0 \dots 3 \end{array} \quad (6.3)$$

where I'_i denotes the measured intensity signals, which are offset corrected, and are normalized by division through the 5th-detector signal. As mentioned in the foregoing chapter, this is necessary due to fluctuations in laser power.

Applying the Stokes vectors (5.99) for the different linear states to equation (6.1) we have

$$\begin{pmatrix} I_0(\theta_P) \\ I_1(\theta_P) \\ I_2(\theta_P) \\ I_3(\theta_P) \end{pmatrix} = \begin{pmatrix} a_{00} & a_{01} & a_{02} & a_{03} \\ a_{10} & a_{11} & a_{12} & a_{13} \\ a_{20} & a_{21} & a_{22} & a_{23} \\ a_{30} & a_{31} & a_{32} & a_{33} \end{pmatrix} \begin{pmatrix} 1 \\ \cos 2\theta_P \\ \sin 2\theta_P \\ 0 \end{pmatrix} \quad (6.4)$$

Solving this matrix equation for the intensity components we get

$$I_i(\theta_P) = a_{i0} + a_{i1} \cos 2\theta_P + a_{i2} \sin 2\theta_P \quad \begin{array}{l} \theta_P = 0, 10, 20, \dots 180^\circ \\ i = 0 \dots 3 \end{array} \quad (6.5)$$

This represents a linear set of equations. It is overdefined, because four independent states would suffice to determine the instrument matrix unambiguously, while actually there are 19 measured linear states (after reduction by (6.3)). This leads to higher accuracy in calculating the a_{ij} using a least squares algorithm.

Equation (6.5) can also be seen as a Fourier series with the a_{ij} as Fourier coefficients. So in literature (e.g. Krishnan [16]) the evaluation of these components is often referred to as Fourier analysis.

Because of S_3 is zero for all linear states, only the first three columns of the instrument matrix are achieved during this first step. The last column is obtained by applying circularly polarized states. This is done by inserting the retarder into the PSG and maintaining an angle of $\pm 45^\circ$ between linear polarizer and the retarder, while both are rotated in steps of 20° from $\theta = 0^\circ$ to 360° . So 19 RCP-states (corresponding to $+45^\circ$) are measured as well as 19 LCP-states (-45°). The intensities of the RCP- and LCP-states should be equal, and for further evaluation their mean values are computed.

$$\begin{array}{l} I_{i, RCP} = \frac{1}{19} \sum I'_{i, RCP}(\theta) \\ I_{i, LCP} = \frac{1}{19} \sum I'_{i, LCP}(\theta) \end{array} \quad \begin{array}{l} \theta = 0, 20, 40, \dots 360^\circ \\ i = 0 \dots 3 \end{array} \quad (6.6)$$

Indicators for the quality of the calibration are the standard deviations sd_i of the RCP- and LCP-components. They are computed by

$$\begin{aligned}
 sd_{i, RCP} &= \sqrt{\frac{1}{19-1} \sum (I'_{i, RCP}(\theta) - I_{i, RCP})^2} \\
 sd_{i, LCP} &= \sqrt{\frac{1}{19-1} \sum (I'_{i, LCP}(\theta) - I_{i, LCP})^2}
 \end{aligned} \tag{6.7}$$

Applying the Stokes vectors (5.100) for RCP- and LCP-polarized light to equation (6.1) we have

$$\begin{pmatrix} I_0 \\ I_1 \\ I_2 \\ I_3 \end{pmatrix} = \begin{pmatrix} a_{00} & a_{01} & a_{02} & a_{03} \\ a_{10} & a_{11} & a_{12} & a_{13} \\ a_{20} & a_{21} & a_{22} & a_{23} \\ a_{30} & a_{31} & a_{32} & a_{33} \end{pmatrix} \begin{pmatrix} 1 \\ 0 \\ 0 \\ \pm 1 \end{pmatrix} \tag{6.8}$$

Solving this matrix equation for the RCP- and LCP-component we find

$$\begin{aligned}
 I_{i, RCP} &= a_{i0} + a_{i3} & i = 0 \dots 3 \\
 I_{i, LCP} &= a_{i0} - a_{i3}
 \end{aligned} \tag{6.9}$$

From this it is easy to obtain the desired fourth column of the instrument matrix as following

$$a_{i3} = \frac{I_{i, RCP} - I_{i, LCP}}{2} \quad i = 0 \dots 3 \tag{6.10}$$

Now the instrument matrix is complete and the result is stored in an ASCII-file for further evaluations.

Additionally, adding the two equations of 6.9 we again obtain the first column of the instrument matrix:

$$a_{i0} = \frac{I_{i, RCP} + I_{i, LCP}}{2} \quad i = 0 \dots 3 \tag{6.11}$$

On the other hand, we have got the a_{i0} from measuring the linear states. Of course the two evaluations should provide the same results. The differences, the so called consistencies c_i , are a further indicator for the quality of the calibration. The c_i are represented as relative quantities defined by

$$c_i = \frac{a_{i0, c} - a_{i0, p}}{a_{i0, p}} \cdot 100 \% \quad i = 0 \dots 3 \tag{6.12}$$

where $a_{i0, p}$ denotes the first column of the instrument matrix obtained from the measurement of linear states and $a_{i0, c}$ of circular states.

In the following an example of a calibration is given. First, Fig. 6.6 shows the total intensity after the PSG when rotating the linear polarizer. One can see, that the light delivered to the PSG is not unpolarized, but in some way elliptically polarized. This occurs due to changes of the state of polarization within the optical fiber which connects laser and PSG, while the laser itself is linear polarized. Another problem is the non-Gaussian beam profile at the output of the fiber. More to this topic will be given by Seifter [4].

Fig. 6.7 shows the four intensity signals from the PSD during the application of linear states. These data points are first normalized with respect to the total intensity signal

from the 5th-detector, and then they are fitted using equation 6.5. The result is shown in Fig. 6.8, where the marked points represent measured values. The lines are recalculated from 6.5 using the first three rows of the fitted instrument matrix.

To obtain the fourth row of the instrument matrix the measurement of circular states yielded

$$\mathbf{I}_{RCP} = \begin{pmatrix} +0.983 \pm 0.024 \\ +0.267 \pm 0.008 \\ +0.144 \pm 0.001 \\ +0.355 \pm 0.005 \end{pmatrix} \quad \mathbf{I}_{LCP} = \begin{pmatrix} +0.472 \pm 0.017 \\ +0.638 \pm 0.016 \\ +0.202 \pm 0.002 \\ +0.232 \pm 0.002 \end{pmatrix} \quad (6.13)$$

and the consistencies

$$\mathbf{c} = \begin{pmatrix} -0.400 \% \\ +0.106 \% \\ -1.311 \% \\ -0.968 \% \end{pmatrix} \quad (6.14)$$

Finally, the obtained instrument matrix is stored in the file 'auto_cal.051' and reads as

$$\mathbf{A} = \begin{pmatrix} +0.731 & +0.162 & -0.623 & +0.256 \\ +0.452 & +0.111 & +0.392 & -0.186 \\ +0.175 & -0.151 & -0.075 & -0.029 \\ +0.297 & -0.244 & +0.107 & +0.061 \end{pmatrix} \quad (6.15)$$

This calibration is one of the best we have done so far. This can be seen from the verification (see chapter 6.4), which shows an average error of the Stokes parameters of 0.009.

At least, Fig. 6.9 shows a poor calibration. The position of the measured data points at I_2 and I_4 indicate problems in the alignment of the PSD. As one can see, the values for θ_P and $\theta_P + 180^\circ$ are not the same. While rotating the linear polarizer it comes to slight changes in the direction of the outgoing beam. If the PSD is not well aligned, it is very sensitive to this changes and therefore the mentioned deviations occur. Additionally, the error in the I_1 -intensity signal was due to an overload in the electronics, because the total intensity was too high.

The standard deviation of circular states and the consistencies (the indicators of how good the calibration has been performed) are now

$$\mathbf{I}_{RCP} = \begin{pmatrix} +0.989 \pm 0.024 \\ +0.266 \pm 0.003 \\ +0.145 \pm 0.004 \\ +0.356 \pm 0.006 \end{pmatrix} \quad \mathbf{I}_{LCP} = \begin{pmatrix} +0.481 \pm 0.018 \\ +0.656 \pm 0.026 \\ +0.208 \pm 0.006 \\ +0.244 \pm 0.006 \end{pmatrix} \quad (6.16)$$

$$\mathbf{c} = \begin{pmatrix} -0.461 \% \\ -2.128 \% \\ -1.010 \% \\ -0.698 \% \end{pmatrix} \quad (6.17)$$

Comparing the data of these two calibrations, one can see, that the RCP-values are rather equal, while the LCP-values differ by about 0.01. The maximum difference is given at the second detector by 0.018, and also the consistency of this detector is much larger than before. This is in turn a problem of PSD-alignment. The verification of this poor calibration shows an average error of the Stokes parameters of 0.02, which is double the value of the good calibration.

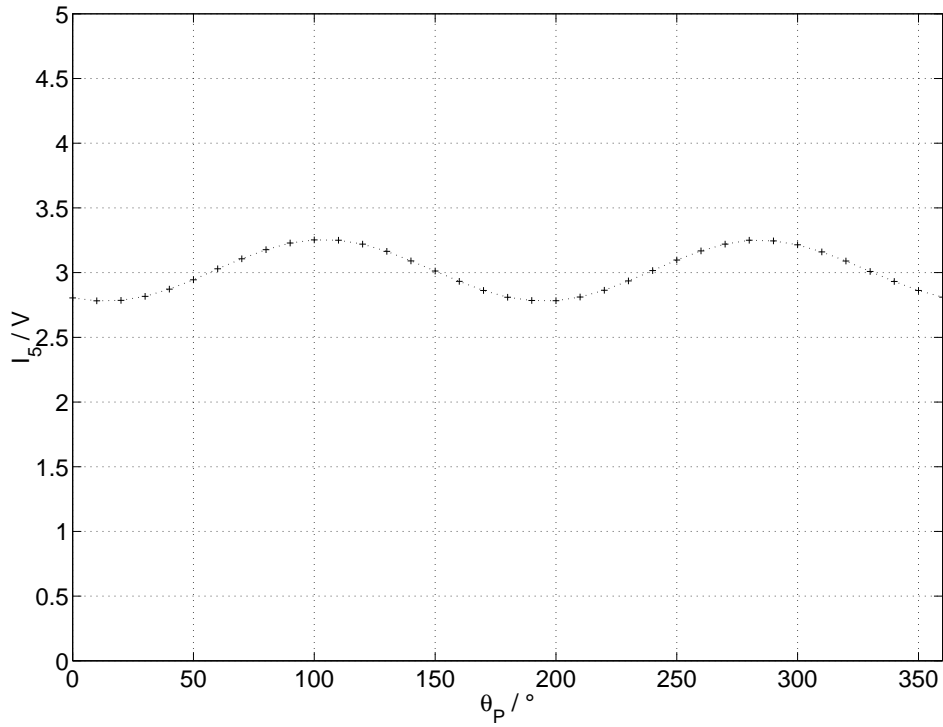


Figure 6.6: Intensity signal of the 5th-detector while applying linear states for calibration
 I_5 : intensity signal; θ_P : rotation angle of the linear polarizer.

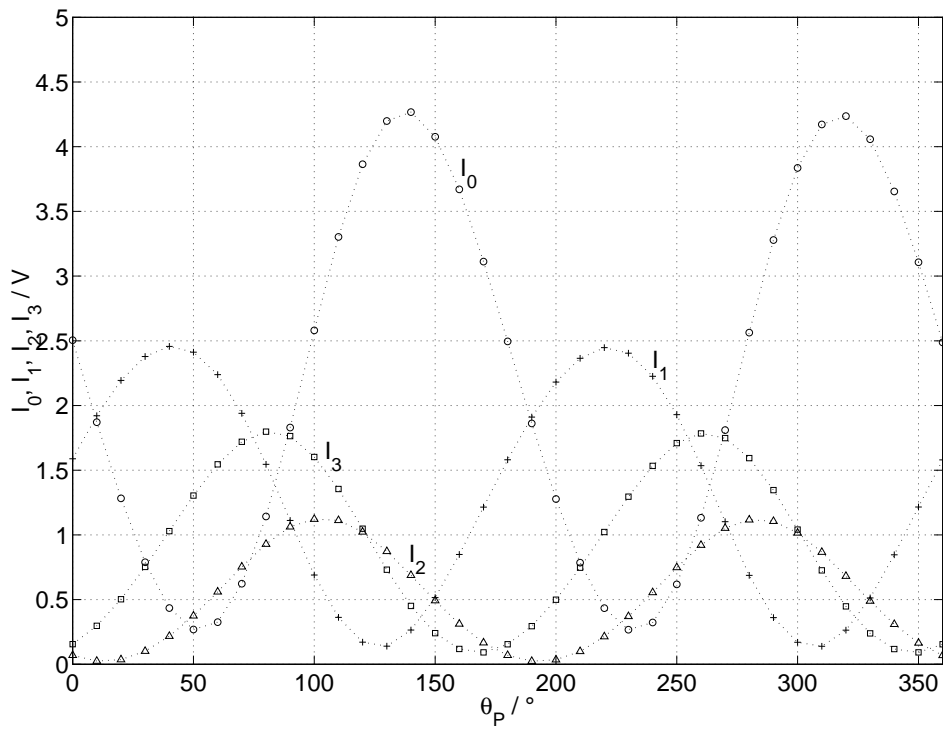


Figure 6.7: Intensity signals from the PSD while applying linear states for calibration
 I_0, I_1, I_2, I_3 : intensity signals; θ_P : rotation angle of the linear polarizer.

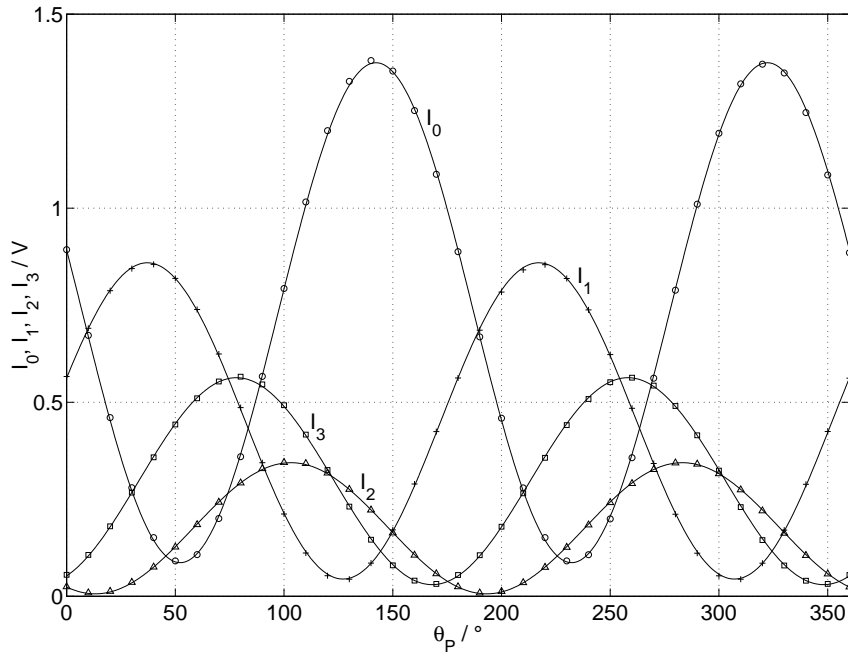


Figure 6.8: Intensity signals normalized by the signal of the 5th-detector while applying linear states for calibration. The marked points are measured values, the line represents theoretical values
 I_0, I_1, I_2, I_3 : normalized intensity signals; θ_P : rotation angle of the linear polarizer.

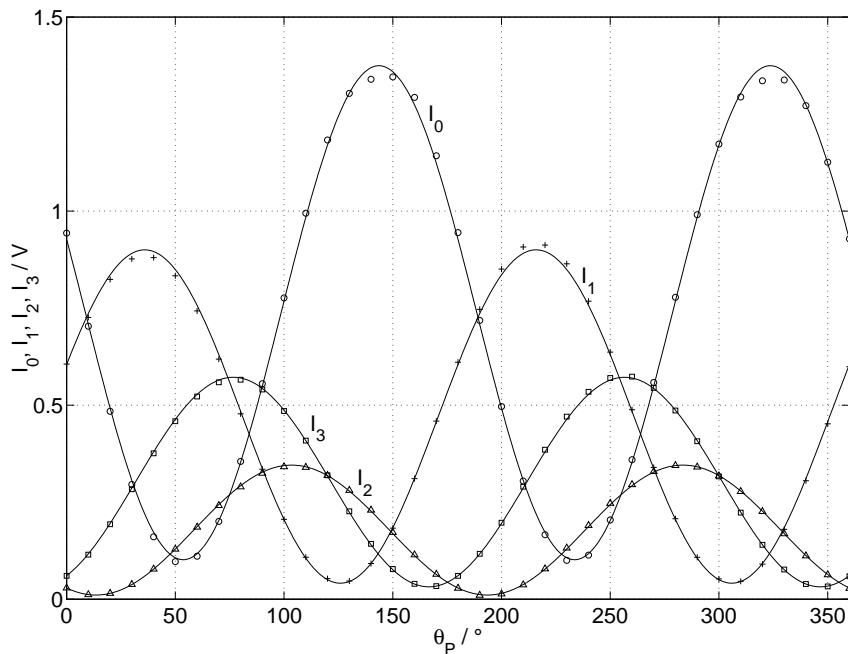


Figure 6.9: Intensity signals as in Fig. 6.8 for a poor calibration
 I_0, I_1, I_2, I_3 : normalized intensity signals; θ_P : rotation angle of the linear polarizer.

6.4 Verification of the calibration

The verification procedure is intended to estimate how good the calibration has been performed. In this case the linear polarizer is set to zero and the quarter-wave retarder is rotated in steps of 10° from 0° to 360° . The measured Stokes parameters S_i at a rotation angle θ_C of the retarder are compared to the theoretical values of equation (5.101). The results are shown in Fig. 6.10 for the good calibration of the last chapter, and in Fig. 6.11 for an other poor calibration. In the last figure one can see clearly the deviations of the measured Stokes parameters from the theoretical values.

Since it is rather difficult to see small deviations in the graphical representation, also numerical values are derived for an estimation of the performance of the calibration. So the mean deviations between measured and theoretical Stokes parameters are computed by

$$\Delta S_i = \frac{1}{37} \sum |S_i - S'_i| \quad i = 1 \dots 3 \quad (6.18)$$

where S_i denotes the theoretical and S'_i the measured values. The total RMS-error is defined by

$$\Delta S_{tot} = \sqrt{S_1^2 + S_2^2 + S_3^2} \quad (6.19)$$

These values are calculated at the end of the verification procedure. For example, the good calibration delivered

$$\begin{aligned} \Delta S_1 &= 0.005 \\ \Delta S_2 &= 0.004 \\ \Delta S_3 &= 0.006 \end{aligned} \quad (6.20)$$

$$\Delta S_{tot} = 0.009 \quad (6.21)$$

and the poor one

$$\begin{aligned} \Delta S_1 &= 0.017 \\ \Delta S_2 &= 0.017 \\ \Delta S_3 &= 0.033 \end{aligned} \quad (6.22)$$

$$\Delta S_{tot} = 0.040 \quad (6.23)$$

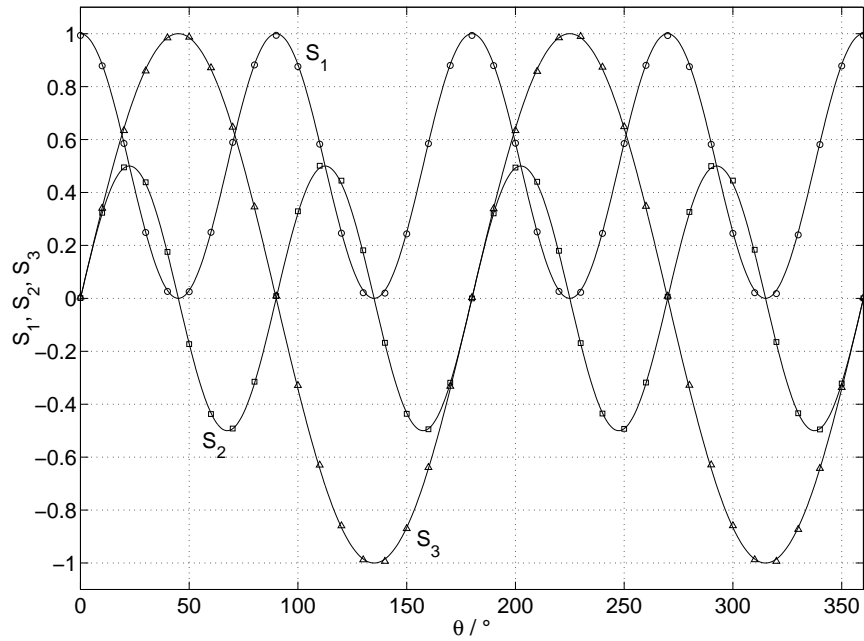


Figure 6.10: Stokes parameters during verification of the calibration. The marked points are measured values, the line represents theoretical values

S_1 , S_2 , S_3 : Stokes parameters; θ : rotation angle of linear polarizer and quarter-wave retarder.

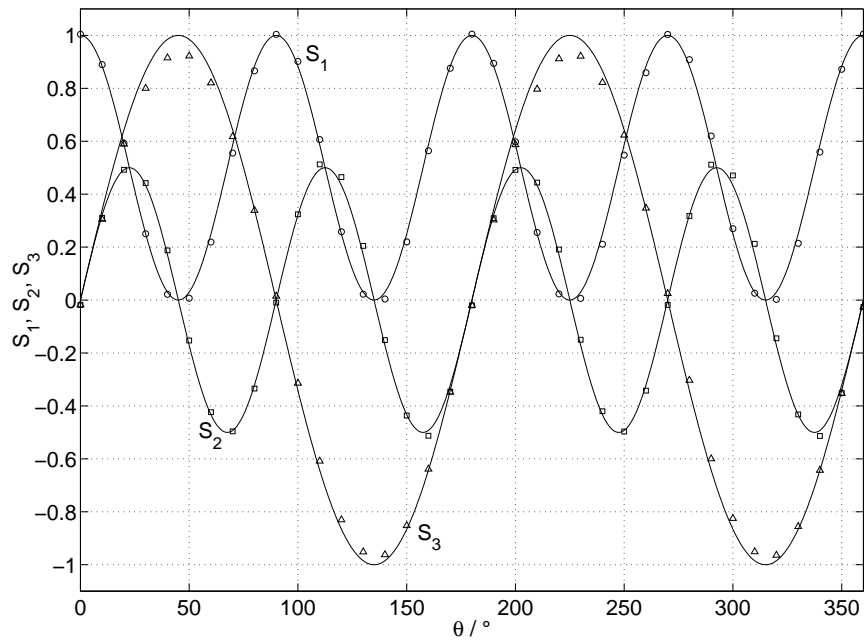


Figure 6.11: Stokes parameters as in Fig. 6.10 for a poor calibration

S_1 , S_2 , S_3 : Stokes parameters; θ : rotation angle of linear polarizer and quarter-wave retarder.

6.5 Instrument matrix

The instrument matrix is in some way the fingerprint of the DOAP-system. Therefore it is important to find an interpretation of its rows and columns. This is given by Azzam [17], and a general analysis and optimization of the instrument matrix is found by Brudzewski [18].

For the further evaluations the instrument matrix has to be inverted and normalized in different ways. To do so, there is the small program *CALNORM*, which delivers the computed data in an ASCII-file. The printout reads as

Date: 12-Apr-2000

File: auto_cal.051 28-Mar-2000 12:26:46

Instrument matrix:

```
+0.7308 +0.1615 -0.6235 +0.2556
+0.4519 +0.1107 +0.3921 -0.1859
+0.1753 -0.1514 -0.0749 -0.0287
+0.2967 -0.2440 +0.1074 +0.0614
```

Inverse matrix:

```
+0.5518 +0.8396 +0.4614 +0.4597
+0.6929 +0.9343 -2.9054 -1.4130
-0.4319 +0.6317 -3.4125 +2.1184
+0.8431 -1.4499 -7.8060 +4.7451
```

Determinant of instrument matrix: +0.0229

Condition number of instrument matrix: +10.5425

Normalized instrument matrix with respect to the first element:

```
+1.0000 +0.2210 -0.8532 +0.3498
+0.6185 +0.1514 +0.5366 -0.2544
+0.2399 -0.2072 -0.1024 -0.0392
+0.4060 -0.3339 +0.1470 +0.0840
```

Inverse normalized instrument matrix:

```
+0.4033 +0.6135 +0.3372 +0.3359
+0.5064 +0.6827 -2.1232 -1.0325
-0.3156 +0.4616 -2.4938 +1.5481
+0.6161 -1.0595 -5.7044 +3.4676
```

Determinant of normalized instrument matrix: +0.0803

Condition number of normalized instrument matrix: +10.5425

Normalized instrument matrix with respect to the first element of each row:

```
+1.0000 +0.2210 -0.8532 +0.3498
+1.0000 +0.2448 +0.8676 -0.4113
+1.0000 -0.8637 -0.4269 -0.1634
+1.0000 -0.8224 +0.3622 +0.2069
```

Determinant of normalized instrument matrix: +1.3330

In the following a short overview of the article of Azzam [17] is given and the results are applied to the instrument matrix of our DOAP-system.

The instrument matrix relates the Stokes vector $\mathbf{S} = (S_0, S_1, S_2, S_3)$ of the incident light linearly to the intensities $\mathbf{I} = (I_0, I_1, I_2, I_3)$ measured by the PSD in the form

$$\mathbf{I} = \mathbf{A}\mathbf{S} \quad (6.24)$$

For the measurement of polarization states the instrument matrix has to be inverted

$$\mathbf{S} = \mathbf{A}^{-1}\mathbf{I} \quad (6.25)$$

The essential condition for matrix inversion is, that \mathbf{A} is non-singular, hence \mathbf{A}^{-1} exists. This requires also the determinant of \mathbf{A} to be non-zero.

Interpretation of rows

The instrument matrix can be expressed in terms of its rows as

$$\mathbf{A} = \begin{pmatrix} \mathbf{A}_0 \\ \mathbf{A}_1 \\ \mathbf{A}_2 \\ \mathbf{A}_3 \end{pmatrix} \quad (6.26)$$

From equation (6.24) we find for the m^{th} -intensity signal

$$\begin{aligned} I_m &= \mathbf{A}_m \mathbf{S} & m = 0 \dots 3 \\ I_m &= a_{m0}S_0 + a_{m1}S_1 + a_{m2}S_2 + a_{m3}S_3 \end{aligned} \quad (6.27)$$

where a_{mi} are the elements of \mathbf{A}_m . If we normalize this equation with respect to the first term, we get

$$I_m = a_{m0}S_0(1 + \mathbf{a}_m \mathbf{s}) \quad m = 0 \dots 3 \quad (6.28)$$

where

$$\mathbf{s} = (S_1/S_0, S_2/S_0, S_3/S_0) \quad (6.29)$$

$$\mathbf{a}_m = (a_{m1}/a_{m0}, a_{m2}/a_{m0}, a_{m3}/a_{m0}) \quad (6.30)$$

The components of \mathbf{s} are the normalized Stokes parameters S_1, S_2 and S_3 , which are also the components of the polarization state vector in the Poincaré sphere (see chapter 5.2). Therefore the scalar product $\mathbf{a}_m \mathbf{s}$ can be seen as the projection of the polarization state onto the vectors \mathbf{a}_m , when these are also represented in the Poincaré sphere. From the requirement that \mathbf{A} must be non-singular, it follows that the four \mathbf{a}_m -vectors are linear independent. This means, that their endpoints must not lie in one plane.

If we consider unpolarized light, where $\mathbf{s} = 0$, we obtain from equation (6.28)

$$I_m = a_{m0}S_0 \quad m = 0 \dots 3 \quad (6.31)$$

Consequently, \mathbf{a}_{m0} has the following meaning

$$a_{m0} = \frac{I_m}{S_0} \quad m = 0 \dots 3 \quad (6.32)$$

which is the normalized response of the m^{th} -detector per unit power of incident unpolarized radiation. Because $S_0 > 0$ and the intensities are always non-negative, we find

$$a_{m0} > 0 \quad m = 0 \dots 3 \quad (6.33)$$

Applying completely polarized light to the PSD ($|\mathbf{s}| = 1$), in turn equation (6.28) determines the amount of intensity seen by the different detectors. If the polarization state is parallel to one of the row-vectors \mathbf{a}_m , the corresponding detector will receive a maximum on intensity

$$I_{m, \max} = a_{m0} S_0 (1 + |\mathbf{a}_m|) \quad (6.34)$$

and if the polarization state is antiparallel we get a minimum

$$I_{m, \min} = a_{m0} S_0 (1 - |\mathbf{a}_m|) \quad (6.35)$$

Because the intensity signals are non-negative we find the constraints

$$|\mathbf{a}_m| \leq 1 \quad m = 0 \dots 3 \quad (6.36)$$

Consequently the intensity signals of the detectors vary in the range of

$$0 \leq I_m \leq 2 a_{m0} S_0 \quad (6.37)$$

Finally, expanding equation (6.36) we find the inequality

$$\sqrt{a_{m1}^2 + a_{m2}^2 + a_{m3}^2} \leq a_{m0} \quad m = 0 \dots 3 \quad (6.38)$$

Applying the constraints (6.33) and (6.36) to the instrument matrix (6.15) of our DOAP-system, we get

$$\begin{aligned} a_{00} = 0.7308 > 0 \quad a_{10} = 0.4519 > 0 \quad a_{20} = 0.1753 > 0 \quad a_{30} = 0.2967 > 0 \\ |\mathbf{a}_1| = 0.9482 \leq 1 \quad |\mathbf{a}_2| = 0.9909 \leq 1 \quad |\mathbf{a}_3| = 0.9772 \leq 1 \quad |\mathbf{a}_4| = 0.9221 \leq 1 \end{aligned}$$

So all inequalities are satisfied.

Fig. 6.12 shows the row-vectors of the normalized instrument matrix (6.15) in the Poincaré sphere. The appropriate normalized matrix is found in the printout of the *CALNORM*-program under '*Normalized instrument matrix with respect to the first element of each row*'. In Fig. 6.13 we see the projection of the Poincaré sphere in the S_1 - S_2 -plane, looking into the direction of S_3 .

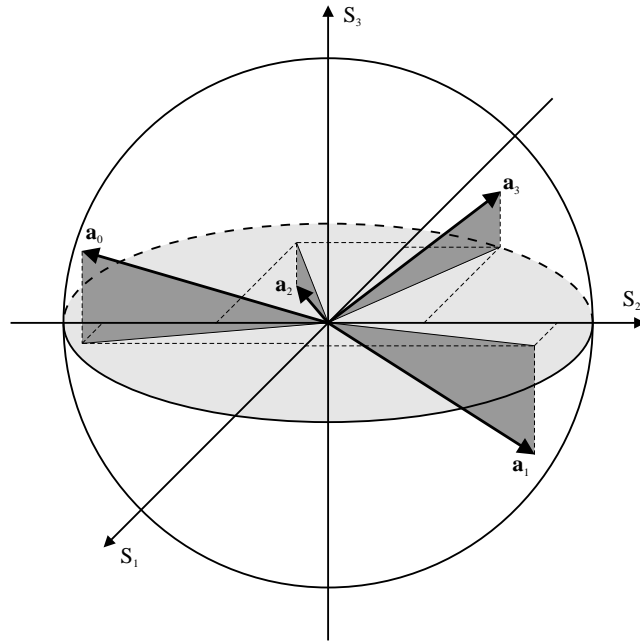


Figure 6.12: Representation of the instrument matrix in the Poincaré sphere
 S_1, S_2, S_3 : Stokes parameters; $\mathbf{a}_0, \mathbf{a}_1, \mathbf{a}_2, \mathbf{a}_3$: normalized row-vectors of the instrument matrix.

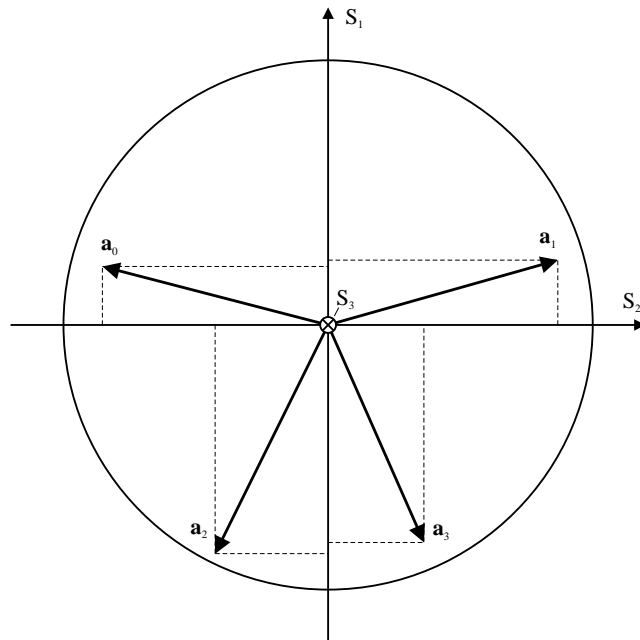


Figure 6.13: Representation of the instrument matrix in the Poincaré sphere projected onto the S_1 - S_2 -plane
 S_1, S_2, S_3 : Stokes parameters; $\mathbf{a}_0, \mathbf{a}_1, \mathbf{a}_2, \mathbf{a}_3$: normalized row-vectors of the instrument matrix.

Interpretation of columns

The instrument matrix \mathbf{A} also can be written in terms of its columns

$$\mathbf{A} = \left(\mathbf{C}_0 \quad \mathbf{C}_1 \quad \mathbf{C}_2 \quad \mathbf{C}_3 \right) \quad (6.39)$$

Applying unpolarized light, which is represented by the normalized Stokes vector $\mathbf{S}_{UPL} = (1, 0, 0, 0)$, we get using equation (6.24) and (6.39)

$$\mathbf{I}_{UPL} = \mathbf{A}\mathbf{S}_{UPL} = \mathbf{C}_0 \quad (6.40)$$

Consequently, the first row of the instrument matrix specifies the normalized response of the PSD to incident unpolarized light. This is the same result as we have already obtained in equation (6.32).

For further considerations we apply the following orthogonal states to the instrument matrix (6.39):

- Linear horizontal and vertical polarized light (LHP and LVP)

These states are represented by the Stokes vectors $\mathbf{S}_{LHP} = (1, 1, 0, 0)$ and $\mathbf{S}_{LVP} = (1, -1, 0, 0)$ and we get

$$\begin{aligned} \mathbf{I}_{LHP} &= \mathbf{A}\mathbf{S}_{LHP} = \mathbf{C}_0 + \mathbf{C}_1 \\ \mathbf{I}_{LVP} &= \mathbf{A}\mathbf{S}_{LVP} = \mathbf{C}_0 - \mathbf{C}_1 \end{aligned} \quad (6.41)$$

Combining these two equations, it immediately follows that

$$\mathbf{C}_1 = \frac{1}{2} (\mathbf{I}_{LHP} - \mathbf{I}_{LVP}) \quad (6.42)$$

Consequently, the second column of the instrument matrix represents the differential normalized response of the PSD to incident linear horizontal and vertical polarized light.

- Linear $+45^\circ$ and -45° polarized light ($+45LP$ and $-45LP$)

These states are represented by the Stokes vectors $\mathbf{S}_{+45LP} = (1, 0, 1, 0)$ and $\mathbf{S}_{-45LP} = (1, 0, -1, 0)$ and we get

$$\begin{aligned} \mathbf{I}_{+45LP} &= \mathbf{A}\mathbf{S}_{+45LP} = \mathbf{C}_0 + \mathbf{C}_2 \\ \mathbf{I}_{-45LP} &= \mathbf{A}\mathbf{S}_{-45LP} = \mathbf{C}_0 - \mathbf{C}_2 \end{aligned} \quad (6.43)$$

Combining these two equations, it immediately follows that

$$\mathbf{C}_2 = \frac{1}{2} (\mathbf{I}_{+45LP} - \mathbf{I}_{-45LP}) \quad (6.44)$$

Consequently the third column of the instrument matrix represents the differential normalized response of the PSD to incident linear $+45^\circ$ and -45° polarized light.

- Circularly right and left handed polarized light

These states are represented by the Stokes vectors $\mathbf{S}_{RCP} = (1, 0, 0, 1)$ and $\mathbf{S}_{LCP} = (1, 0, 0, -1)$ and we get

$$\begin{aligned}\mathbf{I}_{RCP} &= A\mathbf{S}_{RCP} = \mathbf{C}_0 + \mathbf{C}_3 \\ \mathbf{I}_{LCP} &= A\mathbf{S}_{LCP} = \mathbf{C}_0 - \mathbf{C}_3\end{aligned}\tag{6.45}$$

Combining these two equations, it immediately follows that

$$\mathbf{C}_3 = \frac{1}{2} (\mathbf{I}_{RCP} - \mathbf{I}_{LCP})\tag{6.46}$$

Consequently, the fourth column of the instrument matrix represents the differential normalized response of the PSD to incident circularly right and left handed polarized light.

Additionally, equations (6.41), (6.43) and (6.45) also give

$$\mathbf{C}_0 = \frac{1}{2} (\mathbf{I}_{LHP} + \mathbf{I}_{LVP}) = \frac{1}{2} (\mathbf{I}_{+45LP} + \mathbf{I}_{-45LP}) = \frac{1}{2} (\mathbf{I}_{RCP} + \mathbf{I}_{LCP})\tag{6.47}$$

This leads to the general result

$$\mathbf{C}_0 = \frac{1}{2} (\mathbf{I}_S + \mathbf{I}_{OS})\tag{6.48}$$

which indicates that the first column of the instrument matrix also represents the average of the normalized responses of the PSD to any pair of orthogonal polarization states (denoted by S and OS).

Condition number for matrix inversion

In literature (Brudzewski [18]) we find for the relative error of the measured Stokes vector

$$\frac{|\Delta \mathbf{S}|}{|\mathbf{S}|} \leq \sigma(\mathbf{A})\sigma(\mathbf{A}^{-1}) \frac{|\Delta \mathbf{I}|}{|\mathbf{I}|} \tag{6.49}$$

- $\sigma(\mathbf{A})$... spectral radius of instrument matrix \mathbf{A}
- $\sigma(\mathbf{A}^{-1})$... spectral radius of \mathbf{A}^{-1}
- \mathbf{S} ... Stokes vector obtained from (6.25)
- $\Delta \mathbf{S}$... uncertainties of the Stokes vector
- \mathbf{I} ... vector of measured intensities
- $\Delta \mathbf{I}$... uncertainties of \mathbf{I}
- $\|$... vector norm

The spectral radius $\sigma(\mathbf{M})$ of an arbitrary matrix \mathbf{M} is given by the square root of the largest eigenvalue of $\mathbf{M}^T \mathbf{M}$. In MATLAB¹ the product $\sigma(\mathbf{A})\sigma(\mathbf{A}^{-1})$ is called the *condition number for matrix inversion* and its value for the current instrument matrix is read in the printout of *CALNORM*. So we find for the instrument matrix (6.15)

$$\sigma(\mathbf{A})\sigma(\mathbf{A}^{-1}) = 10.5 \tag{6.50}$$

Assuming that each detector receives the same amount of the incoming intensity, Brudzewski [18] shows that equation (6.49) can be used to estimate the uncertainties of the Stokes parameters by

$$\left(\frac{\Delta S}{S}\right)_i \leq \left[\frac{[\sigma(\mathbf{A})\sigma(\mathbf{A}^{-1})]^2 (1 + P^2) - 1}{3P^2} \right]^{1/2} \frac{\Delta I}{I} \quad i = 1 \dots 3 \tag{6.51}$$

- P ... degree of polarization
- $\frac{\Delta I}{I}$... average value of relative uncertainties of the measured intensities

Considering a degree of polarization in the range of 0.9...1.0 and using (6.50) we obtain

$$\left(\frac{\Delta S}{S}\right)_i \leq 8.6 \frac{\Delta I}{I} \quad i = 1 \dots 3 \tag{6.52}$$

While the condition number of matrix inversion is quite important during the development of the PSD, it plays a minor role once the PSD is set up. In this case the parameters (e.g. angle of reflection of the coated beam splitter or thickness of the coating layer) are fixed and therefore the instrument matrix is given. But the condition number can be used to compare different DOAP-systems. The smaller its value, the more precise the instrument.

¹MATLAB Version 5.1, The Language of Technical Computing, Copyright ©1984-1997 The Math-Works, Inc.

6.6 Alignment to measurement position

For the measurement PSG and PSD are arranged under an angle of 140° , which corresponds to a reflection angle of 70° . This is done using a custom-built BK7-glass prism.

The optical constants of BK7-glass are well known, and we find for its refractive index n and extinction coefficient k at a wavelength of 684.4 nm in the Melles Griot catalogue 2000 [22]

$$n_{684.4 \text{ nm}} = 1.5135 \qquad k_{684.4 \text{ nm}} \approx 0 \qquad (6.53)$$

On the other hand, measuring the optical constants by means of the DOAP-system yields

$$n_{684.4 \text{ nm}} = 1.5138 \pm 0.0004 \qquad k_{684.4 \text{ nm}} = 0.115 \pm 0.001 \qquad (6.54)$$

Therefore we have an excellent agreement in the refractive index, but the extinction coefficient is rather poor. This arises from the fact, that Stokes parameter S_3 must be zero when linear polarized light is applied to non-absorptive media. Actually, S_3 was not zero during the measurement (about -0.1 for the evaluation of (6.54)), which comes from a poor alignment of the PSD. After a new alignment we achieved $S_3 = 0.009$ and $k = -0.002$. The measured values (6.54) are the mean of 1024 data points, which are shown in Fig. 6.14.

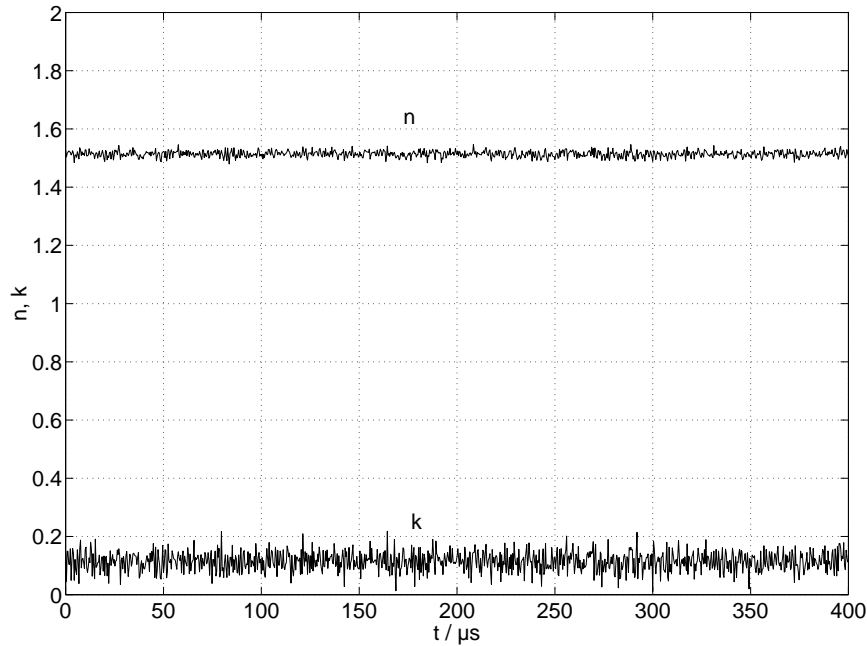


Figure 6.14: Refractive index n and extinction coefficient k of the BK7-glass prism
 t : time.

Very interesting are also the detector signals recorded during the experiment with the BK7-glass prism. They are shown in Fig. 6.15 and more detailed in Fig. 6.16. The noise level is rather high, but on a closer view we see that the signals are correlated. Therefore the major part of noise comes from fluctuations in laser intensity. These should cancel out during the normalization of the Stokes vector with respect to its first component S_0 . Only the noise coming from the input amplifiers remains.

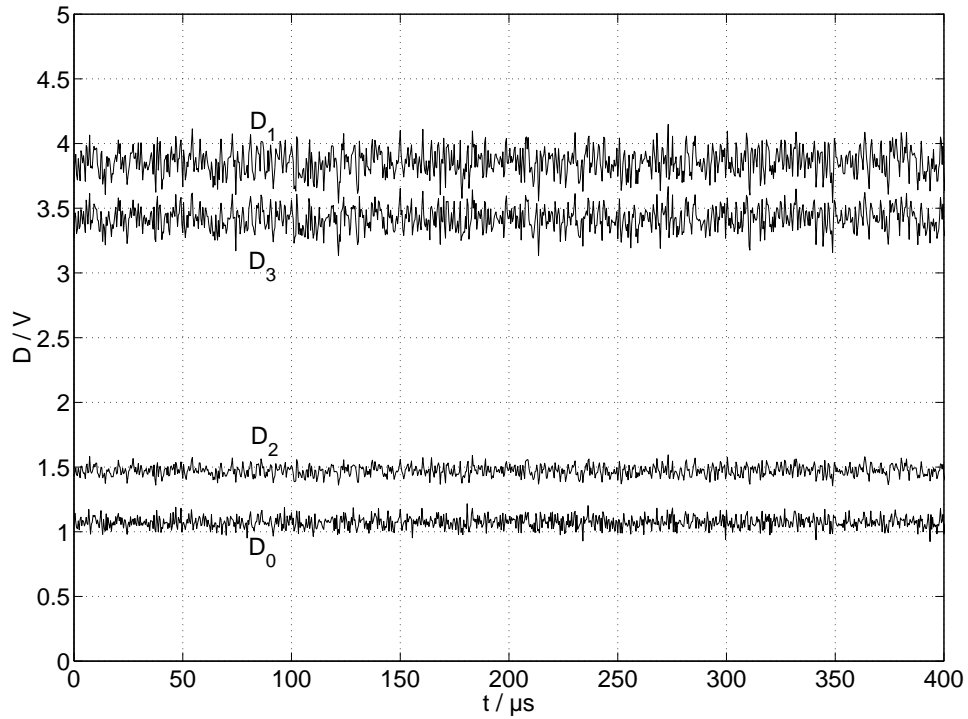


Figure 6.15: Detector signals for reflection on the BK7-glass prism during alignment to the measurement position
 t : time; D_0 , D_1 , D_2 , D_3 : detector signals.

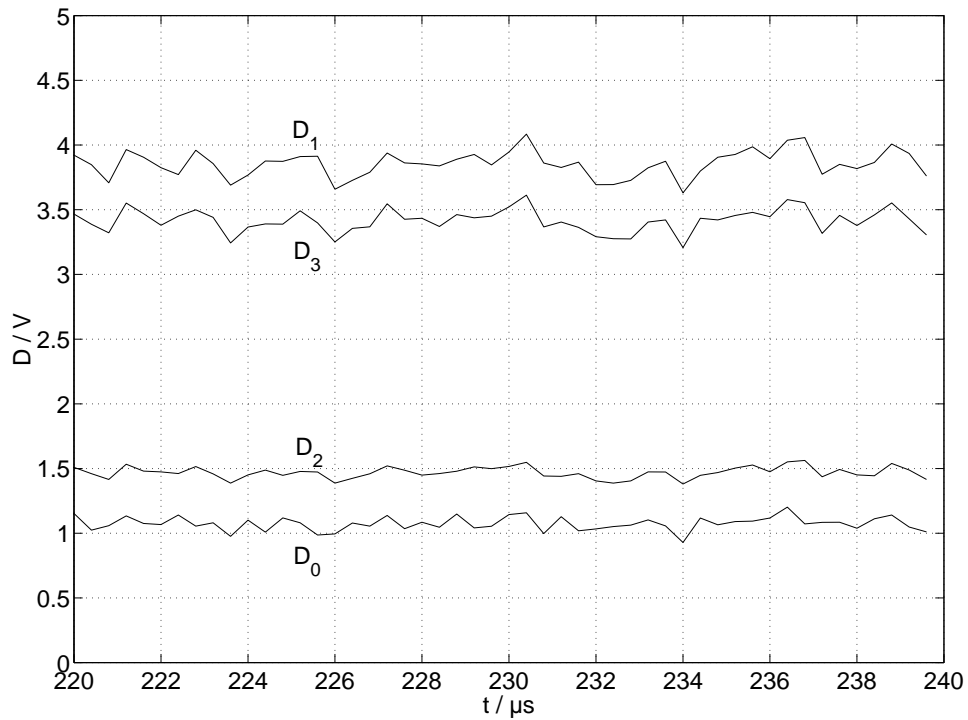


Figure 6.16: Zoom into the detector signals for reflection on the BK7-glass prism during alignment to the measurement position
 t : time; D_0 , D_1 , D_2 , D_3 : detector signals.

6.7 Measurement

During the pulse-heating experiment $+45^\circ$ -linear polarized light is applied to the wire sample. The PSD collects the reflected light at an angle of about 140° (see Fig. 6.1 b)), which corresponds to an incidence and/or reflectance angle of $\Theta = 70^\circ$. The Stokes vector \mathbf{S}^r of the reflected light is given by equation (6.2) and must be normalized with respect to S_0^r . Therefore we have

$$\mathbf{S}^i = \begin{pmatrix} 1 \\ S_1^r \\ S_2^r \\ S_3^r \end{pmatrix} \quad (6.55)$$

The ellipsometric parameters Δ and ψ are obtained from equations (5.54) and (5.55)

$$\Delta = \arctan\left(\frac{-S_3^r}{S_2^r}\right) \quad (6.56)$$

$$\psi = \frac{1}{2} \arctan\left(\frac{\sqrt{(S_2^r)^2 + (S_3^r)^2}}{-S_1^r}\right) \quad (6.57)$$

and the optical parameters n_2 and k_2 of the sample by the fundamental equation of ellipsometry (5.62)

$$n_2 - ik_2 = n_1 \tan \Theta \sqrt{1 - \frac{4\rho \sin^2 \Theta}{(1 + \rho)^2}} \quad (6.58)$$

where $\rho = \tan \psi e^{i\Delta}$ and n_1 is the refractive index of the ambient.

Finally the normal-spectral emissivity ϵ_λ at 684.4 nm of the sample material is given by equation (5.5)

$$\epsilon_\lambda(0) = \frac{4n_1 n_2}{(n_1 + n_2)^2 + k_2^2} \quad (6.59)$$

Geometrical considerations

The angle of reflection is not fixed at one value as assumed using equation (5.62), but it lies in a certain interval due to the acceptance angle of the PSD, determined by the opening of the iris diaphragm. Another problem is the accurate alignment of the angle of reflection. So this chapter is intended to give an estimation on the occurring errors.

The geometrical situation when reflecting light on a cylindrical shaped sample is shown in Fig. 6.17. The opening of the iris diaphragm can be set between $0 \dots 25 \text{ mm}$. Therefore the half acceptance angle Φ is obtained by

$$\Phi = \arctan \frac{d}{2l} = 0 \dots 5.3^\circ \quad (6.60)$$

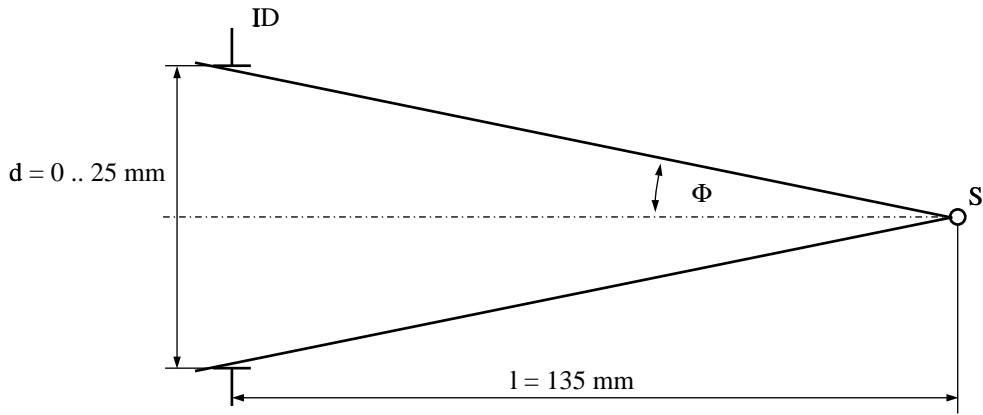


Figure 6.17: Geometrical considerations to the reflection of light on a cylindrical shaped sample \Rightarrow acceptance angle of the PSD

ID: iris diaphragm; *S*: sample; *d*: diameter of iris diaphragm; *l*: distance between sample and PSD; Φ : half acceptance angle of the PSD.

The acceptance angle Φ of the PSD corresponds to a certain interval of reflection angle Θ , which is derived in Fig. 6.18. From this we see

$$\Theta = \left[\Theta - \frac{\Phi}{2}, \Theta + \frac{\Phi}{2} \right] \quad (6.61)$$

The angular interval of reflection on the wire sample is also given by Φ (see Fig. 6.18), and subsequently we obtain for the arc length b within the reflection takes place

$$b = 2\pi r \frac{\Phi}{360^\circ} = 0 \dots 23 \mu\text{m} \quad (6.62)$$

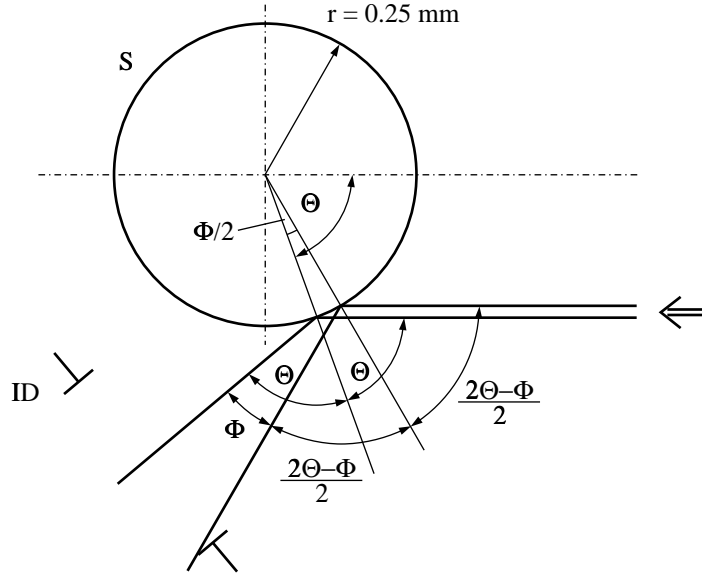


Figure 6.18: Geometrical considerations to the reflection of light on a cylindrical shaped sample \Rightarrow interval of reflection angle

ID: iris diaphragm; *S*: sample; *r*: radius of the sample;
 Θ : angle of reflection; Φ : half acceptance angle of the PSD.

The Stokes parameters of reflected light depend on the reflection angle Θ as can be seen from Fig. 5.12. To estimate the error due to the measured interval (6.61) instead of the nominal value of the reflection angle, we first simulate the Stokes parameters as a function of Θ using equation (5.53). The measured Stokes parameters are now given by the mean values

$$S_i = \frac{\int S_i(\Theta) dA}{\int dA} = \frac{\int_{\Theta - \frac{\Phi}{2}}^{\Theta + \frac{\Phi}{2}} S_i(\Theta) \cos \Theta d\Theta}{\int_{\Theta - \frac{\Phi}{2}}^{\Theta + \frac{\Phi}{2}} \cos \Theta d\Theta} \quad i = 0 \dots 3 \quad (6.63)$$

where the first integration is taken over the cross section of the incident beam. To come to the second equation we must consider the relation between an infinitesimal part of the cross sectional area dA and an infinitesimal change in reflection angle $d\Theta$. This is shown in Fig. 6.19. To do so, we also have to assume the following items

- The laser beam has a uniform beam profile in the region where the reflection takes place.
- The surface of the sample is ideally smooth and of ideal cylindrical shape.
- The detectors of the PSD receive the reflected intensities uniform within the acceptance angle.

Finally we compute the emissivity from Stokes parameters (6.63) using equations (6.55) to (6.59). The so obtained values are compared to the emissivity calculated with the nominal reflection angle of 70° . The result of the simulation is shown in Fig. 6.20, and we see that the error is smaller than 0.2% and therefore negligible.

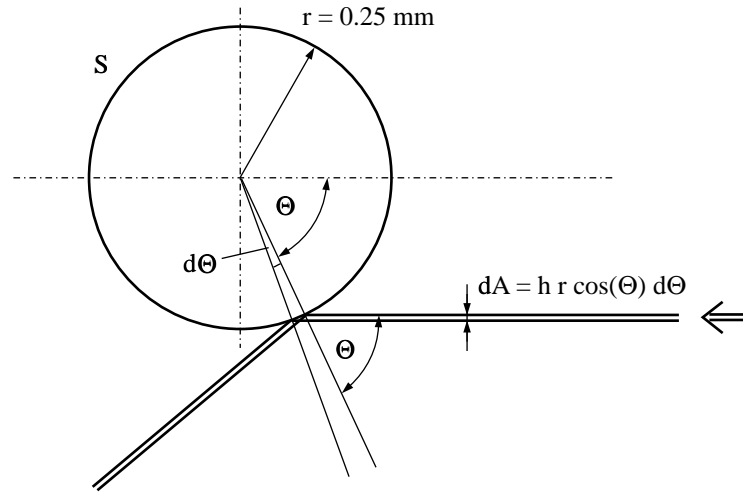


Figure 6.19: Geometrical considerations to the reflection of light on a cylindrical shaped sample \Rightarrow beam cross-sectional area
 S : sample; r : radius of the sample; Θ : angle of reflection;
 dA : infinitesimal beam cross-section corresponding to the infinitesimal reflection angle $d\Theta$; h : height of laser beam.

Actually there are changes in the Stokes parameters when opening the iris diaphragm. This effect is minimized when the PSD is well aligned. The remaining changes might come from the non-Gaussian laser profile as mentioned in chapter 6.3.

Another problem is the accurate alignment to the reflection angle $\Theta = 70^\circ$. Fig. 6.21 shows the error due to a misalignment of the PSD. This is calculated in the same way as the error due to the opening of the iris diaphragm, setting $d = 10 \text{ mm}$ and using in expression (6.63) the new integration interval

$$\Theta = \left[\Theta - \frac{\Phi}{2} - \Delta\Theta, \Theta + \frac{\Phi}{2} - \Delta\Theta \right] \quad (6.64)$$

The alignment of the PSD is done using the CCD-camera looking at the first field stop FS (see Fig. 6.2), where the reflected beam has to be centred at. A misalignment of $\Delta\Theta = 0.2^\circ$ corresponds to a shift of the beam at FS of about 1 mm and is additionally magnified by the CCD-camera. The field stop itself has an diameter of 1 mm , and therefore the alignment is always better than 0.5 mm . So the error due to misalignment is smaller than 0.5% in the computed emissivity.

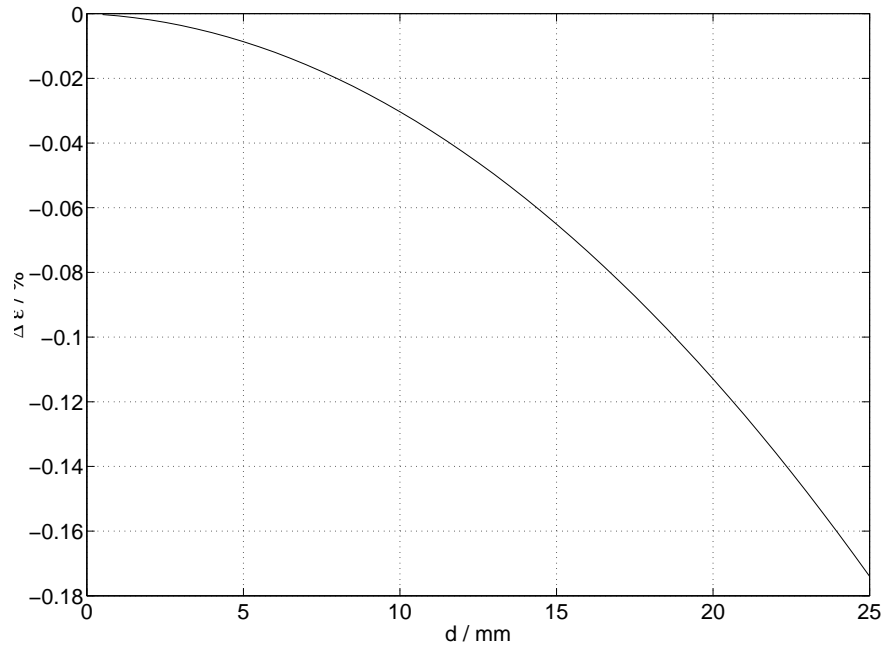


Figure 6.20: Error in emissivity dependent on the opening of the iris diaphragm (nominal reflection angle $\Theta = 70^\circ$, $n_2 = 2.5$, $k_2 = 2.5$)
 d : diameter iris diaphragm; $\Delta\epsilon$: relative error of emissivity.

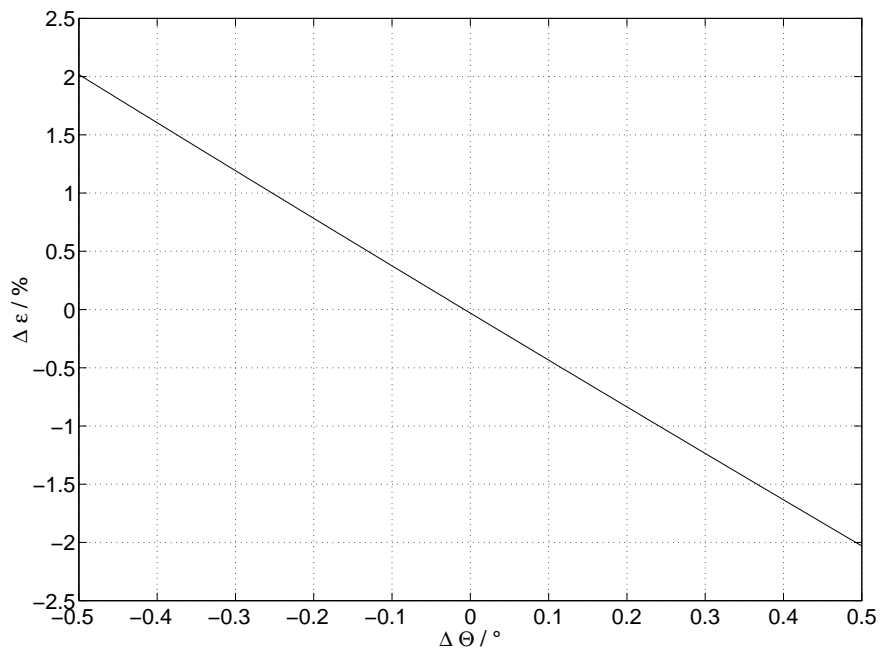


Figure 6.21: Error in emissivity depending on the misalignment of the PSD (nominal reflection angle $\Theta = 70^\circ$, opening of iris diaphragm $d = 10 \text{ mm}$, $n_2 = 2.5$, $k_2 = 2.5$)
 $\Delta\Theta$: deviation of reflection angle due to misalignment; $\Delta\epsilon$: relative error of emissivity.

Chapter 7

DOAP-mode of the HOTWIRE-program

7.1 DOAP-mode

The *DOAP*-mode is intended for evaluation of pulse heating data combined with emissivity measurement using a division-of-amplitude photopolarimeter. Temperature is calculated from radiance temperature and emissivity using equation (3.45).

Ellipsometry data acquisition is done by a special software package provided together with the DOAP system. Raw data are the four detector signals of the DOAP as well as current, voltage hot, voltage cold and intensity of radiation from the pulse heating experiment. The last four signals are either sampled with the DOAP system (every $0.4 \mu s$ with a sample depth of 1024 data points) or by the INSIGHT data acquisition as described in chapter 4.1. In the last case the pulse heating data must be reduced from the fast sample rate of $10 MHz$ to $2.5 MHz$ of the DOAP. This is the preferred method because it leads to smoothed input data. The further processing is the same as in *HOTWIRE*-mode, see chapter 4.1.

In principle all features of the *HOTWIRE*-mode are also available in *DOAP*-mode. So see chapter 4.1 for the evaluation of pulse heating data. One difference is the determination of temperature as described in chapter 7.2.

Additional to pulse heating data now there are also ellipsometric data, as listed in the following.

Raw data detector signals DOAP

Raw data versus time delivered by the acquisition software

- *Detector 1* ⇒ Fig. 7.1
- *Detector 2* ⇒ Fig. 7.2
- *Detector 3* ⇒ Fig. 7.3
- *Detector 4* ⇒ Fig. 7.4

Stokes parameters

Applying the calibration matrix to the detector signals the Stokes parameters are obtained using equation (6.2) and are normalized by (6.55). The ellipsometric parameters are calculated from (6.56).

- *Stokes parameter 1* \Rightarrow Fig. 7.5
- *Stokes parameter 2* \Rightarrow Fig. 7.6
- *Stokes parameter 3* \Rightarrow Fig. 7.7
- *Ellipsometric parameters* \Rightarrow Fig. 7.8

Ellipsometry

Refractive index and extinction coefficient are gained using the fundamental equation of ellipsometry (6.58). From those emissivity is computed using (6.59). The degree of polarization is given by (5.38).

- *Emissivity* \Rightarrow Fig. 7.9
- *Degree of polarization* \Rightarrow Fig. 7.10
- *Refractive index* \Rightarrow Fig. 7.11
- *Extinction coefficient* \Rightarrow Fig. 7.12

Ellipsometry additional

- *Emissivity versus radiance temperature* \Rightarrow Fig. 7.13
- *Emissivity versus temperature*
- *Emissivity versus spec. enthalpy* \Rightarrow Fig. 7.14
- *Emissivity versus time*

Data saved in *DOAP*-mode are:

- Time in μs
- Current in A
- Corrected voltage drop across wire in V
- Radiance temperature in K
- Temperature in K
- Temperature via melting plateau in K
- Spec. enthalpy in kJ/kg
- Spec. resistivity in $\mu\Omega m$
- Degree of polarization
- Emissivity

Similar as in *HOTWIRE*-mode a log-file is saved, which contains all the parameters used during data evaluation. The log-file is the same as printed in chapter 4.1. It only contains more data due to ellipsometry.

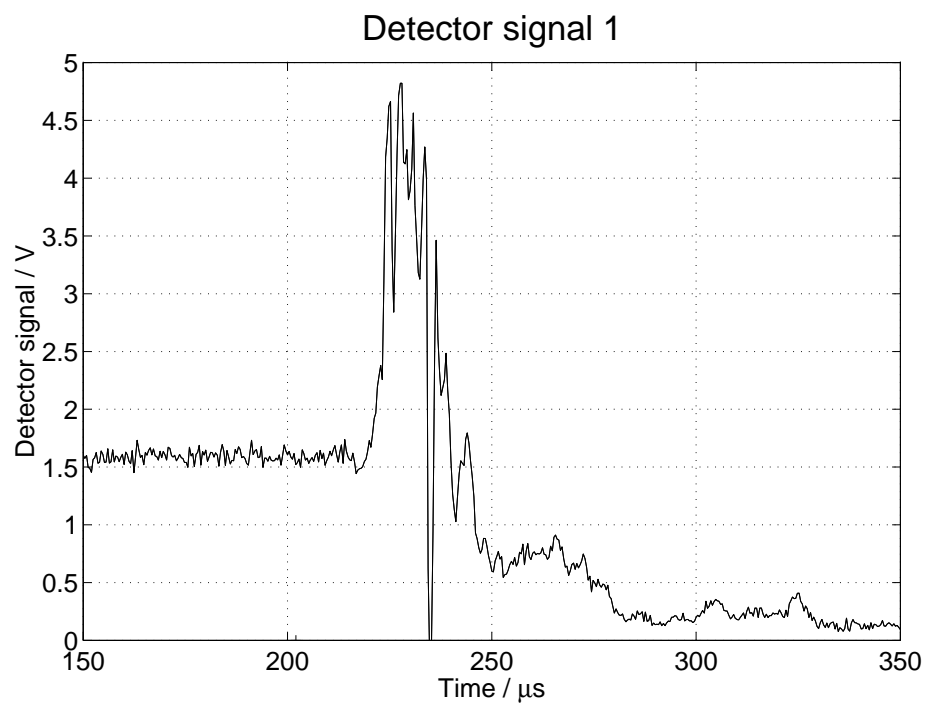


Figure 7.1: Raw data Niobium: signal of detector 1 versus time

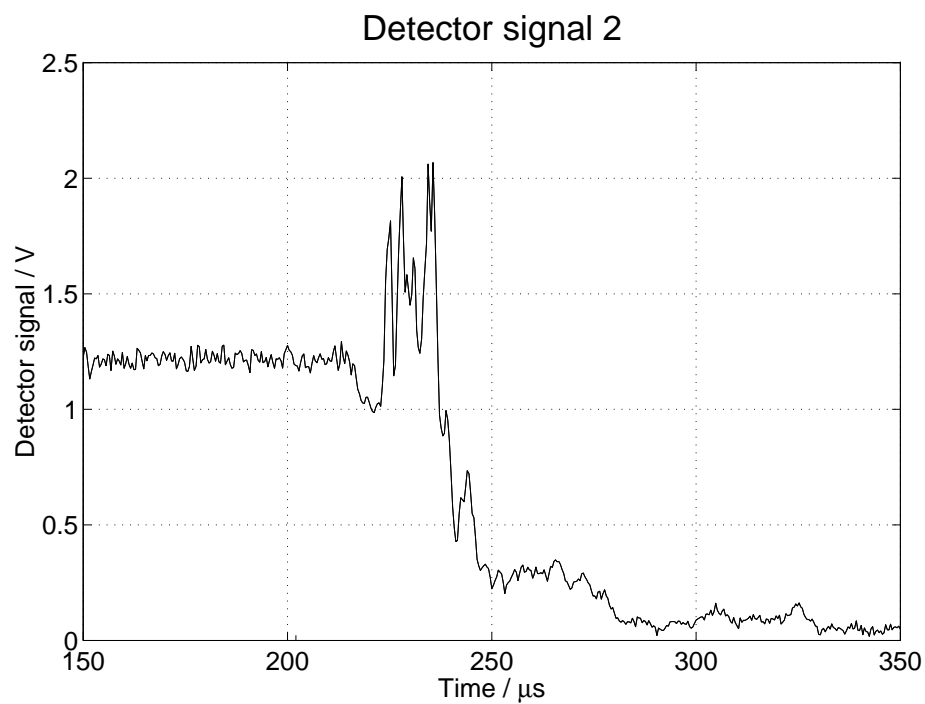


Figure 7.2: Raw data Niobium: signal of detector 2 versus time

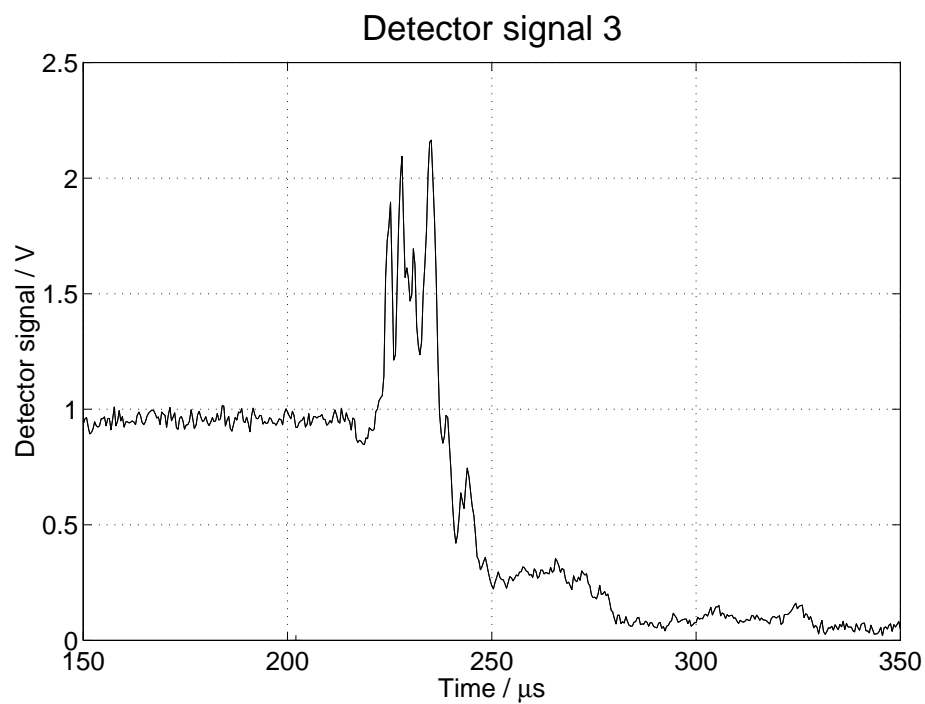


Figure 7.3: Raw data Niobium: signal of detector 3 versus time

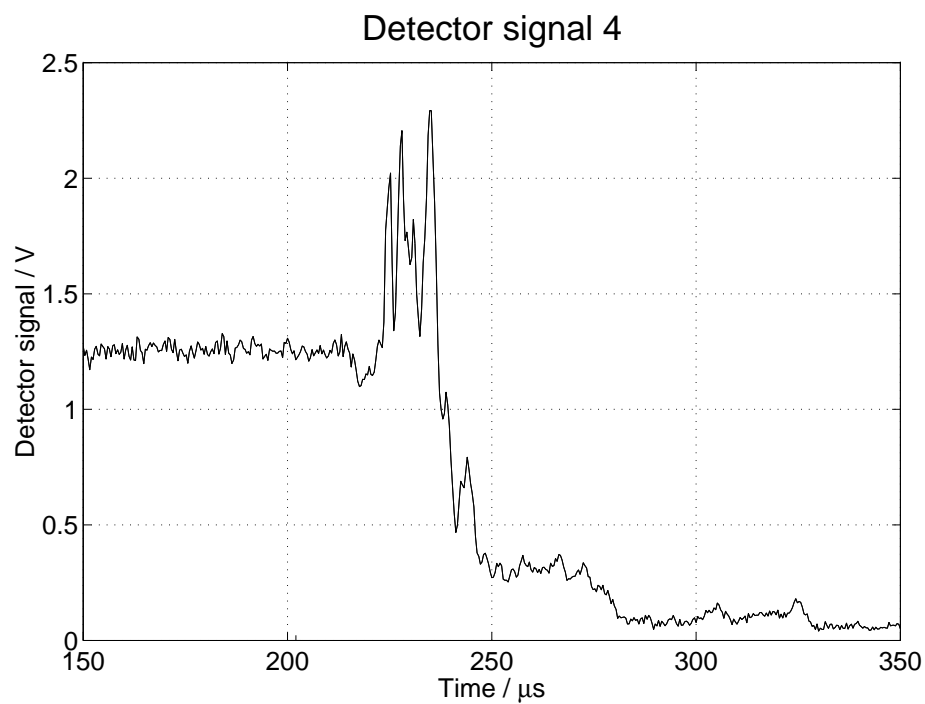


Figure 7.4: Raw data Niobium: signal of detector 4 versus time

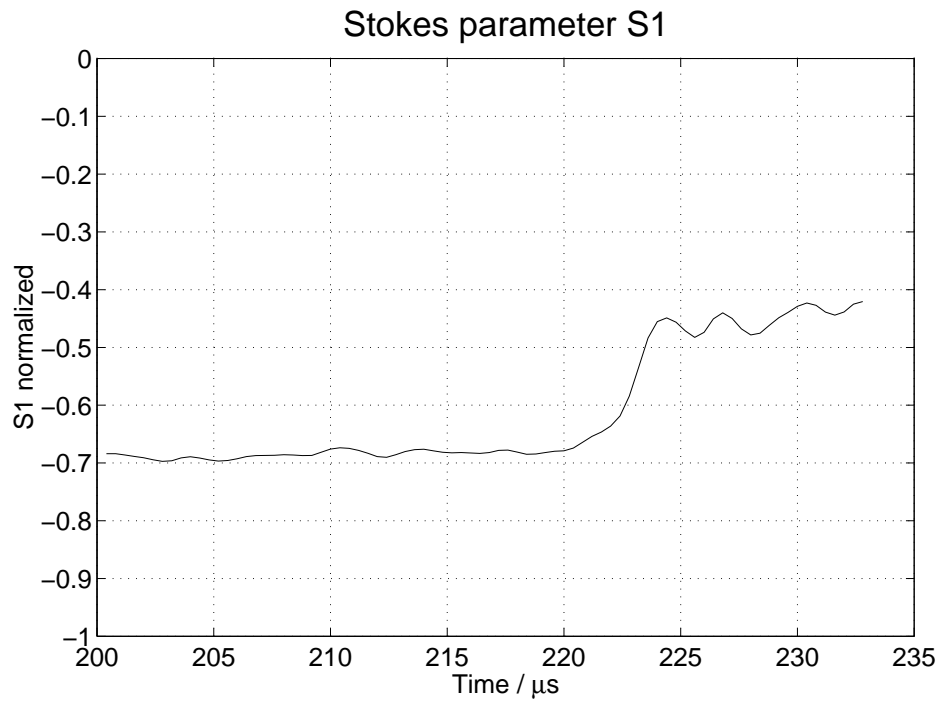


Figure 7.5: Ellipsometric data Niobium: normalized Stokes parameter 1 versus time

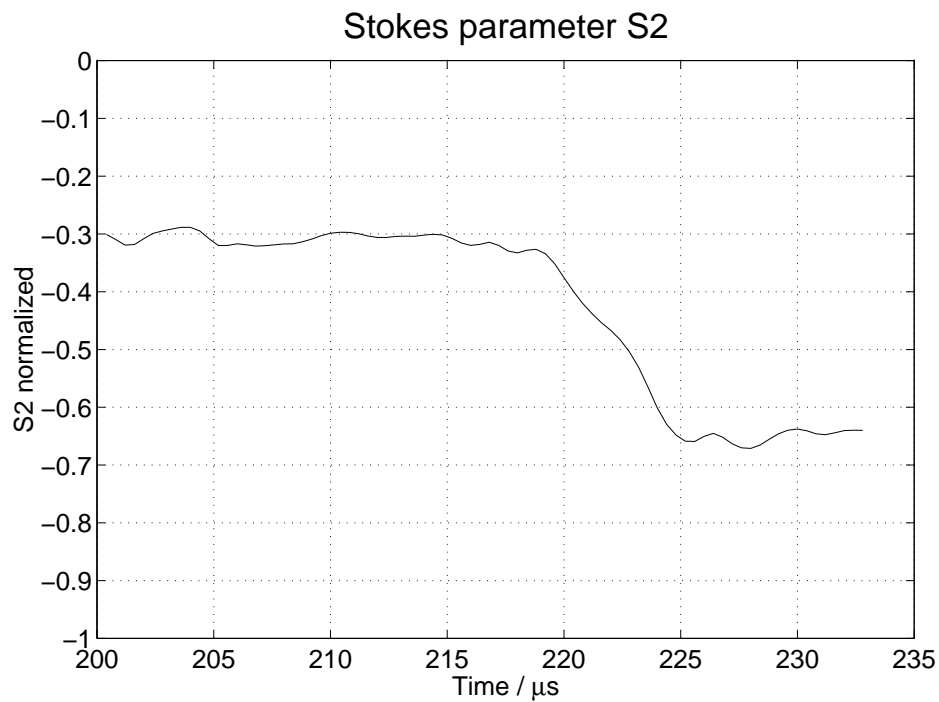


Figure 7.6: Ellipsometric data Niobium: normalized Stokes parameter 2 versus time

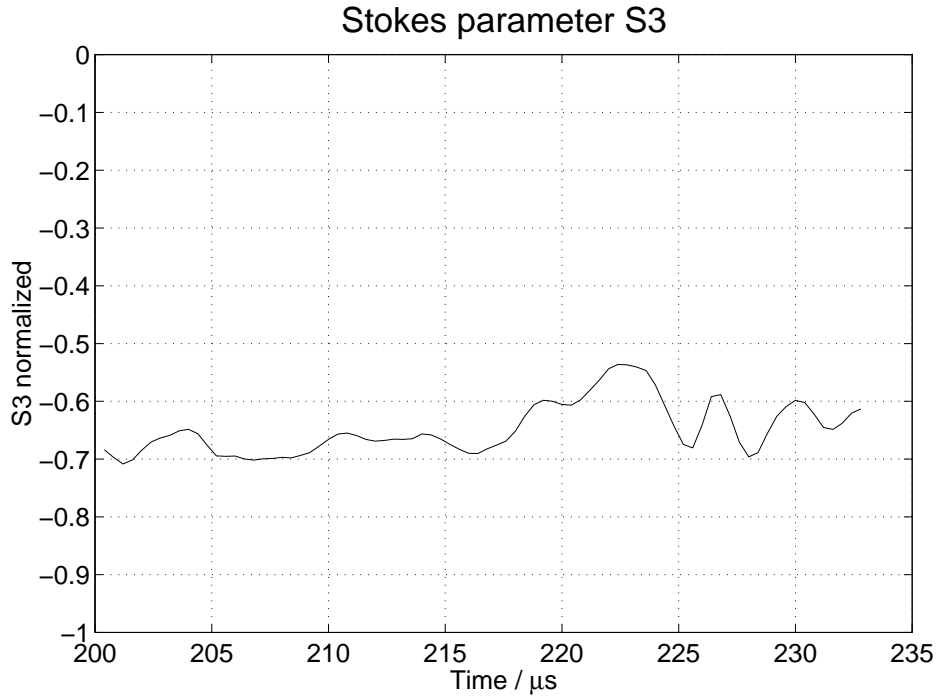


Figure 7.7: Ellipsometric data Niobium: normalized Stokes parameter 3 versus time

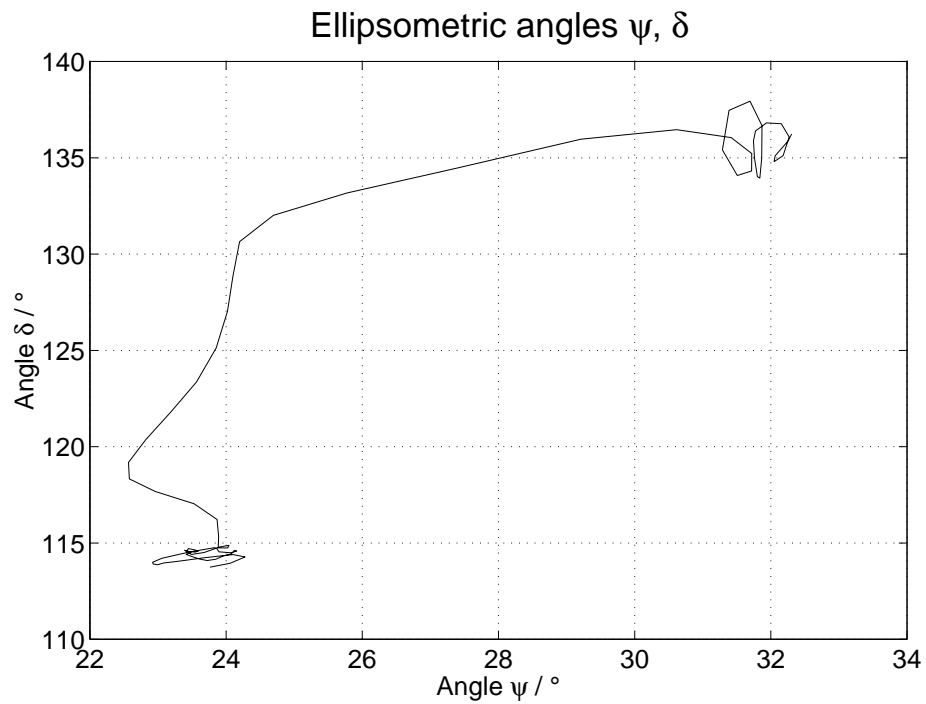


Figure 7.8: Ellipsometric data Niobium: ellipsometric parameters $\Rightarrow \delta$ versus ψ

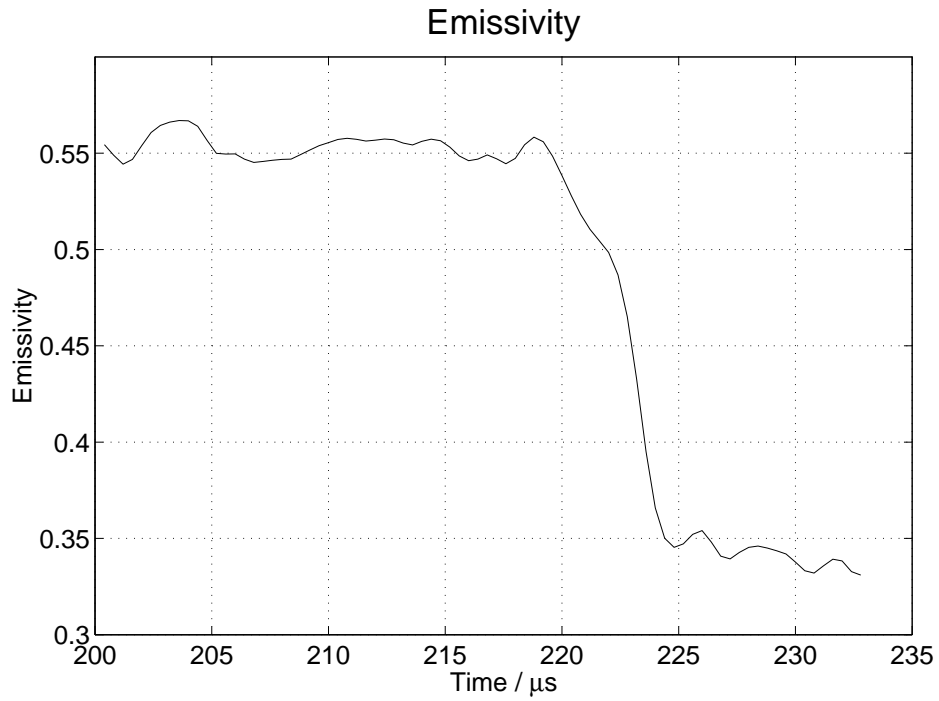


Figure 7.9: Result data Niobium: emissivity versus time

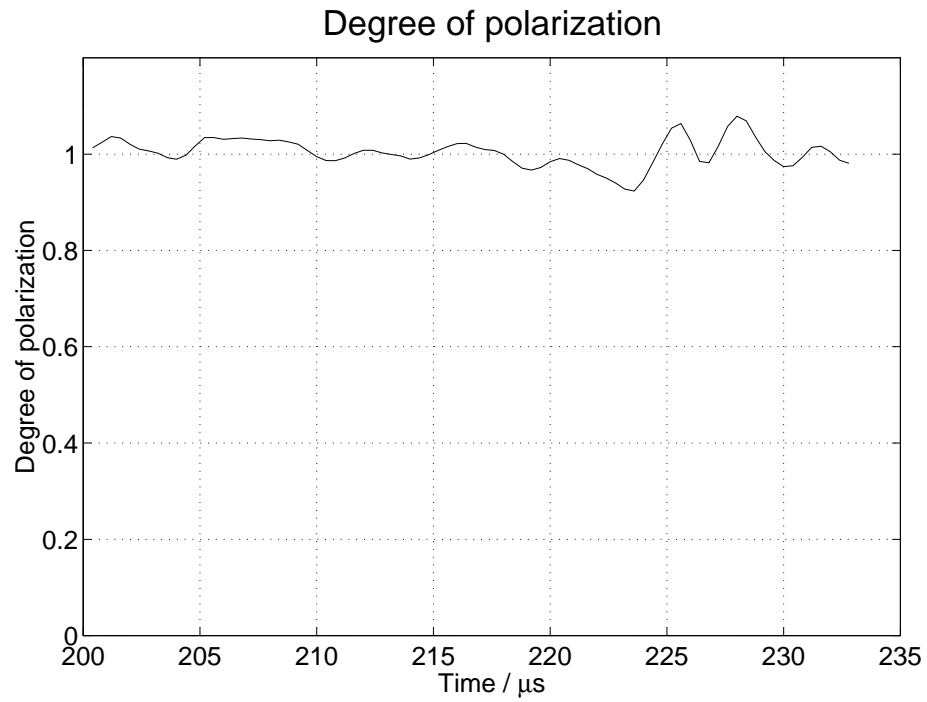


Figure 7.10: Ellipsometric data Niobium: degree of polarization versus time

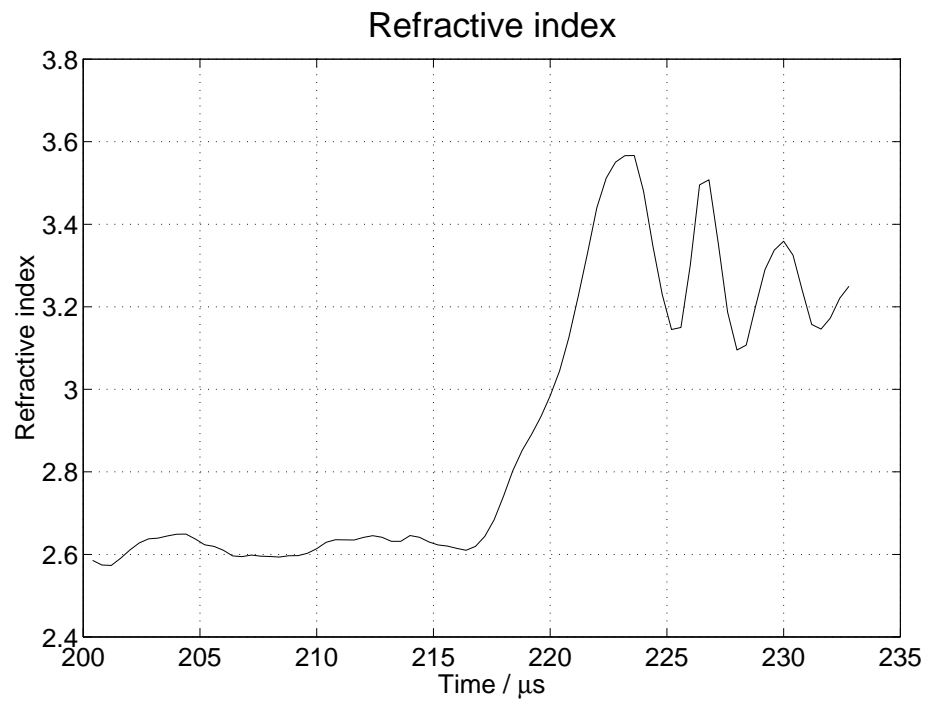


Figure 7.11: Optical constants Niobium: refractive index versus time

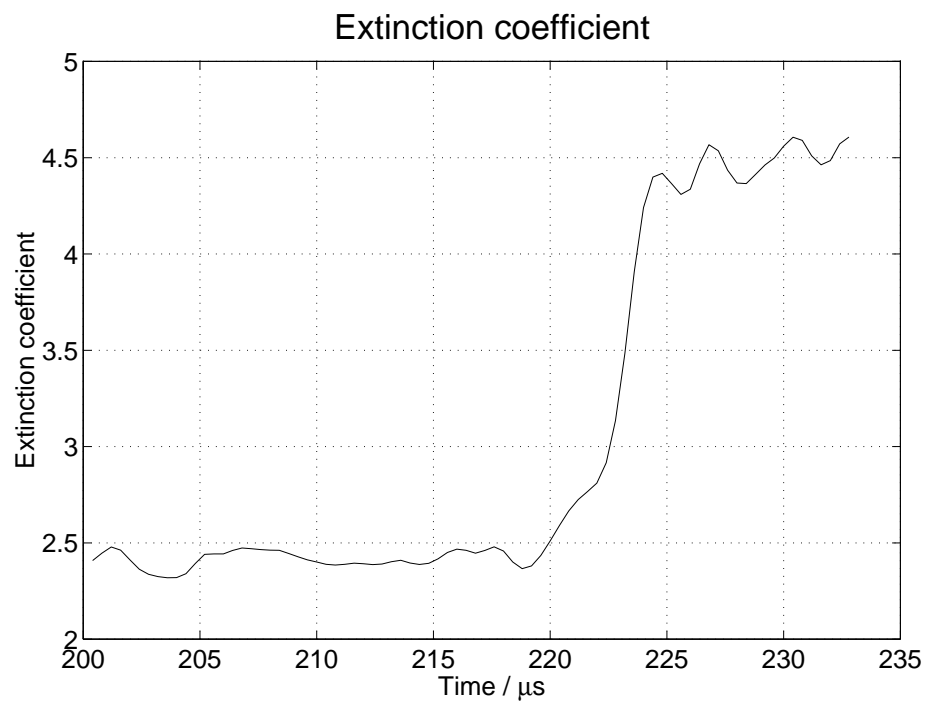


Figure 7.12: Optical constants Niobium: extinction coefficient versus time

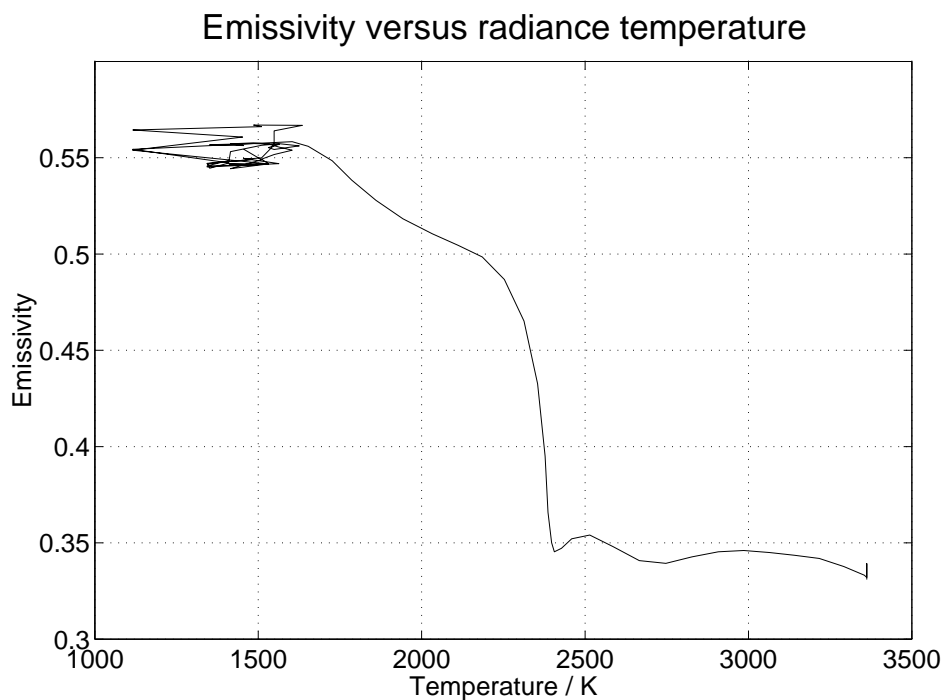


Figure 7.13: Result data Niobium: emissivity versus radiance temperature

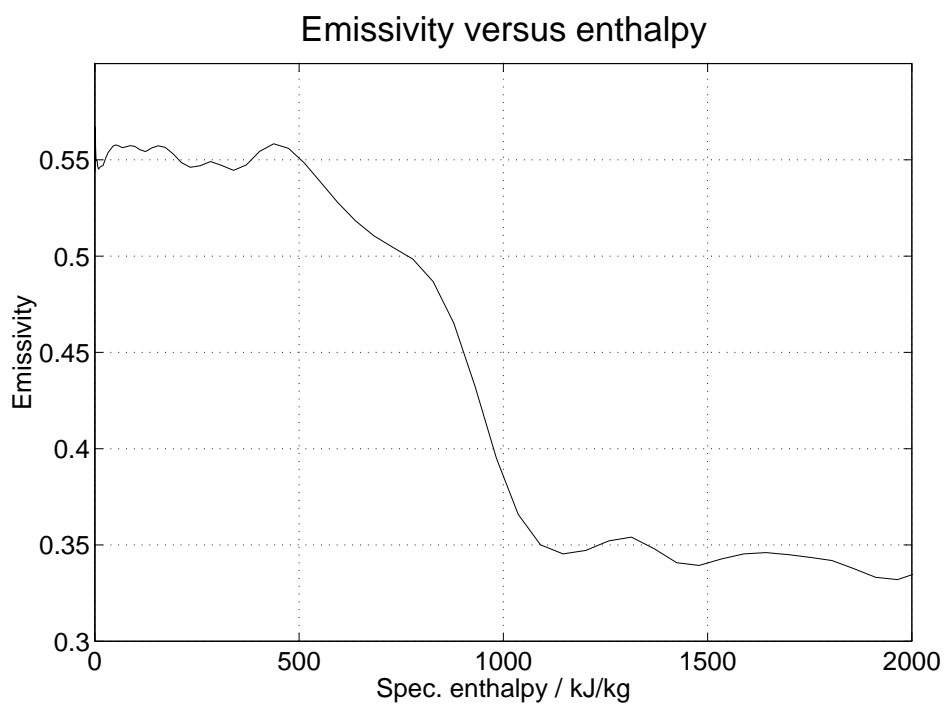


Figure 7.14: Result data Niobium: emissivity versus specific enthalpy

7.2 Temperature

As described in the theoretical part chapter 3.5 true temperature can be calculated by equation 3.45 from radiance temperature and emissivity. On the other hand it also possible to use the concept of the *HOTWIRE*-mode. In chapter 4.4 it is shown how to obtain true temperature via melting plateau as reference point. The same feature is available in *DOAP*-mode, where it is used to compare between the temperatures gained by the two different methods. The result for an experiment with Niobium is shown in Fig. 7.15.

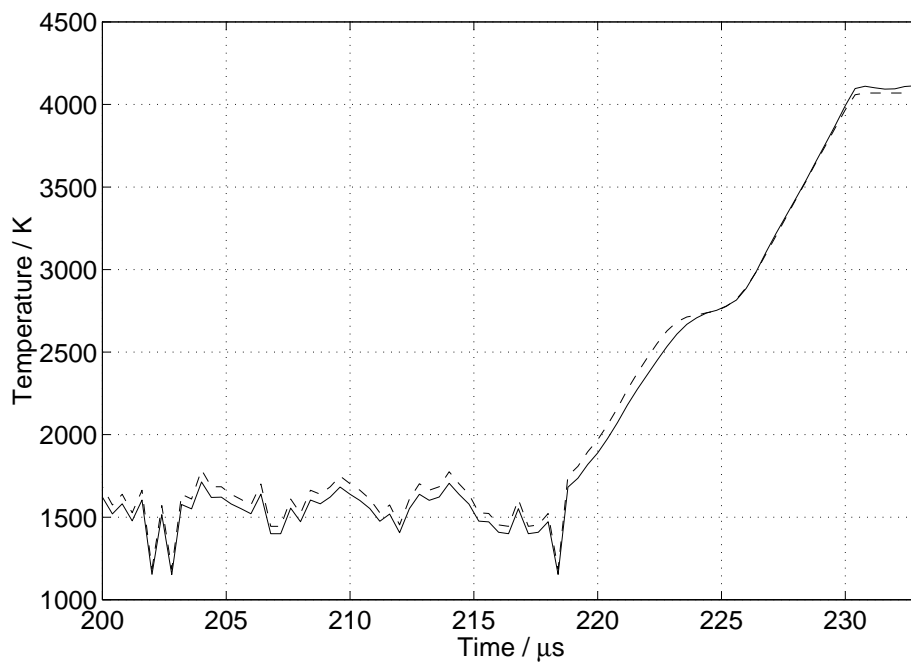


Figure 7.15: Comparison between true temperature calculated from radiance temperature and emissivity (solid curve) and temperature via melting plateau as reference point (dashed curve).

Chapter 8

Conclusion and future outlook

The *HOTWIRE*-program was first used by Cagran [19] for the evaluation of experiments on Copper. The results are in good agreement with other data published in literature.

A new aspect in the experiments is the emissivity measurement using the division-of-amplitude photopolarimeter. The calibration and its verification shows, that Stokes parameters can be achieved with a mean uncertainty of about ± 0.005 . Additionally, measurements on BK7-glass give the optical parameters n and k with a precision of three digits. But all these data are obtained by averaging over some thousand data points, and so the noise (see e.g. Fig. 6.14), originating mainly from the input amplifiers, cancels out. However, this is not the case during the actual pulse-heating experiment. The maximum sampling rate of the DOAP-system is 2.5 MHz due to limits in the electronics (linearity of the band-pass filters of the lock-in detection). So there are only about 10 data points during the phase transition from solid to liquid in a typical experiment. Of course, this is the most interesting interval, because emissivity changes very rapidly, as one sees comparing figures 4.6 and 7.9. Subsequently, in future projects the sampling rate as well as the bandwidth of the lock-in detection should be increased, e.g. using a digital lock-in technique, as proposed by Krishnan [20].

As shown in chapter 6.7, small variations in the alignment or the opening of the iris diaphragm should not influence the Stokes parameters very much from the theoretical point of view. Actually, the PSD is very sensitive to these actions, and so there are two considerations

- The optics of the PSD is very complex and small deviations from the ideal alignment lead to a different distribution of the intensities onto the individual detectors.
- The non-Gaussian beam profile has some intensity hot spots, which also can cause the sensitivity of the PSD to alignment.

Next time it is planned to install the laser outside the shielded room to avoid the optical fiber for coupling, and therefore to obtain a Gaussian beam profile. The difficulties are to maintain the electromagnetic shielding. Results will be given by Seifert [4].

The plan for the future is on one hand a systematic investigation on emissivity of different metals and alloys, such as e.g. Niobium, Tungsten, Copper, Molybdenum, Iron, Nickel and Invar. On the other hand, it should be proofed, if the DOAP can be used in combination with the high pressure vessel, which is described by Pottlacher [21]. Results will also be given by Seifert [4].

Appendix A

Data of selected metals

Table A.1: Density δ_{20} at $20^\circ C$ and melting temperature T_M of selected metals
Data taken from [23]

Chemical Symbol	Name	Atomic number	δ_{20} in kgm^{-3}	T_M in K
Ag	Silver	47	10500	1235
Al	Aluminium	13	2700	934
Au	Gold	79	19300	1338
Ba	Barium	56	3500	998
Be	Beryllium	4	1848	1551
Bi	Bismuth	83	9800	544
Ca	Calcium	20	1550	1112
Cd	Cadmium	48	8640	594
Co	Cobalt	27	8900	1768
Cr	Chromium	24	7100	2130
Cu	Copper	29	8960	1356
Fe	Iron	26	7870	1808
Ge	Germanium	32	5320	1210
Hf	Hafnium	72	13100	2500
In	Indium	49	7300	429
Ir	Iridium	77	22400	2683
La	Lanthanum	57	6174	1194
Li	Lithium	3	534	454
Mg	Magnesium	12	1740	922
Mn	Manganese	25	7400	1517
Mo	Molybdenum	42	10220	2890
Nb	Niobium	41	8570	2741
Ni	Nickel	28	8900	1726
Os	Osmium	76	22500	3318
Pb	Lead	82	11350	601
Pd	Palladium	46	12000	1827
Pt	Platinum	78	21450	2045
Re	Rhenium	75	21000	3453
Rh	Rhodium	45	12400	2238
Ru	Ruthenium	44	12200	2583
Sb	Antimony	51	6680	904
Sc	Scandium	21	2990	1814
Sn	Tin	50	7280	505
Sr	Strontium	38	2600	1043
Ta	Tantalum	73	16600	3269
Te	Tellurium	52	6250	723
Ti	Titanium	22	4500	1933
Tl	Thallium	81	11850	577
V	Vanadium	23	6100	2163
W	Tungsten	74	19300	3683
Y	Yttrium	39	4478	1795
Zn	Zinc	30	7140	693
Zr	Zirconium	40	6490	2125

Table A.2: Refractive index n , extinction coefficient k , pseudo-Brewster angle Θ_B and spectral-normal emissivity ϵ_λ at wavelength λ for selected metals at room temperature (20°C)
Data taken from [24]

Chemical Symbol	Name	n	k	Θ_B in $^\circ$	ϵ_λ	λ in nm
Ag	Silver	0.140	4.44	76.7	0.03	688.8
Au	Gold	0.160	3.80	74.4	0.04	688.8
Cr	Chromium	3.84	4.37	80.1	0.36	700.5
Cu	Copper	0.213	4.05	75.4	0.05	688.0
Ir	Iridium	2.64	4.81	79.4	0.29	688.8
Mo	Molybdenum	3.81	3.58	79.0	0.42	688.8
Nb	Niobium	2.69	2.89	75.3	0.49	670.2
Ni	Nickel	2.14	4.00	77.1	0.33	688.8
Os	Osmium	3.78	1.83	76.5	0.58	688.8
Pd	Palladium	1.80	4.42	78.4	0.26	704.5
Pt	Platinum	2.51	4.43	78.6	0.31	688.8
Rh	Rhodium	2.30	6.02	81.0	0.20	688.8
Ta	Tantalum	1.35	2.60	69.8	0.44	688.8
V	Vanadium	3.43	3.05	77.5	0.47	688.8
W	Tungsten	3.82	2.91	78.1	0.48	688.8

Bibliography

- [1] Pottlacher G., 1998: *"Beiträge zur experimentellen Untersuchung thermophysikalischer Daten flüssiger Metalle und Legierungen"*, Habilitationsschrift, TU-Graz
- [2] Azzam R. M. A., 1982: "Division-of-amplitude photopolarimeter (DOAP) for the simultaneous measurement of all four Stokes parameters of light", *Opt. Acta* **29**, 685-689
- [3] Krishnan S., Nordine P. C., 1996: "Fast ellipsometry and Mueller-matrix ellipsometry using the division-of-amplitude photopolarimeter", *SPIE Vol.* 2873
- [4] Seifter A., 2001: Dissertation, TU-Graz
- [5] Kaschnitz E., 1992: *"Bestimmung thermophysikalischer Daten verschiedener Metalle bei ohmscher Pulsaufheizung im Mikrosekundenbereich"*, Dissertation, TU-Graz
- [6] Seydel U., Fücke W., Wadle H., 1980: *"Die Bestimmung thermophysikalischer Daten flüssiger hochschmelzender Metalle mit schnellen Pulsaufheizexperimenten"*, Verlag Dr. Peter Mannhold, Düsseldorf
- [7] Küpfmüller K., 1990: *"Einführung in die theoretische Elektrotechnik"*, Springer-Verlag
- [8] Weißmantel Ch., Hamann C., 1980: *"Grundlagen der Festkörperphysik"*, Springer-Verlag
- [9] Seifter A., 1996: *"Bestimmung thermophysikalischer Daten von Eisen - Nickel - Legierungen im flüssigen Zustand mittels ohmscher Pulsaufheizung"*, Diplomarbeit, TU-Graz
- [10] DeWitt P. P., Nutter G. D., 1988: *"Theory and Practice of Radiation Thermometry"*, A Wiley-Interscience Publication, JOHN WILEY & SONS, Inc.
- [11] Papoušek W., 1998: *"Elektrodynamik"*, Skriptum zur Lehrveranstaltung 515.524, Semester Technische Physik, ©Hochschülerschaft an der TU-Graz GmbH
- [12] Azzam R. M. A., Bashara N. M., 1992: *"Ellipsometry and polarized light"*, North-Holland, Amsterdam
- [13] Collett E., 1993: *"Polarized light"*, Marcel Dekker, Inc.
- [14] Azzam R. M. A., Masetti E., Elminyawi M., El-Saba A. M., 1988: "Construction, calibration, and testing for a four-detector photopolarimeter", *Rev. Sci.Instrum.* **59**, 84-88

- [15] Azzam R. M. A., Lopez A. G., 1989: "Accurate calibration of the four-detector photopolarimeter with imperfect polarizing elements", J. Opt. Soc. Am. **A6**, 1513-1521
- [16] Krishnan S., 1992: "Calibration, properties, and application of the division-of-amplitude photopolarimeter at 632.8 and 1523 nm", J. Opt. Soc. Am. **A9**, 1615-1622
- [17] Azzam R. M. A., 1989: "Instrument matrix of the four-detector photopolarimeter: physical meaning of its rows and columns and constraints on its elements", J. Opt. Soc. Am. **A7**, 87-91
- [18] Brudzewski K., 1991: "Static Stokes ellipsometer: general analysis and optimization", J. Mod. Opt. **38**, 889-896
- [19] Cagran C., 2000: "*Thermal conductivity and thermal diffusivity of liquid copper*", Diploma thesis, TU-Graz
- [20] Krishnan S., 2000, private communication
- [21] Pottlacher G., Jäger H., 1990: "Measurement of thermophysical properties of Lead by a submicrosecond pulse heating method (2000 to 5000 K)", International Journal of Thermophysics, Vol. 11.4, p. 719 - 729
- [22] *Melles Griot catalogue*, 2000,
- [23] *Goodfellow catalogue*, 1999
- [24] Palik E. D., 1990: "*Handbook of Optical Constants of Solids*", Academic Press, Inc.